

# Impact of choices for center-of-mass correction energy on the surface energy of Skyrme energy density functionals

Philippe Da Costa <sup>1</sup>, Karim Bennaceur <sup>1</sup>, Jacques Meyer <sup>1</sup>, Wouter Ryssens <sup>2</sup>, and Michael Bender <sup>1</sup>

<sup>1</sup>*Université Claude Bernard Lyon 1, CNRS/IN2P3, IP2I,*

*UMR 5822, rue E. Fermi, F-69622 Villeurbanne Cedex, France*

<sup>2</sup>*Institut d'Astronomie et d'Astrophysique, Université Libre de Bruxelles,*  
*Campus de la Plaine CP 226, 1050 Brussels, Belgium*

(Dated: 21 March 2023)

**Background:** In the framework of nuclear energy density functional (EDF) methods, many nuclear phenomena can be related to the deformation of intrinsic states. Their accurate modeling relies on the correct description of the change of nuclear binding energy with deformation. The two most important contributions to the deformation energy have their origin in shell effects and the surface energy coefficient of nuclear matter.

**Purpose:** It has been pointed out before that the choices made for the center-of-mass (c.m.) correction energy and the effective mass during the parameter adjustment influence the deformation properties of nuclear EDFs. We study the impact of these two properties by means of a set of purpose-built parametrizations of the standard Skyrme EDF at next-to-leading (NLO) order in gradients.

**Methods:** In a first step, we build nine series of parametrizations with a systematically varied surface-energy coefficient  $a_{\text{surf}}$  for three frequently-used options for the c.m. correction (none, one-body term only, full one-body and two-body contributions) combined with three values for the isoscalar effective mass  $m_0^*/m$  (0.7, 0.8, 0.85) and analyse how well each of these parametrizations can be adjusted to the properties of spherical nuclei and infinite nuclear matter. In a second step, we performed additional fits without the constraint on surface energy, adding one “best-fit” parametrization to each of the nine series. We then benchmark these parametrizations to the deformation properties of heavy nuclei by means of three-dimensional Hartree-Fock-Bogoliubov calculations that allow for non-axial and/or non-reflection symmetric configurations.

**Results:** We perform a detailed correlation analysis between surface and volume properties of nuclear matter using the nine series of parametrizations. The best fits out of each series are then benchmarked on the fission barriers of  $^{240}\text{Pu}$  and  $^{180}\text{Hg}$ , as well as on the properties of deformed states at normal and superdeformation for actinides and nuclei in the neutron-deficient Hg region.

**Conclusions:** The main conclusions are as follows: (i) Each combination of choices for c.m. correction and  $m_0^*/m$  leads to a significantly different optimal value of  $a_{\text{surf}}$ , reason being that the effective interaction has to absorb the contribution of the c.m. correction to the total binding energy. (ii) Many properties of symmetric and asymmetric infinite nuclear matter of Skyrme NLO EDFs are strongly correlated to the value of  $a_{\text{surf}}$ . (iii) Omitting the c.m. correction results in values of  $a_{\text{surf}}$  that are systematically too small. On the other hand, including the one-body term but neglecting the computationally expensive two-body term means  $a_{\text{surf}}$  will be too large. Both choices result in unrealistic predictions for fission barriers and superdeformed states of heavy nuclei. Only by incorporating the complete c.m. correction does one obtain quite realistic surface properties from an adjustment protocol that only constrains properties of infinite nuclear matter and spherical nuclei. (iv) Lowering  $a_{\text{surf}}$  increases the susceptibility of finite nuclei to take an exotic shape.

## I. INTRODUCTION

The self-consistent mean-field approach and its extensions, such as the Random Phase Approximation (RPA) and the Generator Coordinate Method (GCM), allow for the systematic study of properties and phenomena for all systems throughout the chart of nuclei [1, 2]. Using a universal energy density functional (EDF) to model the effective in-medium nucleon-nucleon interaction, these techniques give access to numerous observables concerning ground and excited states of nuclei, such as binding energies, deformations, isomeric states, rotational bands, as well as the large-amplitude collective motion of nuclear systems. Furthermore, symmetry-broken mean-field configurations allow for a natural interpretation of experimental data in terms of the shape of the nucleus in its intrinsic frame.

With the arrival of a wealth of new data on many

different aspects of the fission process [3, 4] and major advances in its microscopic modeling [5, 6], there is a renewed interest in constructing parametrizations of the nuclear EDFs that are predictive for physics at large deformation [7].

Indeed, not all parametrizations of the nuclear EDF, most of which are mainly adjusted to properties of nuclear matter and finite spherical nuclei, describe well the available information on nuclear states at large deformation [8] or fission barriers [9]. There are in fact just very few parametrizations of the nuclear EDF that are widely-used for nuclear fission studies, among which the Skyrme parametrization SkM\* [10] and the Gogny interaction D1S [11] are arguably the most prominent. Both were in fact constructed by the readjustment of an earlier parametrization that was unable to reproduce even the gross trends of fission barriers.

It is well established that a correct description of shape

isomeric states and fission barriers of heavy nuclei is strongly correlated with the value of the surface energy coefficient  $a_{\text{surf}}$  [9, 10, 12, 13] and, to a lesser degree, also with the surface symmetry energy coefficient  $a_{\text{ssym}}$  [8] of semi-infinite nuclear matter. There is, however, not a one-to-one correspondence as the actual minima and maxima of the deformation energy landscape of finite nuclei are generated by shell effects. Still, the values of  $a_{\text{surf}}$  and  $a_{\text{ssym}}$  can be indirectly used to inform parameter fits about deformation energies [9–11].

The binding energy of finite nuclei is, of course, also strongly correlated with  $a_{\text{surf}}$ . In a liquid-drop picture of a nucleus with  $A$  nucleons, the surface energy is the only contribution to the binding energy that scales as  $A^{2/3}$ . Nuclear masses therefore strongly constrain  $a_{\text{surf}}$  even when considering spherical nuclei only.

It has also been pointed out that the choices made to approximately correct for spurious center-of-mass (c.m.) motion during the parameter adjustment have an impact on the resulting surface properties [14]. The motivation for such correction is that the localized  $A$ -body states used in the mean-field modeling of static finite nuclei are not eigenstates of the many-body momentum operator  $\hat{\mathbf{P}} = \sum_i \hat{\mathbf{p}}_i$  with eigenvalue zero, but rather are superpositions of eigenstates of  $\hat{\mathbf{P}}$  that only yield an average value of  $\langle \hat{\mathbf{P}} \rangle = 0$ . The resulting spurious excitation energy can be approximately eliminated by subtracting the average value of the kinetic energy of the nucleus in its c.m. frame, which is the expectation value of the operator [14–17]<sup>1</sup>

$$\frac{1}{2Am} \hat{\mathbf{P}}^2 = \sum_i \frac{\hat{\mathbf{p}}_i^2}{2Am} + \sum_{i < j} \frac{\hat{\mathbf{p}}_i \cdot \hat{\mathbf{p}}_j}{Am}, \quad (1)$$

where the sums run over occupied single-particle states. The first term on the r.h.s. is a one-body operator that yields  $1/A$  times the free kinetic energy. The second term, however, is a two-body operator that leads to a non-local contribution to the total energy.

The numerical implementation of the two-body term is comparatively cumbersome, and, at least in the context of the otherwise local Skyrme EDF, its calculation is quite costly in terms of CPU time. For this reason, the two-body term has been omitted for the vast majority of parametrizations of Skyrme-type EDFs adjusted so far, including well-known examples such as SkM\* [10], SLy5s1 [9], SLy4 and SLy5 [17].

Some parametrizations that aim at describing nuclear fusion or fission dynamics were adjusted without any c.m. correction at all, examples being SLy4d [18] and UNEDF2 [19]. The motivation for the latter practice is that,

because of the  $1/A$  factor, the c.m. correction cannot be consistently defined for processes where two nuclei fuse or one nucleus splits apart without introducing further corrections for other types of spurious motion [20, 21].

Among the Skyrme parametrizations that were adjusted including the full c.m. correction (1) are the SkI $x$  and SV- $x$  parametrizations of Refs. [22, 23], SLy6 and SLy7 from Ref. [17], and those of the large-scale mass fits from Refs. [24–29]. The full c.m. correction is also considered for most of the parametrizations of the Gogny force such as D1S [11].

Disregarding for the moment parametrizations that were explicitly adjusted to nuclear properties at large deformation, and parametrizations that were adjusted with a specific emphasis on other observables than nuclear ground-state data, there is a correlation between the scheme for c.m. correction and the performance for fission barrier heights. This observation becomes particularly obvious for parameter sets constructed within the same protocol, but with different choices for the c.m. correction [14]. Parametrizations that are adjusted with the full c.m. correction give systematically smaller fission barriers than parametrizations that keep only the one-body part, but are otherwise adjusted within the same fit protocol. This finding is not related to the deformation dependence of the c.m. correction itself, which in general is quite small [14]. Instead, the interaction part of the EDF has to absorb the absent contributions from Eq. (1) to the total binding energy. There are indications that considering or not the c.m. correction as such might cause a similar problem: as pointed out in Ref. [9], the SLy4d parametrization [18] that was adjusted with the same protocol as SLy4 and SLy6 but without any c.m. correction at all, gives significantly smaller fission barriers than SLy6.

Among these three families of Skyrme parametrizations, those adjusted with the full c.m. correction perform systematically better for fission barriers. This does not, however, mean that *only* these perform well. Indeed, the long-standing reference parametrization for fission studies, SkM\* [10], belongs to the family of parametrizations that only consider the one-body c.m. correction. Similarly, the UNEDF1 [12] and UNEDF2 [19] parametrizations that have been used in recent fission studies were adjusted without any c.m. correction. What these exceptions have in common is that in one way or the other they were explicitly adjusted to some characteristics of fission barriers: SkM\* via readjusting some parameters of the earlier SkM parametrization [30] such that  $a_{\text{surf}}$  reproduces a semi-classical estimate for the fission barrier of  $^{240}\text{Pu}$  [10], whereas the fit protocol of UNEDF1 [12] and UNEDF2 [19] considers excitation energies of some fission isomers. The adjustment of the D1S parametrization of the Gogny force [11], which employs the full c.m. correction, was also informed by fission barrier heights. Other examples of such parametrizations are those of the SLy5sX series that employ only the one-body contribution to the c.m. correction and which were constructed

<sup>1</sup> This expression assumes that one is in the c.m. frame of the nuclear system, i.e. that  $\langle \hat{\mathbf{P}} \rangle = 0$ . If this is not the case, then the c.m. correction energy is proportional to the dispersion of  $\hat{\mathbf{P}}$ , i.e.  $\frac{1}{2Am} (\langle \hat{\mathbf{P}}^2 \rangle - \langle \hat{\mathbf{P}} \rangle^2)$ , instead.

with a systematically varying constraint on  $a_{\text{surf}}$  with the aim of finding the one that performs best for fission barriers [9]. That the deformation energy of parameter sets adjusted with the full c.m. correction is automatically more realistic can serve as the starting point for their fine-tuning to fission barriers. The very recent mass fits BSkG2 [28, 29] and BSkG3 [31] use the full c.m. correction and achieve a mean deviation of less than 500 keV on the primary and secondary barriers of 45 actinide nuclei, including odd and odd-odd ones, through a slight readjustment of corrections for other types of collective motion.

Strutinski's theorem [32] relates deformation energies and the actual deformation of energetic minima and barriers to the evolution of the bunching of single-particle levels around the Fermi energy with deformation. Deformation properties are therefore also correlated to the effective mass [33] as the level density of single-particle scales with the latter [34]. As a consequence, it has been observed that the effective mass can have a visible influence on the excitation energies of superdeformed states and fission barrier heights [23].

Starting from these observations, the goals of the present article are

1. to further clarify the correlation between the surface energy coefficient during a parameter adjustment and the multiple choices made for the c.m. correction in the literature;
2. to further analyze the role of the isoscalar effective mass for fission barriers and its correlation with the surface energy coefficient.

To this aim, we constructed new series of parametrizations that are adjusted with each of the three different treatments of the c.m. correction terms mentioned above, and this for three different values of the isoscalar effective mass:  $m_0^*/m = 0.70, 0.80$  and  $0.85$ .

This article is organized as follows: Section II defines the form of the Skyrme EDF that will be used for our study, while Sec. III details the fit protocol used to adjust nine series of new parametrizations customized for our study that differ in the scheme for c.m. correction and isoscalar effective mass. Section IV discusses correlations between properties of infinite and semi-infinite matter found for these new fits and proposes a set of "best fits" for each choice of c.m. correction and isoscalar effective mass that are then used in Sec. V for the study of representative fission barriers as well as properties of normal-deformed and superdeformed states of heavy nuclei. Section VI summarizes our findings.

## II. THE ENERGY DENSITY FUNCTIONAL

For the purpose of our study of the impact of the scheme for c.m. correction and the value of the isoscalar effective mass on surface properties of nuclei, we constructed a set of new parametrizations of the standard

Skyrme EDF. As we are interested in surface properties, we omit genuine tensor forces that directly impact only nuclear shell structure [35, 36] and the response to spin- and spin-isospin excitations [37]. We also limit ourselves to the Skyrme EDF at next-to-leading order (NLO) in gradients [38, 39] and to a form where only the coupling constants of the gradientless (leading order) terms in the EDF have a (single) density dependence.

The total energy is given by [1]

$$E_{\text{tot}} = E_{\text{kin}} + E_{\text{Sky}} + E_{\text{Coul}} + E_{\text{pair}} + E_{\text{corr}}, \quad (2)$$

where  $E_{\text{kin}}$  is the kinetic energy,  $E_{\text{Sky}}$  the Skyrme energy that accounts for the binding due to strong interaction in the particle-hole channel,  $E_{\text{Coul}}$  the Coulomb energy,  $E_{\text{pair}}$  the pairing energy and  $E_{\text{corr}}$  is the sum of all corrections for quantal zero-point motion.

The kinetic energy is given by [1]

$$E_{\text{kin}} = \frac{\hbar^2}{2m} \int d^3r \tau_0(\mathbf{r}), \quad (3)$$

where we use same value  $\hbar^2/2m = 20.735530$  MeV fm<sup>2</sup> for protons and neutrons that is obtained by averaging the values of  $\hbar^2/2m_n$  and  $\hbar^2/2m_p$  as obtained from the 2020 recommendations for the nucleon masses by the Particle Data Group [40] and the 2018 CODATA value for  $\hbar c$  [41].

The local Skyrme EDF can be decomposed into isoscalar ( $t = 0$ ) and isovector ( $t = 1$ ) terms that are either constructed out of time-even ("e") densities only and terms that contain time-odd ("o") densities

$$E_{\text{Sky}} = \int d^3r \sum_{t=0,1} \left[ \mathcal{E}_{t,e}(\mathbf{r}) + \mathcal{E}_{t,o}(\mathbf{r}) \right]. \quad (4)$$

We consider here the traditional standard form of the Skyrme EDF for which the time-even and time-odd parts take the form [1]

$$\begin{aligned} \mathcal{E}_{t,e}(\mathbf{r}) = & C_t^{\rho\rho} \rho_t^2(\mathbf{r}) + C_t^{\rho\rho\rho^\alpha} \rho_t^2(\mathbf{r}) \rho_0^\alpha(\mathbf{r}) \\ & + C_t^{\rho\Delta\rho} \rho_t(\mathbf{r}) \Delta\rho_t(\mathbf{r}) + C_t^{\rho\tau} \rho_t(\mathbf{r}) \tau_t(\mathbf{r}) \\ & - C_t^{sT} \sum_{\mu,\nu=x}^z J_{t,\mu\nu}(\mathbf{r}) J_{t,\mu\nu}(\mathbf{r}) \\ & + C_t^{\rho\nabla J} \rho_t(\mathbf{r}) \nabla \cdot \mathbf{J}_t(\mathbf{r}), \end{aligned} \quad (5)$$

$$\begin{aligned} \mathcal{E}_{t,o}(\mathbf{r}) = & C_t^{ss} \mathbf{s}_t^2(\mathbf{r}) + C_t^{ss\rho^\alpha} \mathbf{s}_t^2(\mathbf{r}) \rho_0^\alpha(\mathbf{r}) \\ & + C_t^{s\Delta s} \mathbf{s}_t(\mathbf{r}) \cdot \Delta\mathbf{s}_t(\mathbf{r}) - C_t^{\rho\tau} \mathbf{j}_t^2(\mathbf{r}) \\ & + C_t^{sT} \mathbf{s}_t(\mathbf{r}) \cdot \mathbf{T}_t(\mathbf{r}) + C_t^{\rho\nabla J} \mathbf{s}_t(\mathbf{r}) \cdot \nabla \times \mathbf{j}_t(\mathbf{r}). \end{aligned} \quad (6)$$

For the definition of the local densities and currents entering the Skyrme EDF see for example Ref. [1]. The coupling constants  $C_t^{\rho\tau}$ ,  $C_t^{sT}$ , and  $C_t^{\rho\nabla J}$  appear in both parts of the EDF in order to ensure its Galilean invariance [42]. For the new parametrizations whose adjustment is described in what follows, the coupling constants

of the Skyrme EDF are calculated as the strict HF expectation value of a central + spin-orbit Skyrme interaction, meaning that the resulting bilinear terms in the spin-current tensor density  $J_{t,\mu\nu}(\mathbf{r})$  are kept, as is the strict relation  $C_0^{\rho\nabla J} = 3 C_1^{\rho\nabla J}$  between the isoscalar and isovector spin-orbit coupling constants. In addition, when doing so, the coupling constants of all time-odd terms are linearly dependent on the coupling constants of the time-even terms. Although these relations are necessary to respect the Pauli principle (at least for the non-density-dependent terms), they are not always imposed. Instead, for many parametrizations of Skyrme's EDF, some of the coupling constants are either set to zero or treated as independent ones. For some of the existing parametrizations of the Skyrme EDF, some of the time-odd terms in Eq. (6) have to be dropped in order to avoid numerical finite-size instabilities [43–45]. As will be explained in Sec. III, the adjustment protocol for the parametrizations constructed for our study ensures that none of such instabilities appear at densities that are probed in finite nuclei.

The Coulomb energy of a Slater determinant is given by the sum of a direct and an exchange term  $E_{\text{Cou}} = E_{\text{Cou}}^{(d)} + E_{\text{Cou}}^{(e)}$  that take the form

$$E_{\text{Cou}}^{(d)} = \frac{e^2}{2} \iint d^3r_1 d^3r_2 \frac{\rho_{\text{ch}}(\mathbf{r}_1) \rho_{\text{ch}}(\mathbf{r}_2)}{|\mathbf{r}_1 - \mathbf{r}_2|}, \quad (7)$$

$$E_{\text{Cou}}^{(e)} = -\frac{e^2}{4} \iint \left[ \rho_{\text{ch}}(\mathbf{r}_1, \mathbf{r}_2) \rho_{\text{ch}}(\mathbf{r}_2, \mathbf{r}_1) + \mathbf{s}_{\text{ch}}(\mathbf{r}_1, \mathbf{r}_2) \cdot \mathbf{s}_{\text{ch}}(\mathbf{r}_2, \mathbf{r}_1) \right] \frac{d^3r_1 d^3r_2}{|\mathbf{r}_1 - \mathbf{r}_2|}, \quad (8)$$

with  $e^2 = 1.439964 \text{ MeV fm}$  being the square of the unit charge [41] and  $\rho_{\text{ch}}$  and  $\mathbf{s}_{\text{ch}}$  representing, respectively, the scalar and vector charge densities. As often done for the calculation of the Coulomb energy and fields, we neglect the intrinsic charge distribution of nucleons and use point-proton densities instead.

While the direct term only depends on local one-body densities, the exchange term depends on the full one-body non-local densities  $\rho_p(\mathbf{r}_1, \mathbf{r}_2)$  and  $\mathbf{s}_p(\mathbf{r}_1, \mathbf{r}_2)$ . As we consider only properties of doubly-magic nuclei during the parameter adjustment that can be calculated with a spherical code in which this term can be treated at acceptable numerical cost, the Coulomb exchange energy and its contribution to the mean fields are calculated exactly for this task. When calculating properties of deformed nuclei and fission barriers in a Cartesian 3d code, however, the exact numerical treatment of  $E_{\text{Cou}}^{(e)}$  becomes unacceptably costly and the numerically much more efficient Slater approximation that yields a local energy density,

$$E_{\text{Cou}}^{(e,S)} = -\frac{3e^2}{4} \left( \frac{3}{\pi} \right)^{1/3} \int d^3r [\rho_{\text{ch}}(\mathbf{r})]^{4/3}, \quad (9)$$

is used instead. As analyzed in Refs. [46–48], using the Slater approximation introduces only a small error of the

order of 3 % on the Coulomb exchange energy that only mildly depends on deformation.

For the doubly-magic nuclei entering the parameter adjustment, the HFB treatment of pairing correlations breaks down such that these calculations are performed at the HF level. When calculating deformed open-shell nuclei and fission barriers, however, pairing correlations have to be considered. The scheme employed for this task will be described in Sec. V B.

In the present work,  $E_{\text{corr}}$  is limited to the approximate correction for the c.m. motion and is given by the expectation value of the operator defined in Eq. (1)

$$E_{\text{corr}} = -E_{\text{c.m.}} = -E_{\text{c.m.}}^{(1)} - E_{\text{c.m.}}^{(2)} = -\frac{\langle \hat{\mathbf{P}}^2 \rangle}{2mA}. \quad (10)$$

The c.m. correction can be written as the sum of a one-body ( $E_{\text{c.m.}}^{(1)}$ ) and a two-body ( $E_{\text{c.m.}}^{(2)}$ ) contribution, see Eq. (1). The former is simply proportional to the free kinetic energy

$$E_{\text{c.m.}}^{(1)} = \frac{E_{\text{kin}}}{A} = \frac{\hbar^2}{2mA} \int d^3r \tau_0(\mathbf{r}), \quad (11)$$

whereas the two-body contribution has to be expressed either through gradients acting on the product of non-local densities or as a weighted sum over products of off-diagonal matrix elements of the momentum operator, see Ref. [14] for the detailed expression. While  $E_{\text{c.m.}}^{(1)}$  is trivial to calculate numerically at essentially no cost through Eq. (11), the numerical calculation of  $E_{\text{c.m.}}^{(2)}$  and the corresponding contribution to the single-particle Hamiltonian are much more expensive. When working with otherwise local EDFs, the two-body c.m. correction becomes in fact the single most costly contribution to the energy, in particular when self-consistently including its contribution to the single-particle Hamiltonian.

This difference in computational cost, together with the effort necessary to implement the comparatively complicated expressions for its contribution to the total energy and the single-particle Hamiltonian, are the main motivation why  $E_{\text{c.m.}}^{(2)}$  has been omitted for the vast majority of parametrizations of Skyrme's EDF, a practice that started long ago [49].

Skyrme's EDF is not the only flavor in use. Both Fayans' EDF [50, 51], and the SeaLL1 EDF of Ref. [52] are used and adjusted without any c.m. correction at all. The Barcelona-Catania-Paris-Madrid (BCPM) EDF [53, 54] employs the analytical estimate of Ref. [55] for the full c.m. correction. All of these EDFs have in common that they are local. For non-local EDFs that consider the exchange terms from a finite-range force, there is no computational reason to neglect the two-body part of the c.m. correction anymore. Consequently, beginning with D1S [11], all parametrizations of Gogny's force have been adjusted with the full c.m. correction, although the two-body part is not always used in production calculations [56]. Likewise, the parametrizations of the finite-range EDF based on the Michigan-3-Yukawa (M3Y) force



by Nakada [57] as well as the recently introduced regularized finite-range pseudo-potential [58–61] also employ the full c.m. correction.

For the parametrizations considering the full c.m. correction that we adjusted for the present study, we chose a compromise between phenomenology and computational cost. We treated  $E_{c.m.}^{(2)}$  self-consistently during the parameter adjustments, since doing so is not excessively costly in spherical symmetry and is particularly simple in the absence of pairing. The Cartesian 3d calculations of deformed nuclei and fission barriers that we describe below, only account for  $E_{c.m.}^{(2)}$  perturbatively for reasons of computational cost. This means in practice that we drop the corresponding contribution to the single-particle Hamiltonian and only add  $E_{c.m.}^{(2)}$  to the total energy, in Eq. (2), after convergence. Calculating at least part, if not all, of the c.m. correction perturbatively is in fact the strategy followed for many of the existing applications that do consider the full c.m. correction [22, 23, 28, 29, 31, 56, 62, 63].

We note in passing that the center-of-mass correction approximates the energy gain from restoration of translational invariance of the nuclear state [64–69], but even including it self-consistently in the variational equations does by no means even approximatively restore these symmetries in the wave function. Other observables such as the density distributions and its moments therefore also have to be explicitly corrected for spurious c.m. motion as well [70–73]. For further discussion of the c.m. correction to the binding energy and its treatment we refer to Refs. [14–16, 55, 74–82] and references therein.

### III. PARAMETER ADJUSTMENT

#### A. General idea

We have adjusted three sets of parametrizations with different treatment of the c.m. correction. For the first set, we have omitted the first and second term of (1), such that there is no c.m. correction at all. These will be labeled by 1F2F(X) in what follows. For the second set of parametrizations, the correction was limited to its one-body part only, i.e. the term (11). These will be labeled by 1T2F(X) in what follows. Finally, the third set of parametrizations was adjusted considering both the one-body and two-body terms in the c.m. correction. These will be labeled by 1T2T(X). For each choice for the c.m. correction we constructed a series of parameter sets with isoscalar effective mass  $m_0^*/m = 0.70, 0.80$  and  $0.85$ , which will be indicated in the parenthesis (X) of the label. For each of the resulting nine combinations of scheme for c.m. correction and effective mass, we constructed a series of parametrizations with a constraint on the surface energy coefficient  $a_{\text{surf}}$  with target values varying between 15.5 MeV to 20.0 MeV. For that purpose,  $a_{\text{surf}}$  is calculated in the computationally-friendly Modified Thomas-Fermi (MTF) approximation [83] that

was already used earlier for the same purpose in the construction of the SLy5sX parametrizations of Ref. [9].

#### B. Penalty function

To adjust the coupling constants of the Skyrme EDF of Eqs. (5) and (6), we have minimized a penalty function that considers data on doubly-magic nuclei and phenomenological properties of infinite nuclear matter (INM).

This adjustment is achieved by minimizing a penalty function, hereafter denoted  $\chi^2$ , that is a sum of squares of differences between calculated quantities  $\mathcal{O}_i$  and their target values  $\mathcal{O}_i^{(0)}$ . These are weighted by the inverse of the square of parameters  $\Delta\mathcal{O}_i$  that can be regarded as tolerances for the desired final deviation

$$\chi^2 = \sum_i \left( \frac{\mathcal{O}_i - \mathcal{O}_i^{(0)}}{\Delta\mathcal{O}_i} \right)^2. \quad (12)$$

Reaching the minimum of the objective function does not guarantee that all quantities  $\mathcal{O}_i$  fall inside of the interval  $[\mathcal{O}_i^{(0)} - \Delta\mathcal{O}_i, \mathcal{O}_i^{(0)} + \Delta\mathcal{O}_i]$ .

Two quantities characterizing infinite nuclear matter are not constrained through the minimization of the penalty function (12), but are enforced to take a definite value. These quantities are the saturation density, which is fixed to  $\rho_{\text{sat}} = 0.16 \text{ fm}^{-3}$ , and the isoscalar effective mass  $m_0^*/m$  that is set to the required value for each series of fits. Since the objective function involves several properties of nuclear matter at saturation, fixing  $\rho_{\text{sat}}$  in this way greatly stabilizes the parameter adjustment.

Adapting the protocol used for adjusting parametrizations of Refs. [9], the set of constraints considered here is the following:

- Total energies of seven doubly-magic nuclei from AME20 [84], listed in Table I.
- The difference in binding energy  $\Delta E$  between  $^{56}\text{Ni}$  and  $^{40}\text{Ca}$  depends strongly on the distance between the neutron  $1f_{7/2}$  and  $1d_{3/2}$  orbitals and therefore on the strength of the spin-orbit term. We have put a constraint on  $\Delta E$  with a target value of 141.920 MeV and a tolerance of 1 MeV to constrain this term.
- Properties of symmetric infinite nuclear matter in the vicinity of the saturation point: energy per nucleon  $\varepsilon_{\text{sat}}$ , symmetry energy coefficient  $J$  and its slope  $L$  with target values and tolerances given on Table II. The choice of target values for  $J$  and  $L$  is motivated by microscopic calculations in infinite nuclear matter [85].
- Energy per nucleon in infinite neutron matter. We used values calculated for the potentials UV14 plus UVII (see Table III in [86]) at densities up to  $0.45 \text{ fm}^{-3}$  with a tolerance of 25 %.

- Energy per nucleon in polarized infinite nuclear matter and neutron matter. Adjustment of parameters sometimes leads to the appearance of a bound state in symmetric polarized matter or to the collapse of polarized neutron matter at high density. To avoid this type of results, we used the constraints of  $E/A = 12.52$  MeV at density  $0.1 \text{ fm}^{-3}$  in polarized nuclear matter and  $E/A = 40.10$  MeV in polarized neutron matter at the same density (taken from Ref. [87]) both with a large tolerance of 25 %.
- To avoid the appearance of finite-size instabilities [45] we used the linear response method [44] to enforce that the lowest poles of the response function remain above  $\rho_{\min} = 1.2 \times \rho_{\text{sat}} \simeq 0.192 \text{ fm}^{-3}$  in symmetric nuclear matter for all spin and isospin channels (except for the case of the spinodal instability at low density in the  $(S, T) = (0, 0)$  channel) and above half of this density in pure neutron matter, see Ref. [45]. An instability is characterized by a divergence of the response function, or a zero of its inverse, for given values of the density  $\rho_0$  and the transferred momentum  $q$  between particles and holes. To push any instability above  $\rho_{\min}$ , we calculate the sum of the modulus of the inverse of the response function at  $\rho_0 = \rho_{\min}$  for equally spaced values of  $q$  from 0 to  $9 \text{ fm}^{-1}$  with  $\delta q = 0.01 \text{ fm}^{-1}$  and require the result, in all  $(S, T)$  channels to be greater than 0 using an asymmetrical constraint as described by equation (58) in [60]. These strong constraints allow us to avoid the appearance of finite-size instabilities for all parametrizations constructed, as we checked explicitly afterwards.
- The surface energy coefficient calculated in semi-infinite nuclear matter using the MTF approximation was constrained to a series of values in steps of 0.2 MeV with a tolerance of 0.01 MeV. Nine series of interactions have been thus constructed labeled with their {center of mass, isoscalar effective mass, MTF surface energy coefficient} options. Beyond these ones, nine other interactions (only labeled with their {center of mass, isoscalar effective mass} options) have been built omitting the constraint of the surface coefficient in order to have in each case the exact minimum of the penalty function.

The power  $\alpha$  of the density dependence in Eq. (5) is not considered as a free parameter but set to  $\alpha = 1/6$ . It is well known that with standard NLO Skyrme functionals and for given values of saturation density and energy per nucleon in symmetric infinite nuclear matter, the isoscalar effective mass  $m_0^*/m$  and the compression modulus  $K_\infty$  are not independent quantities [88]. The choice to set  $\alpha$  to 1/6 allows to vary the isoscalar effective mass while keeping  $K_\infty$  in a acceptable interval, see Sec. IV C 2. With this choice for  $\alpha$  and for the cho-

Table I. Binding energies (in MeV) of doubly-magic nuclei used to constrain the parameters of the functional. Note that the value for  $^{78}\text{Ni}$  is extrapolated. The last column gives the tolerances (in MeV) used in the fit protocol.

Nucleus	$E_{\text{tot}}$	Tolerance
$^{40}\text{Ca}$	-342.034	$\pm 1.0$
$^{48}\text{Ca}$	-415.983	$\pm 1.0$
$^{56}\text{Ni}$	-483.954	$\pm 1.0$
$^{78}\text{Ni}$	-642.522	$\pm 2.0$
$^{100}\text{Sn}$	-824.995	$\pm 1.0$
$^{132}\text{Sn}$	-1102.675	$\pm 1.0$
$^{208}\text{Pb}$	-1635.862	$\pm 1.0$

Table II. Properties of symmetric nuclear matter in the vicinity of saturation used to constrain the EDF parameters. All quantities are in MeV.

Property	Target value	Tolerance
$\varepsilon_{\text{sat}}$	-16.0	$\pm 0.1$
$J$	32	$\pm 1$
$L$	50	$\pm 5$

sen fixed values for  $\rho_{\text{sat}}$  and  $m_0^*/m$ , the EDF contains in total seven free parameters that have to be adjusted.

All nuclei considered for the fit of parameters are doubly-magic spherical nuclei. It is assumed that pairing correlations do not contribute to those, such that calculations are done at the HF approximation. Their numerical calculations was performed on a radial mesh in coordinate space with 80 points with a constant spacing of 0.25 fm using the code FINRES<sub>4</sub> [89].

## IV. CORRELATIONS BETWEEN NUCLEAR MATTER PROPERTIES

### A. From EDF parametrization to Liquid-drop model

As has been pointed out before [8, 14], the physical origin of the correlation between choices made for the center-of-mass correction and nuclear surface properties on the one hand, and of the correlations between surface properties and the bulk properties of nuclear matter on the other hand, can be understood when looking at binding energies obtained from a liquid-drop model (LDM) whose parameters are set to the values predicted by the parametrizations of EDF models.

To this aim, we employ the following form for the LDM energy of a nucleus with  $N$  neutrons and  $Z$  protons

$$E_{\text{LDM}}(N, Z) = (a_{\text{vol}} + a_{\text{sym}} I^2) A + (a_{\text{surf}} + a_{\text{ssym}} I^2) A^{2/3}$$

$$+ \frac{3e^2}{5r_0} \frac{Z^2}{A^{1/3}} - \frac{3e^2}{4r_0} \left( \frac{3}{2\pi} \right)^{2/3} \frac{Z^{4/3}}{A^{1/3}}, \quad (13)$$

where  $A = N + Z$  is the mass number and  $I = \frac{N-Z}{N+Z}$  the isospin asymmetry. The coefficients of the volume ( $a_{\text{vol}}$ ) and volume symmetry ( $a_{\text{sym}}$ ) energy can be related to properties of infinite nuclear matter at the saturation point, whereas the coefficients of the surface ( $a_{\text{surf}}$ ) and surface symmetry ( $a_{\text{ssym}}$ ) energy are connected to properties of semi-infinite nuclear matter (SINM). The radius constant  $r_0$  is determined by the nuclear matter saturation density  $\rho_{\text{sat}}$  through  $r_0^3 = 3/(4\pi\rho_{\text{sat}})$ . Constructing an LDM that accurately approximates the binding energies of a self-consistent model would require additional terms [90], but the simplicity of Eq. (13) is sufficient for our study.

### B. Further analysis of the correlations between the values for $a_{\text{surf}}$ obtained through different schemes

We recall that there are several approaches to calculate the surface and surface symmetry energy coefficients of an EDF that differ in their strategy and computational cost. A widely used procedure is to extract  $a_{\text{surf}}$  and  $a_{\text{ssym}}$  from calculations of the model system of SINM [9, 91]

$$a_{\text{surf,eff}}(I) = a_{\text{surf}} + a_{\text{ssym}} I^2 \\ = \lim_{L \rightarrow \infty} \left\{ \left[ 4\pi r_0^2 \int_{-L/2}^{+L/2} dz \mathcal{E}(z) \right] - E_{\text{ref}}(I, L) \right\} \quad (14)$$

in a one-dimensional box of length  $L$ , where  $\mathcal{E}(z)$  is the energy density of SINM calculated at an asymmetry  $I$  and  $E_{\text{ref}}(I)$  is a reference volume energy that depends on nucleon numbers.

The value of  $a_{\text{surf}}$  can be determined from a single SINM calculation of symmetric matter ( $I = 0$ ), whereas the extraction of  $a_{\text{ssym}}$  requires at least two calculations at different asymmetries  $I$ .

The SINM calculations can either be performed in some variant of the semi-classical Thomas-Fermi approximation or in the quantal Hartree-Fock framework. While each of these schemes yields a slightly different value for  $a_{\text{surf}}$ , it has been argued in Ref. [9] that they are basically equivalent for the purpose of constraining effective interactions as long as the value that  $a_{\text{surf}}$  is constrained to is suitably chosen.

To put the earlier analysis of Ref. [9] onto a wider basis of parametrizations that systematically cover a wide interval of  $a_{\text{surf}}$  values, and to confirm that the main conclusions of this study also apply when making the choices of the fit protocol described above, we compare values for  $a_{\text{surf}}$  extracted from calculations of semi-infinite nuclear matter performed within either the Hartree-Fock

(HF), within the semi-classical Extended Thomas-Fermi (ETF) approach up to order  $\hbar^4$ , or within the Modified Thomas-Fermi (MTF) approach. For details about these methods we refer to Ref. [9] and references therein, and recall only their main characteristics. In a quantal HF calculation of SINM, one minimizes the total energy as calculated from the self-consistent densities of a Slater determinant of single-particle states. In the ETF calculation, the kinetic and spin-current densities entering the Skyrme EDF are developed into functionals of the local density and its derivatives. The surface energy is then minimized with respect to the parameters of a prescribed profile for the local densities of protons and neutrons. Finally, the MTF approach is based on the observation that a slight modification of the relative weights of the semi-classical expansion of the kinetic density in a limited ETF expansion up to order  $\hbar^2$  makes the system integrable for standard Skyrme EDFs at NLO [83, 92], such that the optimal density profile is obtained without a variational calculation [9, 92]. The computational cost is thereby considerably reduced when going from HF to ETF and then to MTF.

The semi-classical calculations reported here were performed with the same tools as those reported in Ref. [9], whereas the HF calculations were made with a newly designed code [93] that yields results for  $a_{\text{surf}}$  that are identical to those reported in Ref. [9] within typically 0.01 MeV.

For the surface symmetry energy coefficient  $a_{\text{ssym}}$ , the discussion will be limited to values extracted from HF calculations of SINM. The reason is that there are several different choices for the reference energy  $E_{\text{ref}}(I, L)$  entering Eq. (14) that are frequently used in the literature for its extraction and that lead to different values of  $a_{\text{ssym}}$  when extracted from the same calculations of semi-infinite matter. As  $a_{\text{ssym}}$  has not been constrained during the adjustment of the parameter sets discussed here, we will limit its analysis to one scheme to calculate  $a_{\text{ssym}}$  and to one procedure to extract it. For the latter, we choose the thermodynamical definition [94, 95], where the reference energy  $E_{\text{ref}} = \epsilon_{\text{F},n} N_{\text{box}} + \epsilon_{\text{F},p} Z_{\text{box}}$  is provided by the Fermi energies of protons and neutrons, respectively, and the number of protons and neutrons that enter the calculation of the energy density  $\mathcal{E}(z)$  in Eq. (14).

Figure 1 shows the differences  $\Delta a_{\text{surf}}^{\text{MTF}} = a_{\text{surf}}^{\text{MTF}} - a_{\text{surf}}^{\text{HF}}$  and  $\Delta a_{\text{surf}}^{\text{ETF}} = a_{\text{surf}}^{\text{ETF}} - a_{\text{surf}}^{\text{HF}}$  between the values of the surface energy coefficient extracted from SINM calculations with either of the semi-classical ETF and MTF approaches and its value obtained from a HF calculation for all nine series of fits by systematically varying  $a_{\text{surf}}^{\text{MTF}}$  and the isoscalar mass  $m_0^*/m$ .

The difference  $\Delta a_{\text{surf}}^{\text{MTF}}$  between MTF and HF results shows a clear dependence on  $m_0^*/m$ , which was already hinted in the results discussed in Ref. [9]: the difference decreases with increasing effective mass. This can be explained by the nature of the MTF approximation that modifies the dependence of the kinetic density  $\tau[\rho(\mathbf{r})]$  on the local density  $\rho(\mathbf{r})$  in the semi-classical approximation

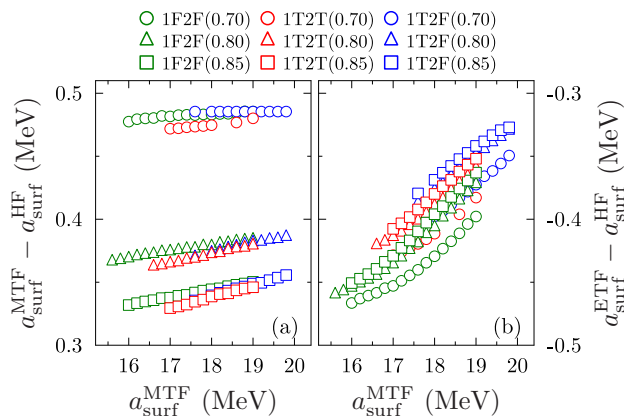


Figure 1. Differences between the surface energy coefficient as calculated in either the MTF (panel (a)) or ETF (panel (b)) approach and its HF value for the nine series of parametrizations as indicated as a function of their  $a_{\text{surf}}^{\text{MTF}}$ . Different colors indicate different schemes for c.m. correction, whereas different markers indicate different isoscalar effective mass  $m_0^*/m$ .

in such a way that the problem becomes integrable [9, 83]: the smaller the isoscalar effective mass, the larger becomes the relative contribution from EDF terms that contain products of  $\tau(\mathbf{r})$  and other densities compared to the free kinetic energy that is linear in  $\tau(\mathbf{r})$ . It appears that the MTF approximation works better for terms of the latter type than those of the former.

For each fixed value of  $m_0^*/m$ , there also is a very mild dependence of  $\Delta a_{\text{surf}}^{\text{MTF}}$  on the actual value of  $a_{\text{surf}}^{\text{MTF}}$ .

For comparison, and to complement the discussion of Ref. [9], Fig. 1 also shows the difference  $\Delta a_{\text{surf}}^{\text{ETF}}$  between ETF and HF results. Although the deviation is not the same for all, its spread is much smaller, meaning that the ETF approximation works much more consistently for parametrizations with different  $m_0^*/m$ . The difference, however, depends more strongly on the value of  $a_{\text{surf}}^{\text{MTF}}$  that the parameter set is constrained to than it is the case for  $\Delta a_{\text{surf}}^{\text{MTF}}$ . At fixed  $a_{\text{surf}}^{\text{MTF}}$  the deviation is systematically slightly smaller for parametrizations with larger  $m_0^*/m$ . There also is a slight systematic dependence of  $\Delta a_{\text{surf}}^{\text{ETF}}$  on the scheme used for the c.m. correction, where the deviation is smallest for parameter sets adjusted with the full 1T2F scheme and largest for those adjusted with the 1F2F scheme.

### C. Penalty function and correlations between nuclear matter properties

#### 1. Surface properties

Figure 2 shows the penalty function for all parametrizations out of the nine series of fits with systematically varied  $a_{\text{surf}}^{\text{MTF}}$  and  $m_0^*/m$ . We focus first on panel (a) that shows the penalty function as a function of  $a_{\text{surf}}^{\text{MTF}}$ .

There is a clear correlation between the value of  $a_{\text{surf}}^{\text{MTF}}$

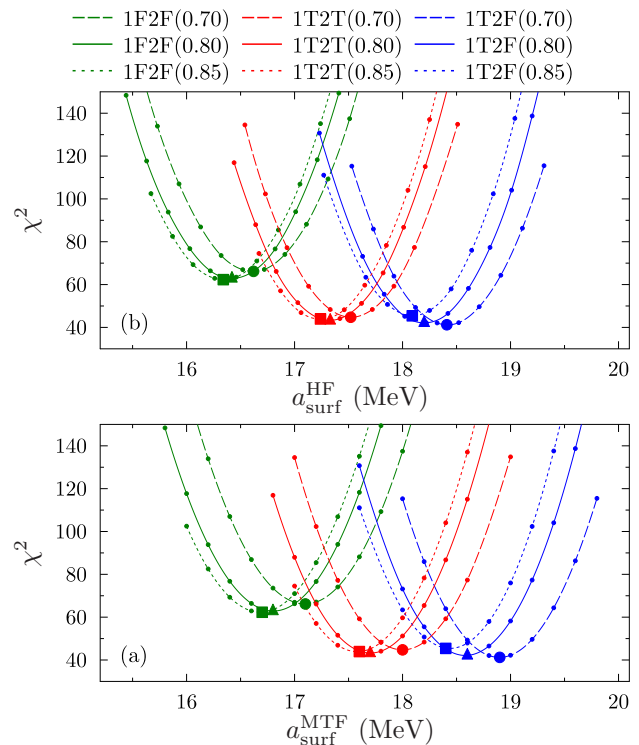


Figure 2. Penalty function  $\chi^2$  for all parametrizations out of the nine series of fits as a function of their value of  $a_{\text{surf}}^{\text{MTF}}$  (panel (a)) and  $a_{\text{surf}}^{\text{HF}}$  (panel (b)). The dots indicate the parametrizations with systematically varied  $a_{\text{surf}}^{\text{MTF}}$  whose properties are studied in Sec. IV C. For each of the nine series, the minimum of  $\chi^2$  is indicated by a filled marker. The properties of the corresponding “best fit” parametrizations are studied beginning with Sec. IV D.

at the minimum of the penalty function and the scheme of c.m. correction: for parameter sets using the popular 1T2F scheme, the minimum is can be found near 18.6 MeV, while for parameter sets using the full 1T2T scheme it is located around 17.7 MeV, and for parameter sets without any c.m. correction (1F2F) one finds it at 16.8 MeV. The position of the minimum also depends in a more limited way on the effective mass  $m_0^*/m$ : with increasing effective mass, the minimum shifts to smaller values of  $a_{\text{surf}}^{\text{MTF}}$ . The different locations of the minima in terms of the surface energy of the parametrizations are quite meaningful: a difference of 1 MeV in  $a_{\text{surf}}$  typically changes the outer fission barrier heights of actinide nuclei by about 4 MeV, a value that is comparable to the experimentally determined barriers for these nuclei. We illustrate this in Sec. V but it was already pointed out repeatedly in earlier studies [9, 13, 96, 97].

Previous studies conducted in Refs. [9, 13] have shown that, for nuclear EDFs that do not consider other quantal corrections<sup>2</sup> than possibly a c.m. correction as done here,

<sup>2</sup> In the presence of additional strongly deformation dependent



the optimal values of  $a_{\text{surf}}^{\text{MTF}}$  for a satisfying description of the deformation properties of heavy nuclei fall into an interval between 17.6 and 18.0 MeV. It is striking to see that the minimum of the penalty function  $\chi^2$  as a function of  $a_{\text{surf}}^{\text{MTF}}$  is situated precisely in this interval for the parametrizations of the 1T2T type, whereas it is well above for parametrizations of 1T2F type and well below for parametrizations of 1F2F type.

The systematic differences between the values of  $a_{\text{surf}}^{\text{MTF}}$  at the minima of the penalty function explain why many of the existing parametrizations that use the popular 1T2F recipe systematically fail to describe fission barrier heights and grossly overestimate them [9, 14, 17], unless their surface properties are constrained during the parameter adjustment. One representative example is the SLy4d parametrization [18], whose surface properties and fission barriers were discussed in Ref. [9].

It is possible to constrain 1F2F and 1T2F parametrizations to realistic surface properties during the fit, but this comes at the price of a deteriorated description of other observables that enter the penalty function. For example, the SLy5s1 parametrization has  $a_{\text{surf}}^{\text{MTF}} = 18.0$  MeV, but performs comparatively poorly for binding energies of nuclei [13]. Recalling that SLy5s1 is of 1T2F(0.70) type and has been adjusted with a protocol that is almost identical to ours, this finding can be easily understood from panel (a) of Fig. 2. Bringing  $a_{\text{surf}}^{\text{MTF}}$  to a realistic value is only achieved at the expense of other features.

As illustrated by Fig. 1, the offset between the HF and MTF values for  $a_{\text{surf}}$  slightly depends on the isoscalar effective mass of the parametrizations. The change of this offset has as a consequence that, for a given choice of scheme for c.m. correction, the minima of the penalty function  $\chi^2$  for different choices of isoscalar effective mass  $m_0^*/m$  become closer when plotting  $\chi^2$  as a function of  $a_{\text{surf}}^{\text{HF}}$  instead of the value of  $a_{\text{surf}}^{\text{MTF}}$  that the parametrizations were constrained to, see panel (b) of Fig. 2. This observation indicates that the fission barrier heights of optimal fits that employ the same scheme for c.m. correction might depend less on the effective mass than is apparent on panel (a) of Fig. 2, at least if one assumes that  $a_{\text{surf}}^{\text{HF}}$  is the value of the surface energy that is the most directly correlated to the deformation energies obtained in EDF calculations.

For a given nucleus, the effective surface energy coefficient  $a_{\text{surf,eff}}(I)$  of Eq. (14) also depends on its asymmetry  $I$  through the surface symmetry energy coefficient  $a_{\text{ssym}}$ . As a consequence, the correlation between the fission barrier of this nucleus and the value of  $a_{\text{surf}}$  constrained in a parameter fit also depends on the value adopted by

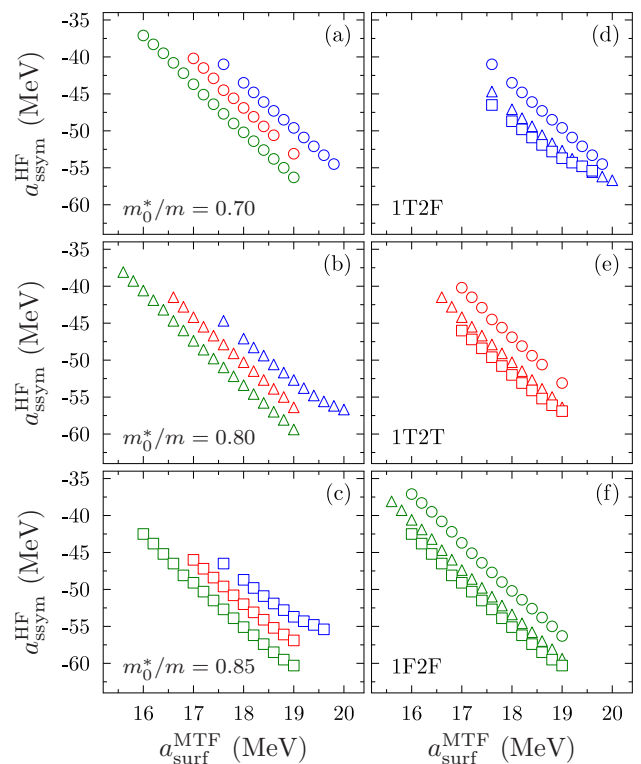


Figure 3. Surface symmetry energy coefficient  $a_{\text{ssym}}^{\text{HF}}$  calculated in HF approximation for all parametrizations out of the nine series of fits, plotted as a function of their value for  $a_{\text{surf}}^{\text{MTF}}$ . Panels (a), (b), and (c) compare parametrizations with same effective mass but different scheme for c.m. correction, whereas panels (d), (e), and (f) compare parametrizations with same scheme for c.m. correction but different effective mass  $m_0^*/m$ .

$a_{\text{ssym}}$  during the parameter fit. As it turns out, for our series of parameter fits the values of  $a_{\text{ssym}}$  are not identical, but also correlated to the value of  $a_{\text{surf}}^{\text{MTF}}$ , the choice of scheme for c.m. correction, and the isoscalar effective mass as illustrated on Fig. 3.

Within each series of our fits, the absolute value of  $a_{\text{ssym}}$  increases with  $a_{\text{surf}}$ . As  $a_{\text{ssym}}$  and  $a_{\text{surf}}$  have in general opposite sign, this dependence keeps the values of  $a_{\text{surf,eff}}(I)$  of very asymmetric nuclei closer together when comparing different parametrizations out of a given series than their difference in  $a_{\text{surf}}$  would suggest.

For a given scheme for c.m. correction, the absolute value of  $a_{\text{ssym}}$  increases with effective mass, typically by about 4 MeV when going from  $m_0^*/m = 0.7$  to  $m_0^*/m = 0.8$ , and by about another 2 MeV when going from  $m_0^*/m = 0.80$  to  $m_0^*/m = 0.85$ . For a given effective mass, the absolute value of  $a_{\text{ssym}}$  increases by about 3 MeV when going from the 1T2F scheme to the 1T2T scheme, and by about another 3 MeV when going from the 1T2T scheme to the 1F2F scheme.

We note in passing that we made an unsuccessful attempt to simultaneously constrain  $a_{\text{surf}}$  and  $a_{\text{ssym}}$  at the MTF level, using an adaptation of the estimate of  $a_{\text{ssym}}$

quantal corrections such as a rotational correction [29, 98, 99], or when considering exact restoration of angular momentum [100, 101], the optimal value of  $a_{\text{surf}}^{\text{MTF}}$  can be substantially different as it only represents the deformation dependence of the interaction energy, but not the deformation dependence of the quantal corrections.

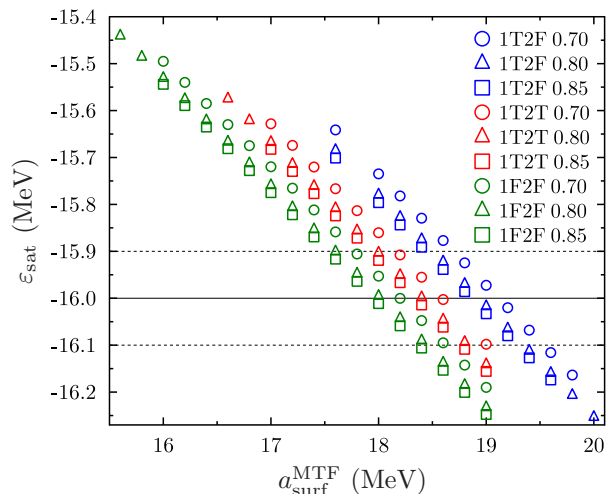


Figure 4. Location of the saturation point: Energy per particle  $\varepsilon_{\text{sat}}$  at the saturation density  $\rho_{\text{sat}}$  of the parametrizations as indicated. The horizontal lines indicate the target value of  $\varepsilon_{\text{sat}}$  and its tolerance in the penalty function.

proposed in Ref. [102]. As it turns out, this cannot be meaningfully done for the NLO Skyrme EDF that we use here: setting  $a_{\text{ssym}}$  to a value that differs significantly from the optimal value for given  $a_{\text{surf}}$  indicated by Fig. 3 pushes the values of some nuclear matter properties far out of their accepted range. Adding  $a_{\text{ssym}}$  to a fit protocol that already fixes  $a_{\text{surf}}$  and aims at realistic bulk properties over-constrains the parameter fit of a Skyrme EDF at NLO. This is not surprising in view of the limited number of independent coupling constants of Eq. (5) that determine nuclear matter properties. It remains to be shown if more general forms of a Skyrme EDF would allow for a fine-tuning of  $a_{\text{ssym}}$  without deteriorating the bulk properties.

## 2. Bulk properties

As it turns out, for a Skyrme EDF at NLO the infinite nuclear matter properties are already strongly correlated to the value of  $a_{\text{surf}}$  even when  $a_{\text{ssym}}$  is left unconstrained.

Figure 4 displays the energy per particle  $\varepsilon_{\text{sat}}$  at saturation density of homogeneous INM. This property equals the volume energy coefficient  $a_{\text{vol}} = \varepsilon_{\text{sat}}$  of the liquid drop model. We constrain it in our parameter fits to  $\varepsilon_{\text{sat}} = (16.0 \pm 0.1)$  MeV, although this target value is incompatible with the most extreme values of  $a_{\text{surf}}$  covered by our fits. In general, large (positive) values of  $a_{\text{surf}}$  correspond to large negative values of  $a_{\text{vol}}$  and vice versa. This correlation can be understood when considering the role of the surface energy for nuclear masses in the liquid-drop model. Since the surface energy  $a_{\text{surf}} A^{2/3}$  reduces nuclear binding, the coefficients of other terms in the liquid-drop model have to change in a way that increases their contribution to the total energy in order to

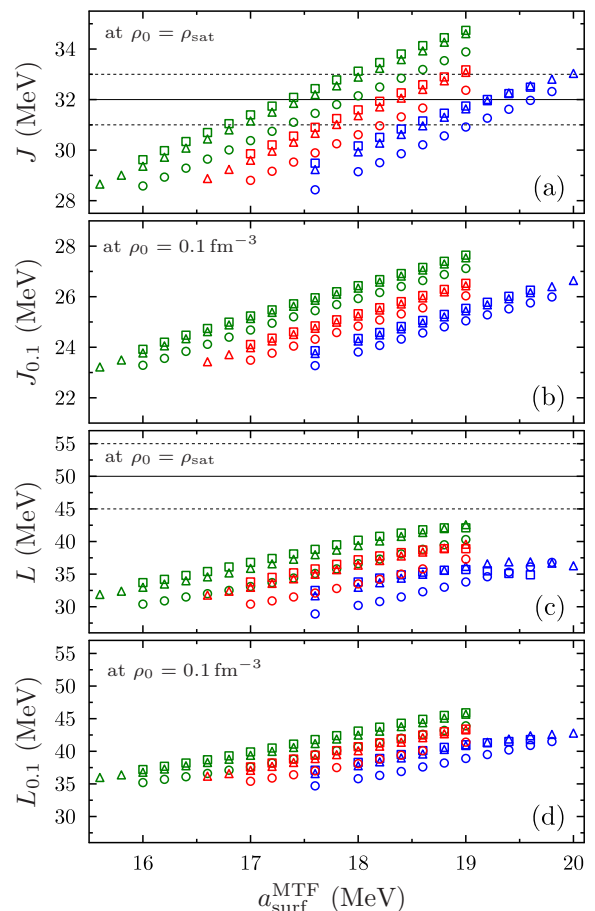


Figure 5. Symmetry energy  $J$  and its slope  $L$  at saturation density  $\rho_{\text{sat}}$  and at  $\rho_0 = 0.1 \text{ fm}^{-3}$  (see text) for the parametrizations as indicated. The horizontal lines indicate the target values of  $J$  and  $L$  in the penalty function, as well as their respective tolerances. Colors and symbols as in Fig. 4.

keep binding energies of finite nuclei roughly constant. The volume term is apparently one of them. Not surprisingly,  $\varepsilon_{\text{sat}}$  is close to 16.0 MeV for parametrizations with a value of  $a_{\text{surf}}^{\text{MTF}}$  near the minimum of the penalty function for all nine series of fits.

Because of the different  $A$  (and  $I$ ) dependence of their contribution to total binding energy, one term can of course not perfectly compensate for the change of the other, such that multiple nuclear matter properties change when varying  $a_{\text{surf}}^{\text{MTF}}$ . And indeed, as can be seen from Fig. 5, the volume symmetry energy coefficient  $a_{\text{sym}}$  of the liquid-drop model, which equals the symmetry energy of symmetric matter

$$S(\rho_0) = \frac{1}{2} \frac{\partial^2 \mathcal{E}}{\partial I^2 \partial \rho_0} \quad (15)$$

at saturation density, i.e.

$$a_{\text{sym}} = J = S(\rho_{\text{sat}}), \quad (16)$$

is also evolving with the constrained value of  $a_{\text{surf}}^{\text{MTF}}$  over a wide range between roughly 28.5 and 35 MeV. Within

each series of fits,  $J$  almost linearly increases with  $a_{\text{surf}}^{\text{MTF}}$ . While the slope of this dependence is almost the same within all nine sets of fits, there is a large offset between different series that strongly depends on the choice made for the scheme for c.m. correction (indicated by different symbols in Fig. 5) and to a much lesser degree also on the value for the effective mass  $m_0^*/m$  (indicated by different colors).

In addition, Fig. 5 displays the slope of the symmetry energy at the saturation point

$$L = 3\rho_0 \left. \frac{\partial S(\rho_0)}{\partial \rho_0} \right|_{\rho_0=\rho_{\text{sat}}}, \quad (17)$$

as well as the values of the symmetry energy and its slope at  $\rho = 0.1 \text{ fm}^{-3}$  denoted  $J_{0.1}$  and  $L_{0.1}$ . It has been pointed out that the slope  $L$  is correlated with characteristics of asymmetric nuclear systems at densities that are very different from saturation density. Examples for such systems are finite nuclei with neutron skins, heavy-ions in collision, or neutron stars [85, 103–106].

One can observe that the values obtained for  $L$  are well outside of the interval defined by the target value and the tolerance [45, 55] (in MeV). This feature reveals that the EDF (6) does not have the required flexibility to satisfy all constraints listed in Sec. IIIB within the tolerance intervals. Even if the values obtained for  $L$  are rather low to correctly reproduce global properties of neutron stars, we can consider that this will not impact too much the properties of finite nuclei besides, possibly, neutron skins, since these values are close to the one obtained with other successful interaction such as D1S [99].

Besides the correlations of nuclear matter properties with observables, there possibly are other correlations that are intrinsic to nuclear models and the protocols used to adjust them. Some of the latter correlations might be spurious consequences of limitations of the models or of the lack of data that allow to isolate the role of each of the properties of nuclear matter. For example, it was pointed out early on that the values of  $L$  and  $J$  of nuclear EDFs are closely correlated [107], which is also found here. Similar correlations are also found between other elements of the symmetry energy [108–110], but their analysis is usually limited to bulk properties of infinite matter. It has also been pointed out that the volume and surface symmetry energy are correlated by nuclear masses through Eq. (13), see for example Refs. [8, 111]. Nuclear masses also correlate the surface symmetry energy with  $\varepsilon_{\text{sat}}$ , such that their sum is nearly constant along the valley of stability [8]. Unfortunately, the portion of the nuclear chart explored experimentally so far is too small to fix the symmetry parameters in a pure LDM model [112].

It has also been argued that finite nuclei actually mainly constrain the symmetry energy  $J_{\rho_0} = S(\rho_0)$  and its slope  $L_{\rho_0}$  at sub-saturation densities around  $\rho_0 \simeq 0.1 \text{ fm}^{-3}$  [104, 113–115]. And indeed, as indicated by Fig. 5, for our nine series of fits the values of  $J_{0.1}$  and  $L_{0.1}$  are somewhat closer one to each other than those of the

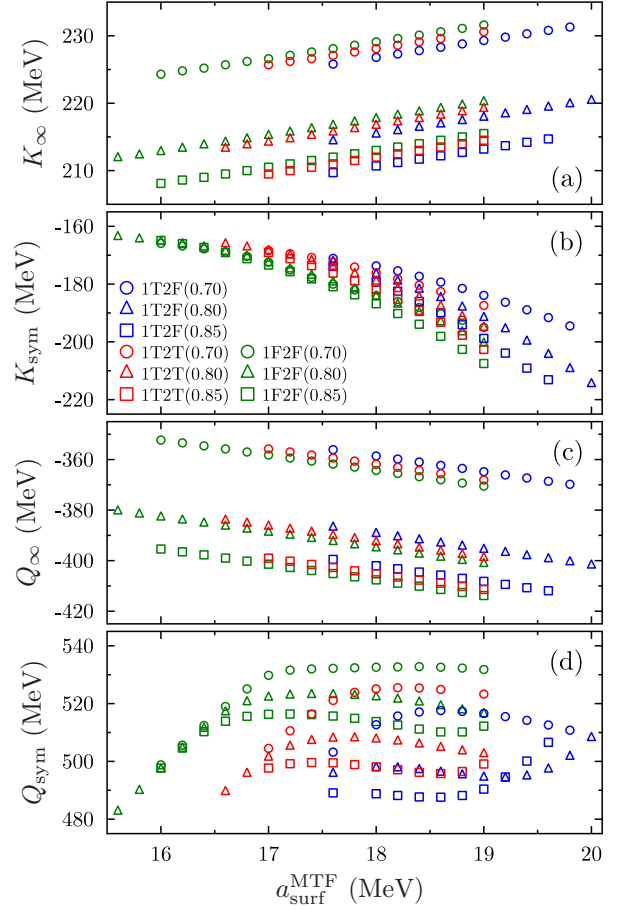


Figure 6. Higher-order derivatives  $K_\infty$ ,  $Q_\infty$ ,  $K_{\text{sym}}$ , and  $Q_{\text{sym}}$  of the binding energy per particle at saturation density  $\rho_{\text{sat}}$ . Colors and symbols as on Fig. 4.

corresponding quantity at  $\rho_{\text{sat}}$ . The spread of these values, however, remains larger than what is typically found for parametrizations whose  $a_{\text{surf}}$  is not constrained, see for example Ref. [113] and Table III in what follows.

Figure 6 displays four higher-order characteristics of infinite matter, which are its incompressibility

$$K_\infty = 9\rho_0^2 \left. \frac{\partial^2}{\partial \rho_0^2} \frac{\mathcal{E}}{\rho_0} \right|_{\rho_0=\rho_{\text{sat}}}, \quad (18)$$

and skewness

$$Q_\infty = 27\rho_0^3 \left. \frac{\partial^3}{\partial \rho_0^3} \frac{\mathcal{E}}{\rho_0} \right|_{\rho_0=\rho_{\text{sat}}}, \quad (19)$$

at saturation, as well as the curvature

$$K_{\text{sym}} = 9\rho_0^2 \left. \frac{\partial^2 S(\rho_0)}{\partial \rho_0^2} \right|_{\rho_0=\rho_{\text{sat}}} \quad (20)$$

and skewness

$$Q_{\text{sym}} = 27\rho_0^3 \left. \frac{\partial^3 S(\rho_0)}{\partial \rho_0^3} \right|_{\rho_0=\rho_{\text{sat}}} \quad (21)$$

of the symmetry energy. Together with the already discussed coefficients  $\varepsilon_{\text{sat}}$ ,  $J$ , and  $L$ , these parametrize the density dependence of the energy per particle and the symmetry energy of symmetric matter around the saturation point in terms of  $x \equiv (\rho_0 - \rho_{\text{sat}})/3\rho_{\text{sat}}$  [116–120]

$$\frac{\mathcal{E}(\rho_0)}{\rho_0} \simeq \varepsilon_{\text{sat}} + \frac{1}{2} K_\infty x^2 + \frac{1}{6} Q_\infty x^3 + \dots, \quad (22)$$

$$S(\rho_0) \simeq J + Lx + \frac{1}{2} K_{\text{sym}} x^2 + \frac{1}{6} Q_{\text{sym}} x^3 + \dots \quad (23)$$

The incompressibility  $K_\infty$  exhibit a weak linear dependence on  $a_{\text{surf}}$  that is almost independent on the scheme for c.m. correction, but falls on a different line for each of the three effective masses. The latter finding is a consequence of the correlation between  $m_0^*/m$ ,  $K_\infty$  and the power  $\alpha$  of the density-dependent term in the time-even part of the Skyrme EDF of Eq. (5) that has been identified in Ref. [88] and already mentioned in Sec. III B. The skewness  $Q_\infty$  exhibits a similar weak linear dependence on  $a_{\text{surf}}$  but in the opposite direction. The reason is that for NLO Skyrme EDFs, the equation of state of symmetric matter is entirely determined by just three combinations of coupling constants plus the exponent  $\alpha$  of the density dependence [88], such that for fixed  $\alpha$  and  $\rho_{\text{sat}}$  there are only two further linearly independent properties of INM, implying that, at given  $\varepsilon_{\text{sat}}$  and  $K_\infty$ , the value of  $Q_\infty$  is completely fixed.

The values of  $K_{\text{sym}}$  and  $Q_{\text{sym}}$ , neither of which is directly constrained in the parameter fit, also change over a wide range. This reflects an overall correlation between the density-dependence of the symmetry energy and the surface energy where changes in one of the symmetry energy's characteristics is partially absorbed by changes of the others. For these higher-order coefficients, however, the correlation is no longer near-linear over the entire range of values for  $a_{\text{surf}}$ . The values for  $K_{\text{sym}}$  show a mild dependence on the scheme for c.m. correction only at large  $a_{\text{surf}}$ , and which is quite different from the large offsets found for  $J$  and  $L$  on Fig. 5 over the entire range of  $a_{\text{surf}}$ . The higher-order coefficient  $Q_{\text{sym}}$ , however, exhibits again quite large a dependence on the adopted scheme for c.m. correction. Both  $K_{\text{sym}}$  and  $Q_{\text{sym}}$  additionally exhibit a mild dependence on  $m_0^*/m$ , similarly to  $J$  and  $L$ .

Figure 7 displays the isoscalar effective mass  $m_0^*/m$ , the enhancement factor  $\kappa_v$  of the Thomas-Reiche-Kuhn sum rule, and the splitting  $\Delta m_{np}^* = m_n^*(I)/m - m_p^*(I)/m$  of the effective masses of neutrons and protons in pure neutron matter ( $I = 1$ ). For Skyrme NLO EDFs, these three quantities are not linearly independent, as they only depend on two coupling constants of the time-even part of the Skyrme EDF of Eq. (5)

$$\frac{m}{m_0^*} = 1 + \frac{2m}{\hbar^2} C_0^{\rho\tau} \rho_{\text{sat}} = 1 + \kappa_s, \quad (24)$$

$$\kappa_v = \frac{2m}{\hbar^2} (C_0^{\rho\tau} - C_1^{\rho\tau}) \rho_{\text{sat}}, \quad (25)$$

$$\Delta m_{np}^* = \frac{2(\kappa_v - \kappa_s)}{(1 + \kappa_s)^2 - (\kappa_v - \kappa_s)^2}, \quad (26)$$

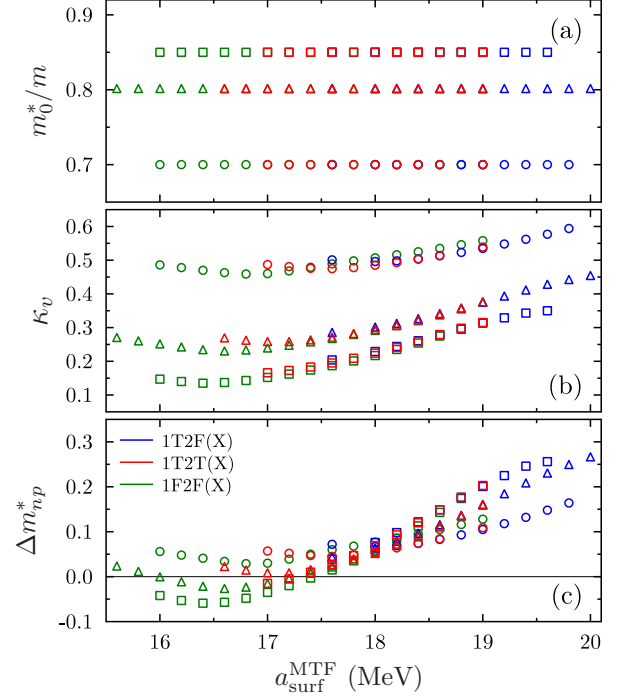


Figure 7. Isoscalar effective mass  $m_0^*/m$ , the enhancement factor of the Thomas-Reiche-Kuhn sum rule  $\kappa_v$ , and the splitting  $\Delta m_{np}^*$  of the effective masses of neutrons and protons in neutron matter. Colors and symbols as on Fig. 4.

see Ref. [43] for a detailed discussion. In particular, the sign of  $\Delta m_{np}^*$  is determined by the sign of  $C_1^{\rho\tau}$ .

As the isoscalar effective mass is imposed exactly on the respective set of fits, the panel displaying  $m_0^*/m$  mainly serves as a reminder of the colors and symbols used to represent the various series of parameter sets.

Contrary to the majority of INM properties discussed so far, for the new parametrizations constructed here the values for  $\kappa_v$  and  $\Delta m_{np}^*$  are strongly correlated to  $m_0^*/m$  and  $a_{\text{surf}}^{\text{MTF}}$ , but remain fairly independent on the scheme of c.m. correction.

At large values of  $a_{\text{surf}}^{\text{MTF}}$ ,  $\Delta m_{np}^*$  takes comparatively large positive values and then becomes smaller with decreasing  $a_{\text{surf}}^{\text{MTF}}$ . For parameter sets with  $m_0^*/m = 0.7$  the value of  $\Delta m_{np}^*$  remains positive at all  $a_{\text{surf}}^{\text{MTF}}$ , whereas for  $m_0^*/m = 0.8$  and  $m_0^*/m = 0.85$  the values of  $\Delta m_{np}^*$  become slightly negative for the smallest values of  $a_{\text{surf}}^{\text{MTF}}$  covered by our fits.

This property has been analyzed in the context of standard Skyrme NLO EDFs before in Ref. [43]. There, it has been pointed out that the early Lyon fits such as SLy4-SLy7 and many others yield negative values for  $\Delta m_{np}^*$ , which is at variance with Brueckner-Hartree-Fock (BHF) predictions for  $\Delta m_{np}^*$  being positive (typically between 0.15 and 0.2 in pure neutron matter calculated with different flavors of BHF approximation [121]). As argued in Ref. [43], this finding is ultimately caused by the stringent constraints on the equation of state of neutron matter



imposed in these fits in combination with a lack of flexibility of the functional form of the EDF. For standard Skyrme EDFs with a small power of the density dependence  $\alpha$  in Eq. (5), the contribution of the effective mass terms to the total binding energy is strongly constrained by the high-density regime of the neutron matter equation of state, even if the latter’s behavior might have a different physical origin. This comes at the expense of losing the possibility to fine-tune the actual isospin dependence of the effective mass, i.e. the spectral properties of the single-particle Hamiltonian in infinite matter. In fact, the attempt to push  $\Delta m_{np}^*$  to positive values may even generate parameter sets with finite-size instabilities in the isovector channel. Adding a second density dependence with sufficiently large exponent is one way to resolve these issues [43].

We employ here the traditional standard Skyrme EDF with a single density dependence that was found to be overconstrained in Ref. [43]. To have the possibility to freely adjust  $a_{\text{surf}}^{\text{MTF}}$ , however, we had to substantially relax the constraints on properties of infinite nuclear and neutron matter. As a byproduct, this yields values for the  $\Delta m_{np}^*$  that are closer to the Brueckner-HF prediction.

The strong correlations between the nuclear matter properties examined above can have two clearly distinct reasons. On the one hand, observables of finite nuclei are known to be only sensitive to specific combinations of two or more properties of INM. On the other hand, the number of INM properties we analyze here is actually larger than the number of parameters of the Skyrme EDF at NLO that determine them. In particular,  $m_0^*/m$ ,  $\kappa_v$  and  $\Delta m_{np}^*$  only depend on parameters of the terms with gradients in the Skyrme generator that also make a large contribution to  $a_{\text{surf}}$  [13] and  $a_{\text{ssym}}$ . The space for these parameters however is limited by the appearance of finite-size instabilities in the four ( $S, T$ ) channels.

These observations indicate that over-constraining some specific properties of nuclear bulk matter in the parameter adjustment of an EDF with a limited number of degrees of freedom can lead to very unrealistic results for other properties. The latter can be higher-order characteristics of homogeneous matter, features of inhomogeneous matter in general, or more specifically surface properties. Indeed, it has been pointed out before that the parametrizations of the standard Skyrme EDF that reproduce best the knowledge about nuclear matter properties of the time [122] do not well describe finite nuclei [123]; surface properties are probably only one aspect of this puzzle. Conversely, extended Skyrme EDFs are needed to describe the global systematics of nuclear masses and the present empirical knowledge about neutron stars within a single model [31, 124, 125]. This observation suggests that constraining nuclear matter properties at densities and asymmetries that are far from those encountered in finite nuclei does not necessarily fix loose ends in the parametrization of a given EDF tailored for the description of finite nuclei as sometimes hoped for, but leads to independent properties that cannot be

simultaneously modeled within the same simple form of the EDF. These concerns can all be traced to the limited number of degrees of freedom of the standard Skyrme EDF. Reconciling some or all of these issues will require extending the form of the EDF, whether through additional density dependencies [43, 126], combined momentum and density dependencies [31, 124, 125, 127, 128], or higher-order momentum dependent terms [38, 39].

#### D. Fits without constraint on $a_{\text{surf}}^{\text{MTF}}$

Since the optimization of the parameters for the EDFs of type 1T2T gives the lowest  $\chi^2$  for a value of  $a_{\text{surf}}^{\text{MTF}}$  that is close to the expected optimal value to describe the properties of nuclei at large deformation, we added one additional parametrization to each series of each type without a constraint on  $a_{\text{surf}}^{\text{MTF}}$ . We call these parametrizations “best fits” in what follows, but underline that they only represent a best fit with respect to the penalty function defined in Sec. III for a given choice of c.m. correction and  $m_0^*/m$ ; these fits are not necessarily optimal to describe nuclear deformation properties. The coupling constants of these parametrizations can be found in the supplementary material [129]. As the surface properties of these additional fits are not constrained by information on deformed nuclei, they can also be used for a study of the impact of the choice for c.m. correction and effective mass on deformation properties of existing parametrizations.

The nuclear matter properties of these parametrizations are listed in Table III. As can be expected from the previous discussion of the correlations between nuclear matter properties and  $a_{\text{surf}}$ , and from the systematic differences between the values of  $a_{\text{surf}}$  at the minimum of the penalty function shown in Fig. 2, the nuclear matter properties of the nine “best fits” vary over a wide range of values, including those constrained in the fit. The values for  $\varepsilon_{\text{sat}}$  fall inside the tolerance interval of the penalty function only for the 1T2F(X), and the values for  $J$  and  $L$  even systematically fall outside the tolerance interval of the penalty function for all of them.

Table III also lists the symmetry energy  $J_{0,1}$  and its slope  $L_{0,1}$  at  $\rho_0 = 0.1 \text{ fm}^{-3}$ . These two quantities at this sub-saturation density are more stringently constrained by the properties of finite nuclei than the values of  $J$  and  $L$  at saturation density, as we mentioned before in the context of Fig. 5. The same is found for the nine “best fits”. In particular, the  $J_{0,1}$  values of the 1F2F(X) and 1T2T(X) fits are near-identical within a few tens of keV, although their values for  $J$  differ by several hundreds of keV. The values of the symmetry energies  $J_{0,1}$  of the three 1T2F(X) fits are also much closer than their  $J$ , but remain slightly larger than those of the 1F2F(X) and 1T2T(X) fits.

As expected from Fig. 7, all 1T2F(X) and 1T2T(X) parameter sets predict a positive splitting of  $\Delta m_{np}^*$ , in agreement with Brueckner-HF calculations. Only the

Table III. Properties of infinite homogeneous nuclear matter (see text for their definition) of the nine best-fit parametrizations. Values for SLy7 and SLy5s1 are shown for comparison.

	$\rho_{\text{sat}}$ (fm <sup>-3</sup> )	$\varepsilon_{\text{sat}}$ (MeV)	$K_{\infty}$ (MeV)	$Q_{\infty}$ (MeV)	$m_0^*/m$	$\kappa_v$	$\Delta m_{np}^*$	$J$ (MeV)	$J_{0.1}$ (MeV)	$L$ (MeV)	$L_{0.1}$ (MeV)	$K_{\text{sym}}$ (MeV)	$Q_{\text{sym}}$ (MeV)
1T2F(0.70)	0.160	-15.948	229.0	-364.1	0.70	0.53	+0.10	30.73	24.92	33.40	38.53	-182.6	517.0
1T2F(0.80)	0.160	-15.917	216.9	-393.0	0.80	0.34	+0.11	30.88	24.90	34.78	39.39	-184.5	496.3
1T2F(0.85)	0.160	-15.900	211.8	-404.7	0.85	0.26	+0.13	30.90	24.87	35.00	39.64	-186.7	487.6
1T2T(0.70)	0.160	-15.860	228.1	-361.9	0.70	0.48	+0.05	30.61	24.83	33.50	38.14	-176.1	525.1
1T2T(0.80)	0.160	-15.832	216.0	-390.7	0.80	0.27	+0.03	30.80	24.83	35.15	38.99	-175.3	508.2
1T2T(0.85)	0.160	-15.820	211.0	-402.6	0.85	0.19	+0.03	30.87	24.82	35.78	39.37	-175.9	499.5
1F2F(0.70)	0.160	-15.742	226.9	-358.7	0.70	0.46	+0.03	30.56	24.82	33.35	37.90	-173.7	531.0
1F2F(0.80)	0.160	-15.713	214.7	-387.6	0.80	0.23	-0.03	30.76	24.84	35.00	38.62	-170.6	520.6
1F2F(0.85)	0.160	-15.701	209.7	-399.5	0.85	0.14	-0.05	30.84	24.85	35.68	38.96	-170.0	514.7
SLy7	0.158	-15.894	229.7	-358.9	0.69	0.25	-0.20	31.99	25.17	47.22	41.95	-113.3	515.2
SLy5s1	0.160	-15.772	222.1	-372.1	0.74	0.30	-0.05	31.43	24.28	48.13	42.76	-124.8	440.4

Table IV. Properties of semi-infinite nuclear matter as obtained with the nine “best-fit” parametrizations (all in units of MeV), where the last two columns list the effective surface energy coefficients  $a_{\text{surf,eff}}^{\text{HF}}(I)$  obtained in HF approximation at the asymmetries of the <sup>180</sup>Hg ( $I = 0.111$ ) and <sup>240</sup>Pu ( $I = 0.217$ ) nuclei discussed in Sec. V. Values for SLy7 and SLy5s1 are shown for comparison.

	$a_{\text{surf}}^{\text{MTF}}$	$a_{\text{surf}}^{\text{ETF}}$	$a_{\text{surf}}^{\text{HF}}$	$a_{\text{ssym}}^{\text{HF}}$	$a_{\text{surf,eff}}^{\text{HF}}$	
					<sup>240</sup> Pu	<sup>180</sup> Hg
1T2F(0.70)	18.9	18.0	18.4	-49	16.1	17.8
1T2F(0.80)	18.6	17.8	18.2	-51	15.8	17.6
1T2F(0.85)	18.4	17.7	18.1	-51	15.7	17.5
1T2T(0.70)	18.0	17.1	17.5	-47	15.3	16.9
1T2T(0.80)	17.7	16.9	17.3	-49	15.0	16.7
1T2T(0.85)	17.6	16.9	17.2	-50	14.9	16.6
1F2F(0.70)	17.1	16.2	16.6	-44	14.5	16.1
1F2F(0.80)	16.8	16.0	16.4	-46	14.3	15.9
1F2F(0.85)	16.7	15.9	16.3	-47	14.1	15.8
SLy7	18.0	17.1	17.5	-51	15.1	16.9
SLy5s1	18.0	17.1	17.6	-56	14.9	16.9

1F2F(X) take negative values as did the earlier SLyX parameter sets [43].

Table III also lists the nuclear matter properties of the SLy7 [17] and SLy5s1 [9] parametrizations that were adjusted with similar, albeit not identical, protocols as ours, and that are both known to provide a reasonable description of fission barriers. There are some noteworthy differences in their nuclear matter properties. The SLy7 parameter set is of 1T2T type and can be directly compared with 1T2T(0.70) that has almost the same effective mass. For SLy7, the values of  $J$  and  $L$  are actually

closer to the target values of our fit protocol than they are for any of our best fits. This, however, comes at the expense of SLy7 exhibiting finite-size spin instabilities, such that it cannot be used in calculations that break time-reversal symmetry without making an ad hoc modification of the  $C_t^{s\Delta s}$  coupling constants in the time-odd part (6) of the Skyrme EDF. This is different for SLy5s1 that has already been adjusted with a constraint on the absence of unphysical finite-size instabilities at densities probed in finite nuclei. The SLy5s1 parameter set is of 1T2F type and has an effective mass that falls in between the values of 1T2F(0.70) and 1T2F(0.80). Again, SLy5s1 yields values for  $J$  and  $L$  that are also closer to the targeted values of our fit protocol. However, its value for  $\varepsilon_{\text{sat}}$  is much further away. These differences result from slight differences in the choices made when setting up the penalty function and indicate that for overall well-adjusted parametrizations of the standard Skyrme EDF any significant improvement with respect to one nuclear matter property can in general only be achieved when significantly degrading others.

Table IV lists surface properties of the nine “best fits” as obtained from calculations of semi-infinite matter. The first three columns provide the surface energy coefficient  $a_{\text{surf}}$  calculated with the HF, ETF and MTF methods, which are also illustrated on Fig. 8. There is again a near-constant shift between the methods with a slight effective-mass dependence, as could be expected from the analysis of the parametrizations with systematically varied  $a_{\text{surf}}^{\text{MTF}}$  as shown on Fig. 1.

As the parameters of the nine “best fits” correspond to the minima of the penalty functions plotted on Fig. 2, the value of their surface energy coefficient depends strongly on their respective scheme for c.m. correction and also their isoscalar effective mass  $m_0^*/m$ . Choosing a different scheme for c.m. correction leads to significantly different values of  $a_{\text{surf}}$ . Confirming the earlier analysis

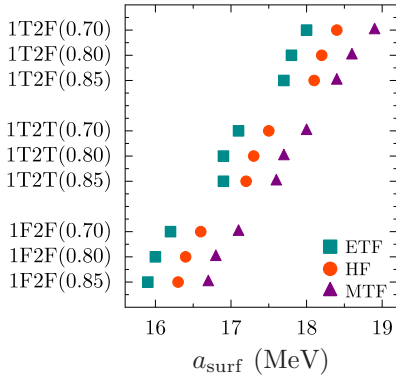


Figure 8. Value of the surface energy coefficient  $a_{\text{surf}}$  calculated with the HF, ETF and MTF methods for the nine “best fits”.

of Ref. [14], those of the 1T2F(X) are typically almost 1 MeV larger than those of the 1T2T(X), whereas those for the 1F2F(X) are about 1 MeV smaller than those for the 1T2T(X), which will make an enormous difference for fission barriers.

To a lesser extent, choosing a different effective mass also yields significantly different values for  $a_{\text{surf}}$  when not constraining the latter. Within a series of fits with same scheme for c.m. correction and compared with the fit with  $m_0^*/m = 0.7$ , the value of  $a_{\text{surf}}$  of the fit with  $m_0^*/m = 0.8$  is about 200 keV smaller, and the one of the fit with  $m_0^*/m = 0.85$  even about 300 keV smaller. As discussed in Refs. [9, 13], changing  $a_{\text{surf}}$  by as little as 0.2 MeV typically changes the outer fission barrier of  $^{240}\text{Pu}$  on the order of 700 keV.

Table IV also lists the surface-symmetry energy coefficient  $a_{\text{ssym}}^{\text{HF}}$  calculated in HF approximation as well as the effective surface symmetry coefficient  $a_{\text{surf,eff}}(I)$  from Eq. (14) of the two nuclei  $^{240}\text{Pu}$  (with  $I = 0.217$ ) and  $^{180}\text{Hg}$  (with  $I = 0.111$ ), whose fission barrier properties will be analyzed in Sec. V.

For the rest of the discussion, we will focus on these parametrizations, labeled 1F2F(X), 1T2F(X), 1T2T(X), and that can be expected to be representative for the typical behavior of standard Skyrme interactions adjusted with a given scheme for c.m. correction at a given effective mass.

### E. The origin of the correlations between nuclear matter properties

As already mentioned, it has been pointed out before [14] that the significantly different values of  $a_{\text{surf}}$  obtained in fits that (i) use different schemes for c.m. correction and that (ii) are only constrained by data on spherical nuclei or nuclear matter, results from the nuclear matter properties absorbing the absent contribution from the c.m. correction energy to the total binding energy of the nuclei entering the penalty function during

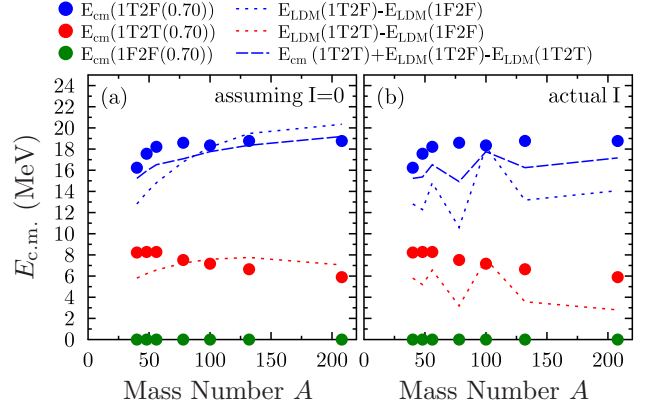


Figure 9. Size of the c.m. correction energy  $E_{\text{c.m.}}$  (full markers) for the three parametrizations with  $m_0^*/m = 0.70$  as indicated for the seven doubly-magic nuclei entering the penalty function of the new fits plotted as a function of their mass number. The lines are estimates for the size of the c.m. correction based on differences of the LDM coefficients obtained for the three fits (see text). Panel (a) compares with the LDM estimates assuming  $I = 0$  for all nuclei, i.e. considering only the volume and surface energy, whereas for the lines in panel (b) also the symmetry and surface symmetry contributions to the LDM energies are taken into account.

the parameters adjustment.

For the seven doubly-magic nuclei entering the adjustment protocol, the size of the c.m. correction energy  $E_{\text{c.m.}}$  is displayed in Fig. 9 for the three parametrizations with  $m_0^*/m = 0.70$  by filled markers. The full c.m. correction of the 1T2T(0.70) parametrizations only takes about one third of the size of the one-body contribution of the 1T2F(0.70). The  $A$ -dependence of the c.m. correction energy is also different in the three cases: for the 1F2F(0.70) it is constant and zero by construction, for the 1T2F(0.70) it quickly rises for light nuclei and then remains almost constant for the heavy ones,<sup>3</sup> whereas for the 1T2T(X) it slowly falls off with mass number (when plotting  $E_{\text{c.m.}}$  for all nuclei across the chart one also clearly sees shell effects introduced by the two-body contribution [14]). Figure 9 clearly indicates that neglecting the two-body contributions to the c.m. correction for reasons of computational convenience neither constitutes a quantitatively nor a qualitatively meaningful approximation. It is because of the different non-linear  $A$  dependence of the resulting c.m. correction energy that differ-

<sup>3</sup> Note that the one-body contribution  $E_{\text{c.m.}}^{(1)}$  to the c.m. correction energy does not fall off to zero in the limit  $A \rightarrow \infty$ ; only the sum of the one-body and two-body contributions does for reasons evoked in the introduction. Instead, when increasing  $A$  beyond the interval shown on Fig. 9, the value of  $E_{\text{c.m.}}^{(1)}$  tends to a value that equals the contribution of the kinetic energy to the energy per particle in infinite matter, which for symmetric matter is  $\frac{3}{5} \frac{\hbar^2}{2m} k_{\text{F}}^2 = \frac{3}{5} \frac{\hbar^2}{2m} \left( \frac{3\pi^2}{2} \rho_{\text{sat}} \right)^{2/3} = 22.108 \text{ MeV}$ .

ent schemes for the c.m. correction have a large impact on the surface energy when fitting parameter sets.

This is illustrated by the three lines on Fig. 9. We recall that we use a convention (10) for  $E_{c.m.}$  where it enters the total binding energy (2) with a minus sign. Assuming that the LDM formula perfectly simulates the contributions from the kinetic, Skyrme and Coulomb energies to the total energy of nuclei when inserting the nuclear matter properties of a given parametrization, one should find  $E_{LDM}^{1F2F} = E_{LDM}^{1T2T} - E_{c.m.}^{1T2T}$  or, equivalently,

$$E_{c.m.}^{1T2T} = E_{LDM}^{1T2T} - E_{LDM}^{1F2F} \quad (27)$$

and similar when comparing two other pairs of parametrizations. The dotted lines on Fig. 9 plot the difference between the LDM energies, calculated through Eq. (13) and using the nuclear matter properties listed in Tables III and IV, of either the 1T2T(0.70) and 1F2F(0.70) (drawn in red) or the 1T2F(0.70) and 1F2F(0.70) (drawn in blue) parametrizations, respectively. In panel (a) only the isoscalar volume and surface terms of the LDM energy are included in this analysis, whereas in panel (b) this is done for the full LDM energy including the symmetry and surface symmetry terms.<sup>4</sup> The dashed blue line shows the sum of the c.m. correction energy  $E_{c.m.}$  obtained with 1T2T(0.70) and the difference between the LDM energies obtained with 1T2F(0.70) and 1T2T(0.70). If the contribution of  $E_{c.m.}$  to the total binding energy was perfectly absorbed by the nuclear matter properties, then the three lines would fall on top of the markers of same color.

For the simpler estimate made in panel (a) this is almost the case; in particular the difference in c.m. correction energy between 1T2T(0.70) and 1T2F(0.70) is very well reproduced by the LDM estimate, as already observed in Ref. [14]. The absolute size of the c.m. correction energies found with 1T2T(0.70) and 1T2F(0.70), however, is less well described by the difference in LDM energies between either and 1F2F(0.70). Also, including the isovector terms in the LDM energy, in particular the surface symmetry energy whose coefficient varies by several MeV, somewhat spoils the agreement between  $E_{c.m.}$  and the LDM estimates, pointing to a more complex compensation between terms in the parameter adjustment as far as the isovector degree of freedom is concerned. This is not too surprising as the LDM expression for the energy assumes that the isovector density is constant throughout the nucleus, and the symmetry energy the same at all densities, which is not at all the case in a self-consistent mean-field model.

Following Ref. [14], the overall size and sign of the differences between the nuclear matter properties of the 1F2F(X), 1T2F(X), and 1T2T(X) can be explained by fitting a simplified LDM expression  $b_{vol} A + b_{surf} A^{2/3}$  directly to the c.m. correction energies plotted on Fig. 9.

For 1T2T(0.70) one finds  $b_{vol} = -0.185$  MeV,  $b_{surf} = 1.241$  MeV. These numbers are of similar size as the differences  $\Delta a_{vol} = -0.118$  MeV and  $\Delta a_{surf} = 0.9$  MeV found between the values of these coefficients for 1T2T(0.70) and 1F2F(0.70) in Tables III and IV. A similar qualitative agreement is found for 1T2F(0.70) and 1F2F(0.70) with  $b_{vol} = -0.325$  MeV,  $b_{surf} = 2.431$  MeV and  $\Delta a_{vol} = -0.206$  MeV,  $\Delta a_{surf} = 1.8$  MeV.

That  $a_{vol}$  and  $a_{surf}$  have to change simultaneously in opposite direction when the interaction energy has to absorb the contribution from the c.m. correction to the binding energy becomes evident when considering the c.m. correction energy to be roughly independent of  $A$  for the nuclei entering the adjustment protocol. A constant change in binding energy of these nuclei can be roughly achieved by a small change of the volume term  $\propto A$  and a larger change of the surface term  $\propto A^{2/3}$  in the opposite direction. For example, assuming that  $E_{c.m.}$  of the 1T2T(0.70) parametrization is simply 7 MeV for nuclei in the range  $40 \leq A \leq 208$ , a least-square fit of the simplified LDM formula to these values yields  $b_{vol} = -0.135$  MeV,  $b_{surf} = 0.99$  MeV, which is even closer to the actual change of the nuclear matter properties when comparing 1F2F(0.70) with 1T2T(0.70) than what is found fitting the precise values for  $E_{c.m.}$  obtained for 1T2T(0.70). Repeating the same estimate with 19 MeV as an approximation for the c.m. correction energy of the 1T2F(0.70) parametrization leads to  $b_{vol} = -0.348$  MeV and  $b_{surf} = 2.53$  MeV.

As said before, taking into account that some of the nuclei are asymmetric leads to a less clear picture. We also recall that  $a_{vol} = \varepsilon_{sat}$  and  $a_{sym} = J$  are constrained in our adjustment protocol, such that their values cannot vary freely when fitting parametrizations with different schemes for c.m. correction. In particular, the above analysis indicates that  $a_{vol} = \varepsilon_{sat}$  has to change by about the size of its tolerance in the adjustment protocol in order to simulate the presence or absence of one or the other contribution to the c.m. correction.

These findings are consistent with the presumption of Ref. [14] that the absent contributions from the c.m. correction to the total binding energy of the nuclei considered in the fit are absorbed by the nuclear matter properties of the resulting parameter sets, and demonstrates that it also applies to the comparison with parameters sets that do not consider any c.m. correction at all.

Results found for the parametrizations with  $m_0^*/m = 0.80$  and  $m_0^*/m = 0.85$  are very similar to what is shown on Fig. 9, with a subtle difference in detail that would, however, be difficult to identify on a plot: for the seven nuclei entering the fit, the c.m. correction energy calculated in either the 1T2T or the 1T2F scheme decreases by roughly 200 keV when going from a fit with  $m_0^*/m = 0.70$  to a fit with  $m_0^*/m = 0.85$ .

We also mention in passing that, for the 1T2T(X) fits, the one-body contribution to the c.m. correction is typically 200 keV larger than the value found with the 1T2F(X) fit with same effective mass because of self-

<sup>4</sup> Note that the Coulomb energy does not contribute to these LDM estimates as, by construction,  $\rho_{sat}$  is the same for all parametrizations considered here.



consistency effects.

Compared with other contributions to the binding energy, a particularity of the c.m. correction energy is that over the range of experimentally accessible nuclei it is almost constant. It turns out that modern refined liquid-drop models also contain large mass-independent terms, i.e. have contributions that are proportional to  $A^0$ . These terms still have an isospin dependence, though. In the finite-range liquid-drop model (FRLDM) of Ref. [130] there is an explicit  $A^0$  term as well as a contribution from the finite-range surface energy that scales as  $A^0$ . In the notation of that paper, for spherical nuclei the sum of these terms is given by  $a_0 - \frac{3a_s^2}{r_0^2} a_s (1 - \kappa_s I^2)$ . Inserting the values of the constants, one finds  $2.645 - 21.927(1 - 2.39 I^2)$  MeV, which varies between  $-19.28$  MeV for  $^{40}\text{Ca}$  and other  $N = Z$  nuclei and  $-16.93$  MeV for  $^{208}\text{Pb}$ . These values are very close to the contribution of the one-body term of the c.m. correction to the total energy as obtained with 1T2F(0.70) and plotted on Fig. 9. The Lublin-Strasbourg liquid drop model (LSD) of Ref. [131] also has a sizable contribution  $\propto A^0$ , which there is motivated as a Gaussian curvature term. In the notation of the paper, it takes the form  $b_{\text{curG}}(1 - \kappa_{\text{curG}} I^2) A^0$ . Inserting again the values of the constants for the NLD parametrization of the LSD, one finds  $10.357(1 - 13.4235 I^2)$ , which takes a positive value of  $10.357$  MeV for all  $N = Z$  nuclei, and falls off to  $4.14$  MeV for heavy nuclei on the valley of stability like  $^{208}\text{Pb}$ , and even might become slightly negative for very neutron-rich ones, such as  $-0.703$  MeV for  $^{78}\text{Ni}$ . The  $A^0$  terms of these modern liquid-drop models therefore behave very differently. Although such term-by-term comparisons between different approaches have to remain qualitative, it seems that the successful reproduction of nuclear masses requires the presence of rather large contributions to the binding energy that are essentially mass-independent.

## V. DEFORMATION PROPERTIES

### A. Set-up of the calculations

To explore the deformation properties of the newly constructed parametrizations, we turned to the MOCCA code of Ref. [132], which represents single-particle wave functions on a three-dimensional Cartesian coordinate-space mesh with equidistant points. Profiting from the efficiency of Lagrange meshes [133], the relatively coarse discretisation  $dx = 1.0$  fm chosen for this study is sufficiently accurate to resolve absolute binding energies to within a few hundred keV [134]. This is sufficient for our purposes, especially since this numerical precision is essentially independent of the nuclear shape, even for the very elongated shapes we discuss below [134], such that we expect differences of binding energies to be even more accurately resolved.

The deformation of the nuclear density can be characterized by its multipole moments  $Q_{\ell m}$ . For two integers  $\ell$  and  $m$  that satisfy  $\ell \geq m \geq 0$ , we define

$$Q_{\ell m} = \int d^3r \rho_0(\mathbf{r}) r^\ell \text{Re} [Y_{\ell m}(\theta, \phi)] , \quad (28)$$

where  $\rho_0(\mathbf{r})$  is the matter density and  $Y_{\ell m}(\theta, \phi)$  is a spherical harmonic. Since the  $Q_{\ell m}$  scale with particle number, it is more straightforward to compare dimensionless multipole moments  $\beta_{\ell m}$ :

$$\beta_{\ell m} = \frac{4\pi}{3R^\ell A} Q_{\ell m} , \quad (29)$$

where  $R = 1.2 A^{1/3}$  fm. By replacing  $\rho_0(\mathbf{r})$  in Eq. (28) by the neutron or proton density and replacing  $A$  in Eq. (29) by either  $N$  or  $Z$ , we also define the neutron and proton multipole moments  $\beta_{q, \ell m}$  with  $q = p, n$ . We will in what follows assume that the nuclear charge density equals the proton density, which implies that the charge and proton multipole moments are equal.

The flexibility of the MOCCA code with respect to the symmetries imposed on the eigenstates of the single-particle Hamiltonian is used to reduce the computational effort. All calculations reported here conserve time-reversal symmetry,  $z$  signature  $\hat{R}_z$  and the  $y$  time-simplex  $\hat{S}_y^T$ . The combination of the latter two imposes two plane symmetries in the  $x = 0$  and  $y = 0$  planes on the local densities and currents [135]. For the calculation of fission barriers at large deformation, parity  $\hat{P}$  is not enforced, which allows for the description of shapes that are not reflection symmetric with respect to the  $z = 0$  plane. In this case, a constraint on the mass dipole moment  $\beta_{10}$  is added to fix the nucleus' center-of-mass at the origin of the numerical box. For the study of shapes at small deformation, however, it turned out that for the majority of cases parity can be enforced as a conserved symmetry without loss of generality. This reduces the computational cost and facilitates the convergence of the self-consistent equations. For either of these two choices, the Cartesian 3d representation allows for the description of non-axial shapes. It turned out, however, that most of the states discussed below remain axially symmetric.

### B. Treatment of pairing correlations

The 1F2F(X), 1T2F(X), and 1T2T(X) parametrizations were adjusted to properties of doubly-magic nuclei for which pairing correlations vanish at the mean-field level. The calculations of energy surfaces and deformed open-shell nuclei that will be presented in what follows, however, require the introduction of pairing correlations. These are treated by solving the HFB equations within the two-basis method [136, 137]. For the effective pairing EDF, we employ the widely-used density-dependent

form [138]

$$E_{\text{pair}} = \sum_{q=p,n} \frac{V_q}{4} \int d^3r \left[ 1 - \frac{\rho_0(\mathbf{r})}{\rho_c} \right] \tilde{\rho}_q^*(\mathbf{r}) \tilde{\rho}_q(\mathbf{r}), \quad (30)$$

where  $\tilde{\rho}_q(\mathbf{r})$  is the pair density [1]. With  $\rho_c = 0.16 \text{ fm}^{-3}$ , this form corresponds to a “surface-type” pairing interaction. A smooth cutoff above and below the Fermi energy as described in Refs. [9, 13, 137] limits the pairing correlations to the single-particle levels around the Fermi energy. For simplicity, we take the proton and neutron pairing strengths to be equal, i.e.  $V_n = V_p = V_1$ , and use the same cutoff parameters ( $\mu_p = \mu_n = 0.5 \text{ MeV}$  and  $\Delta E_p = \Delta E_n = 5.0 \text{ MeV}$ ) for both species, as done before in Refs. [9, 13, 137, 138].

While our earlier studies on deformation energies reported in Refs. [9, 13] used the HFB+Lipkin-Nogami (LN) scheme to ensure the presence of pairing correlations in all states, we use here the stabilisation of the pairing EDF proposed in Ref. [139] instead, with  $E_{\text{cutb}} = 0.3 \text{ MeV}$  for the cutoff parameter.

It is well-known that the pairing strength has to scale with effective mass  $m_0^*/m$ . For the series with  $m_0^*/m = 0.70$  we use the same pairing strength of  $V_1 = -1250 \text{ MeV fm}^{-3}$  for protons and neutrons originally adjusted for SLy4 in Ref. [138] and used in Refs. [9, 13]. Although originally adjusted within the HFB+LN scheme, this pairing strength gives nearly identical values of pairing gaps when used in the context of the stabilized pairing EDF. For the two other series, the pairing strength was readjusted to give the same average neutron pairing gap for the spherical ground state of  $^{188}\text{Pb}$  as SLy4 with  $V_1 = -1250 \text{ MeV fm}^{-3}$ , which led to the values of  $V_1 = -1175 \text{ MeV fm}^{-3}$  for the parametrizations with  $m_0^*/m = 0.80$  and  $V_1 = -1140 \text{ MeV fm}^{-3}$  for those with  $m_0^*/m = 0.85$ .

In some figures, we compare results obtained with the new fits with results obtained with the existing SLy7 [17] and SLy5s1 [9] parametrizations that are known to have reasonable deformation properties. Both have an isoscalar effective mass close to 0.7, see Table III, and will be used with a pairing strength of  $V_q = -1250 \text{ MeV fm}^{-3}$ .

### C. Fission barrier of $^{240}\text{Pu}$

We start our discussion of deformation properties by considering the double-humped fission barrier of  $^{240}\text{Pu}$ , which is arguably the most widely-used testing ground for the modeling of nuclear fission [1, 9, 10, 99, 100, 140–147]. Figure 10 displays the static fission barrier of this nucleus calculated as in Ref. [13]. For all eleven parametrizations, we find a very similar fission path in the space of multipole deformations  $\beta_{\ell m}$  that evolve continuously without sudden jumps. There is one little difference in detail for 1F2F(0.70), 1F2F(0.80), 1F2F(0.85), 1T2T(0.70) and SLy7. For these we find a narrow region around the ground state where octupole deforma-

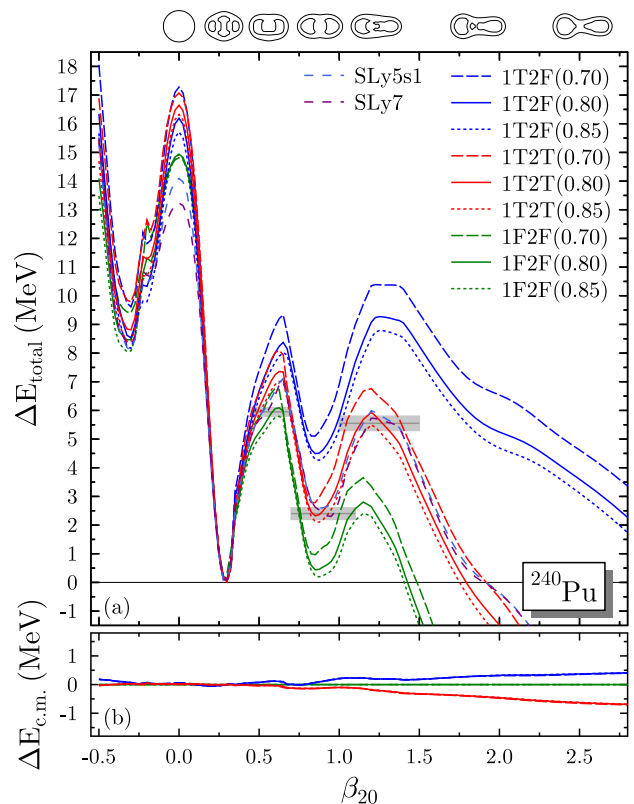


Figure 10. Deformation energy curve of  $^{240}\text{Pu}$  (panel (a)) and change of the center-of-mass correction (panel (b)) as a function of the quadrupole deformation  $\beta_{20}$  for the parametrizations as indicated. In both cases, the energies are normalized to the value at the respective ground-state deformation. To facilitate the comparison, both panels share the same energy scale. The horizontal grey bars in panel (a) indicate experimental values for the height of the inner and outer barriers as well as the excitation energy of the fission isomer, taken from the sources mentioned in the text. The inserts on top of the figure indicate the evolution of shapes along the fission path, the upper and lower halves representing isodensities at  $\rho_0 = 0.08$  and  $0.15 \text{ fm}^{-3}$  in the  $x$  and  $y$  directions.

tion leads to a small additional energy gain: 200 keV for 1F2F(0.70) and a few tens of keV for the four others. For all other parametrizations, all configurations are reflection symmetric up to the superdeformed minimum associated with the fission isomer. At larger quadrupole deformations, octupole deformation gradually sets in and shapes become reflection-asymmetric. Around the two saddle points, the lowest-energy path passes through non-axial shapes that lower the inner barrier by about 1.5 MeV and the outer one by about 0.5 MeV as found earlier in Refs. [13, 29]. The corresponding  $\beta_{22}$  deformation takes values of about 0.07 for the inner and 0.02 for the outer barrier, which corresponds to  $\gamma$  angles of about 12 degrees and 1.5 degrees, respectively. At small deformations and around the minima, the nucleus takes an axial shape. Altogether, the fission path is very similar to the one of the actinide nuclei discussed in Ref. [29].

The energy curves obtained with the new parameter sets fall into three clearly distinguishable groups that are identified by the scheme for c.m. correction employed during their adjustment: those using the 1T2F recipe give systematically the highest energy curves relative to the ground state when increasing deformation, those using the 1F2F recipe the lowest ones, while the 1T2T sets fall in between. The systematic differences are enormous: compared with the 1T2T(X) parameter sets, the excitation energy of the fission isomer is about 2 MeV larger for those in the 1T2F(X) set, while for the 1F2F(X) sets it is about 2 MeV smaller. For the height of the outer barrier, the differences are even larger. Within each of these three groups, there also is a clear dependence of the deformation energy on isoscalar effective mass: for a given recipe of c.m. correction, the deformation energy systematically increases with decreasing  $m_0^*/m$ , and this in a very similar way for each of the three recipes.

As can be seen from panel (b) of Fig. 10, the variation of the c.m. correction energy  $E_{\text{c.m.}}$  with deformation is much smaller than the difference between the barriers and therefore cannot explain it. Still, the one-body contribution systematically increases the barriers by a few 100 keV, whereas the full c.m. correction reduces the barriers by a few 100 keV. The value of the effective mass has practically no influence on the variation of  $E_{\text{c.m.}}$ .

The differences between the barriers reflect primarily the difference between the values for  $a_{\text{surf}}$  of these parametrizations. As has been pointed out earlier in Ref. [14], for parameter sets that are adjusted like ours without an explicit constraint on deformation properties,  $a_{\text{surf}}$  can take very different values depending on the scheme for c.m. correction chosen during the parameter adjustment. In addition, the present study indicates that such fit protocols also produce a weak dependence of  $a_{\text{surf}}$  on the value chosen for the isoscalar effective mass, cf. Table III.

The barriers obtained with SLy5s1 and SLy7 are very similar to those of the new 1T2T(X) parameter sets, as expected from their similar values for  $a_{\text{surf}}$ . There are small differences in detail: SLy7 yields a smaller excitation energy of the fission isomer, whereas SLy5s1 predicts it at slightly larger deformation, and both SLy7 and SLy5s1 produce a slightly wider outer barrier.

The ground-state deformation takes practically the same value of  $\beta_{20} \simeq 0.3$  for all parameter sets and agrees well with the available experimental data [148, 149], see the more detailed comparison in Sec. VE1. The deformation of the isomer, however, is slightly different for each parameter set, mainly in dependence of the effective mass, but always remains close to  $\beta_{20} \simeq 0.85$ . This will also be analysed in more detail in Sec. VE1. Depending on the height of the fission barrier, the positions of the inner and outer saddle points also move to slightly larger deformations with increasing barrier height, as observed before for the SLy5sX series [13].

Before entering the comparison with data, we recall that the main purpose of our new fits discussed here is not the “best reproduction” of barriers by itself, which

in one way or another should include actual information about deformation in the adjustment protocol, but the question of how well barriers are reproduced *without* considering them in the adjustment protocol depending on the choices made for the c.m. correction and the isoscalar effective mass. Phrased differently, we want to analyze which global choices make the reproduction of fission barriers a fine-tuning problem within an existing adjustment protocol that will not be in disproportionate conflict with other constraints.

Concerning the available experimental data for the barrier, we recall that some experiments for double-humped fission barriers provide information about the inner and outer barrier heights, while others issue information about the higher (“primary”) and lower (“secondary”) of the two barriers.

An example for the analysis of fission of  $^{240}\text{Pu}$  induced by direct reactions is Ref. [150], which yields  $5.80 \pm 0.20$  MeV and  $5.45 \pm 0.20$  MeV for the heights of the inner and outer barrier, respectively. The data evaluation from multiple experiments provided by the RIPL-3 database [151], however, lists 6.05 and 5.1 MeV for the heights of these barriers. A recent multi-nucleon transfer experiment finds  $6.25 \pm 0.32$  MeV for the primary fission barrier [152]. Values for the excitation energy of the  $0^+$  superdeformed fission isomer also differ; the authors of Ref. [153] give  $(2.25 \pm 0.20)$  MeV, while the data evaluation of Ref. [154] lists a value of 2.8 MeV. The error bars of the experimental values displayed on Fig. 10 cover the range of these values.

From Fig. 10 it is clear that the 1T2T(X) fits that consider the full c.m. correction give a height of the outer barrier and an excitation energy of the isomer that are closest to experiment, although neither describes the data perfectly. The parameter sets with an elevated effective mass of 0.8 and 0.85 perform slightly better than the one with  $m_0^*/m = 0.7$ , but that seems to be a particularity of the fit protocol used for the new parameter sets as the calculated barrier obtained with the SLy7 parametrization that has an effective mass of  $m_0^*/m = 0.69$  is about as close to the data.

By contrast, the inner barrier is systematically overestimated by all of the 1T2T(X) fits. Its height is only reasonably well described by the three 1F2F(X) fits that in turn grossly underestimate the excitation energy of the isomer and the height of the outer barrier.

Still, Fig. 10 confirms the earlier finding that when adjusting the parameters of EDFs solely to data on spherical ground nuclei and infinite matter, choosing the full c.m. correction yields more realistic surface properties than choosing the 1F2F or 1T2F recipes instead.

Obtaining realistic surface properties for parameter sets of 1F2F and 1T2F type requires adding information on the surface energy to the fit protocol. This is exemplified on Fig. 10 by SLy5s1 that produces a barrier of similar quality as the one from the 1T2T(0.80) and 1T2T(0.85) and SLy7 parametrizations. Unlike these, SLy5s1 is of 1T2F type and had to be constrained dur-

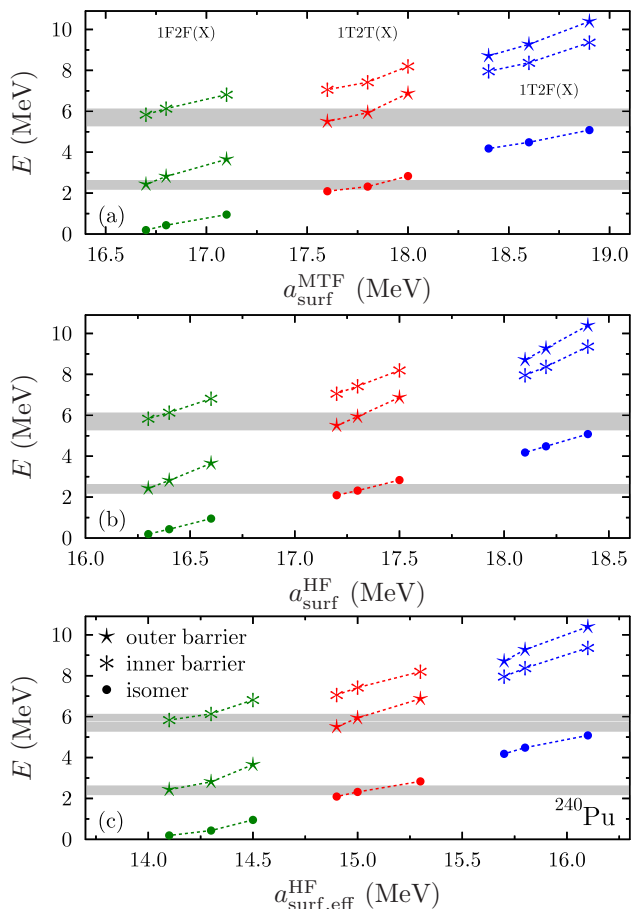


Figure 11. Characteristic energies of the fission barrier of  $^{240}\text{Pu}$  as a function of  $a_{\text{surf}}^{\text{MTF}}$  (panel (a)),  $a_{\text{surf}}^{\text{HF}}$  (panel (b)), and  $a_{\text{surf,eff}}^{\text{HF}}(^{240}\text{Pu})$  (panel (c)). Colors indicate families of parameter sets with same scheme for c.m. correction as in Fig. 10. Markers, however, indicate here the excitation energy of the fission isomer and the heights of the inner and outer barrier, respectively. To guide the eye, lines connect results obtained with the three parameter sets with same scheme for c.m. correction, but different effective mass. Within each family of parameter sets,  $a_{\text{surf}}$  decreases with increasing effective mass, see Tab. IV. As on Fig. 10, the experimental data are indicated by horizontal grey bars, where those for the inner and outer barrier overlap.

ing the fit to have a realistic value of the surface energy by shifting its  $a_{\text{surf}}^{\text{MTF}}$  value from about 19.0 MeV that it would naturally acquire to 18 MeV. Similarly, the parametrizations SkM\* [10] (that is of 1T2F type), UNEDF1 [12], and UNEDF2 [19] (both of 1F2F type) that perform similarly well for this barrier were also constrained in one way or the other to do so.<sup>5</sup>

The failure of the three 1T2T fits, and also SLy5s1 and SLy7, to describe simultaneously all of the three characteristic energies of the barrier of  $^{240}\text{Pu}$  is consistent with the earlier findings for nuclei in this mass region [1, 9]. Two recent exceptions are BSkG1 and BSkG2 [29], which describe the inner and outer barriers of  $^{240}\text{Pu}$  similarly well.

As recalled in Sec. IV B, the surface energy of an EDF cannot be represented by a unique number, as it has an isospin dependence and can be determined within different schemes. This poses the question to which of the various possibilities to characterize surface energy the barriers are actually most correlated to. To answer this question, Fig. 11 displays the excitation energy of the fission isomer and the heights of the inner and outer barrier of  $^{240}\text{Pu}$  as a function of the isoscalar surface energy coefficients calculated in MTF ( $a_{\text{surf}}^{\text{MTF}}$ ) and HF ( $a_{\text{surf}}^{\text{HF}}$ ) approximation, as well as the effective isospin-dependent surface energy coefficient  $a_{\text{surf,eff}}^{\text{HF}}$  calculated in HF approximation.

The different range of  $a_{\text{surf}}$  values over which the three parameter sets with same c.m. correction scheme are spread in each of the panels of Fig. 11 illustrates again that the difference between  $a_{\text{surf}}^{\text{MTF}}$  and  $a_{\text{surf}}^{\text{HF}}$  slightly depends on effective mass as a consequence of the approximations made in the MTF scheme, and that also the surface symmetry energy coefficient that enters  $a_{\text{surf,eff}}^{\text{HF}}$  takes a slightly different value at each effective mass. This change in spread has the consequence that the slope of the line connecting results obtained with the three parameter sets with same c.m. correction is different in each of the three panels.

When comparing results obtained with parameter sets with different effective mass for a given choice of c.m. correction, i.e. the data that are plotted in same color on Fig. 11, one finds in most cases a nearly linear correlation between the calculated characteristic energies of the barrier and the respective surface energy coefficient. For none of the three choices of surface energy coefficient, however, the calculated characteristic energies on Fig. 11 fall near a unique straight line when comparing all nine parametrizations from the different families of fits, i.e. the data plotted in different color. Instead, there always is an offset when going from one family of parametrizations to the next. The sign of this offset is also not universal. For the excitation energy of the isomer, extrapolating the results from a family with overall low  $a_{\text{surf}}$  to higher  $a_{\text{surf}}$  will underestimate the results obtained from parameter sets that actually have larger  $a_{\text{surf}}$ . For the height of the inner barrier the opposite happens: extrapolating values obtained with parameter sets that use the same c.m. correction to higher  $a_{\text{surf}}$  will overestimate the barrier height actually found for the other families of fits.

<sup>5</sup> Although SkM\* [10] is also of 1T2F type, its surface energy actually had to be *increased* compared with the original SkM [30] parametrization, see also Ref. [9] for a detailed comparison of their  $a_{\text{surf}}$  values and the corresponding fission barrier of  $^{240}\text{Pu}$

calculated in a similar manner as done here. The reason is that SkM was adjusted within an unusual protocol that focused on nuclear matter properties relevant for the description of giant resonances.



For the outer barrier height, the sign of the offset is even different when plotting the values as a function of  $a_{\text{surf}}^{\text{HF}}$  or as a function of either  $a_{\text{surf}}^{\text{MTF}}$  or  $a_{\text{surf,eff}}^{\text{HF}}$ . The offsets remain comparatively small and do not prevent using any of these correlations to adjust a suitable value of  $a_{\text{surf}}$  as an alternative to the adjustment of actual fission barriers. However, as already suspected in Ref. [9] based on a set of parametrizations that was much more limited with respect to the choices for c.m. correction and effective mass, one can expect a nearly linear correlation between  $a_{\text{surf}}$  and deformation energies only when the fundamental choices made for the form of the EDF and the fit protocol are the same. This is of course not surprising as the very origin of the complicated topography of a fission barrier like the one of Fig. 10 is generated by the variation of shell effects that are not directly influenced by  $a_{\text{surf}}$ , but depend sensitively on many of the other choices made when parametrizing an EDF.

Shell effects are not the only possible source of such differences. There are also other contributions to the deformation energy that are not represented by the surface energy coefficient and therefore can spoil the correlation between these quantities. One of these is the deformation dependence of the pairing correlation energy, i.e. the energy difference between a HF and a HFB calculation of a nucleus at given deformation. This energy changes along the fission path as a nucleus' ground state and fission isomer correspond to deformations where pairing correlations are weak because of the low level density around the Fermi surface, whereas the saddle points correspond to regions where pairing correlations are strong because of a large level density around the Fermi surface. Assuming that for a given nucleus the size of the pairing correlation energy scales with pairing strength, the need to adjust the pairing strength separately for parametrizations with different effective mass can generate a systematic difference between parameter sets with different  $m_0^*/m$ . This would introduce an effective mass-dependence of the characteristic energies from parametrizations with different effective mass within a series with given scheme for c.m. correction, and thereby misalign the trends when comparing series with different scheme for c.m. correction. While such misalignments are seen on Fig. 11, it is unlikely that the pairing correlation energy is their main source: for the reasons already mentioned, its effect on the excitation energy of the fission isomer should be smaller than its effect on the barrier heights, which is not the case for the differences seen on the figure.

Another contribution for the offsets visible on Fig. 11 is the deformation dependence of the c.m. correction energy  $E_{\text{c.m.}}$  displayed in the lower panel of Fig. 10. Indeed,  $E_{\text{c.m.}}$  does not contribute to the calculation of the surface energy of infinite matter, such that its mass- and deformation dependence is not represented by  $a_{\text{surf}}$  and  $a_{\text{ssym}}$ . Comparing with the 1F2F case where the c.m. correction energy is zero by construction, the values for the excitation energy of the fission isomer are pushed up by about 200 keV by this effect for parameter sets of 1T2F type,

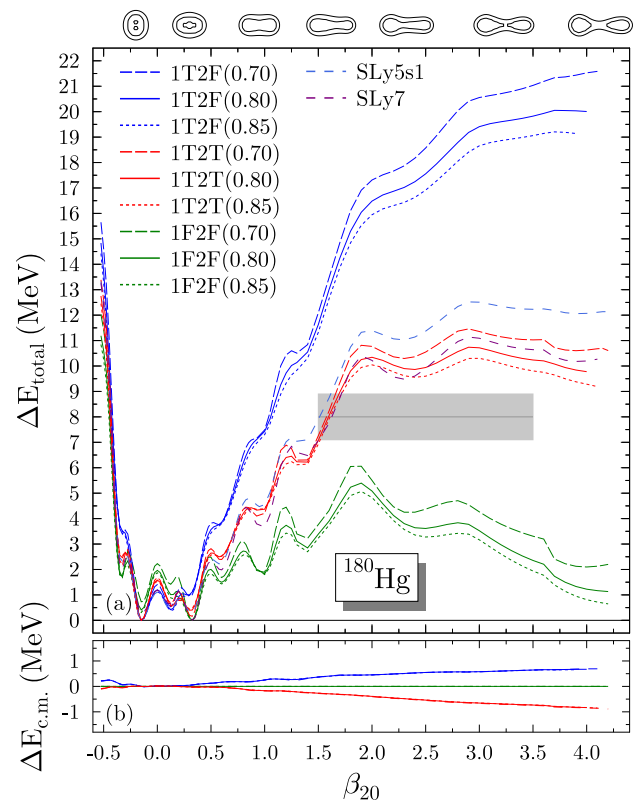


Figure 12. Deformation energy curve of  $^{180}\text{Hg}$  (panel (a)) and change of the center-of-mass correction (panel (b)) as a function of the quadrupole deformation  $\beta_{20}$  drawn in the same way as on Fig. 10. The energy curves end at the deformation at which the calculation jumps to a solution with two separate fragments.

whereas they are pulled down a few tens of keV for parameter sets of 1T2T type. Again, this effect cannot be the major source for the observed offsets in Fig. 11, as it is too small in absolute size and also cannot explain the relative sign in all cases.

#### D. Energy landscape of $^{180}\text{Hg}$

As a second example we discuss  $^{180}\text{Hg}$ , which is among the most neutron-deficient nuclei for which information about the fission barrier is available. Because of its much smaller asymmetry  $I$ , the surface symmetry energy is much less important for the barrier of  $^{180}\text{Hg}$  than for the one of  $^{240}\text{Pu}$ .

In addition, this nucleus is situated in a different region of the chart of nuclei where shell effects along the fission path are very different from those determining the fission path of  $^{240}\text{Pu}$ . This has several consequences for the energy curves displayed on Fig. 12. First,  $^{180}\text{Hg}$  exhibits shape coexistence of near-degenerate normal-deformed states at low excitation energy, one at an oblate deformation of  $\beta_{20} \simeq -0.15$ , the other at a prolate deformation of

$\beta_{20} \simeq 0.32$ . Second, model calculations [155–158] suggest that there is only one broad barrier, whose saddle point is at very larger deformation, possibly very close to the scission point. In fact, the curves on Fig. 12 end where the calculations jump to a solution with two non-identical fragments. The broad outer barrier follows a reflection-asymmetric path beginning at around  $\beta_{20} \simeq 1.1$ . Like in our earlier study of this nucleus with the SLy5sX parametrizations reported in Ref. [13], we have not found non-axial solutions that lower the barrier around the saddle point.

As we are mainly interested in the primary fission barrier of this nucleus, we have not checked if the various super- and hyperdeformed local minima that can be found at intermediate deformations might be connected through triaxial shapes that bypass the small barriers between them that get particularly pronounced for the parameter sets with small surface energy coefficient. For this reason, the energy curves shown on Fig. 12 are for an entirely axial fission path.

For the barrier height, comparison with experiment is not entirely straightforward as all available data were obtained from the observation of  $\beta$ -delayed fission of  $^{180}\text{Tl}$  [159], which passes through excited states of  $^{180}\text{Hg}$  with negative parity and finite angular momentum. The excitation energy of these states is necessarily smaller than the  $Q$  value for electron capture of  $^{180}\text{Tl}$ ,  $Q_{\text{EC}}(^{180}\text{Tl}) = 10.44$  MeV, which sets an upper bound for the fission barrier. The model-dependent analysis of the measured probability of  $\beta$ -delayed fission in that nucleus [156] suggests that the fission barrier has a height of about 8.0(9) MeV, which is the value used in Fig. 12.

The configuration of  $^{180}\text{Hg}$  for which fission has been observed can therefore be expected to have a different structure than the ground state for which the fission barrier is calculated. When comparing theory and experiment, however, we assume that these two barriers are the same, as done in the earlier literature on the subject.

The energy curves calculated with the new parametrizations shown on Fig. 12 fall again into three groups according to their scheme for c.m. correction. Compared to  $^{240}\text{Pu}$ , the differences are even more dramatic because of the larger range of deformations that are probed. This makes it even clearer that the differences in barrier height cannot be caused by the variation of the c.m. correction itself with deformation. Within each group of parametrizations with same c.m. scheme, the barrier height decreases again with increasing effective mass, such that the pattern of the energy curves clearly follows the sequence of the parametrizations'  $a_{\text{surf}}$  values.

Comparing the calculated energy curves with data, the 1T2F(X) parametrizations again overestimate the barrier height, whereas the 1F2F(X) underestimate it. While the 1T2T(X) are again closest to experiment, the calculated barriers are of the same size as the upper limit for the barrier from the  $Q_{\text{EC}}$  value, but overestimate the barrier height as deduced in Ref. [156].

Like in the case of  $^{240}\text{Pu}$ , SLy7 gives a barrier height

that falls in between those predicted by the 1T2T(X) parametrizations. By contrast, SLy5s1 gives a visibly higher barrier than the 1T2T(X) although it has a very similar  $a_{\text{surf,eff}}$  value. This different behavior of SLy5s1 can be explained by its different scheme for c.m. correction, which for SLy5s1 is of 1T2F type. As can be seen from panel (b) of Fig. 12, at the respective saddle point at  $\beta_{20} \simeq 2.8$ , the c.m. correction energy of the 1T2F-type parametrizations is about 500 keV larger than for the ground state, whereas the full c.m. correction energy of the 1T2T-type parametrizations becomes 500 keV smaller. Consequently, the difference in c.m. correction increases the barrier height of SLy5s1 by about 1 MeV compared to SLy7 and the 1T2F(X). As the difference in c.m. correction grows further beyond the saddle point, the outmost part of the fission barrier obtained with SLy5s1 is then also somewhat flatter than the one found with any of the 1T2T(X).

As the c.m. correction does not enter the calculation of the surface energy of semi-infinite matter, the slightly different deformation dependence of the c.m. correction energy obtained for the 1F2F(X), 1T2F(X) and 1T2T(X) parametrizations is not accounted for by their  $a_{\text{surf}}$  value. For nuclei with a very wide fission barrier like  $^{180}\text{Hg}$ , the deformation dependence of the c.m. correction can therefore make a visible difference for the fission barriers of parametrizations with same  $a_{\text{surf}}$ , but different scheme for c.m. correction. For  $^{240}\text{Pu}$  with its much narrower fission barrier, the variation of the c.m. correction energy with deformation across the barrier is much smaller, such that it does not have a visible effect on the fission barrier as seen on Fig. 10.

Experimental data consistently points to an oblate shape of the ground state of this and other *even-even* Hg isotopes in this mass region [160], while many EDF parametrizations predict a prolate shape for these nuclei instead. Among those that do correctly predict an oblate ground state for these nuclei are the fits with low  $a_{\text{surf}}$  out of the SLy5sX series such as SLy5s1 [160]. This success, however, cannot be attributed to a low  $a_{\text{surf}}$  value as such. Comparing the new fits, all of the 1T2T(X) parametrizations (intermediate  $a_{\text{surf}}$ ) and all of the 1T2F(X) (large  $a_{\text{surf}}$ ) predict an oblate ground state, whereas the 1F2F(X) (low  $a_{\text{surf}}$ ) predict a prolate ground state. On the other hand, SLy7 predicts a prolate ground state of  $^{180}\text{Hg}$  although its value for  $a_{\text{surf}}$  is similar to those of the 1T2T(X).

For all of these parameter sets, the energy difference between the prolate and oblate minima is at most 1 MeV, and often significantly less. Note that our calculations also predict a third minimum at small prolate deformation, that for the 1T2F(X) parametrizations is actually lower in energy than the prolate minimum at larger deformation. For the parametrizations with large  $a_{\text{surf}}$  values out of the SLy5sX series, the weakly deformed prolate minimum is actually predicted to be the ground state [13, 160].

These minima are generated by shell effects that are

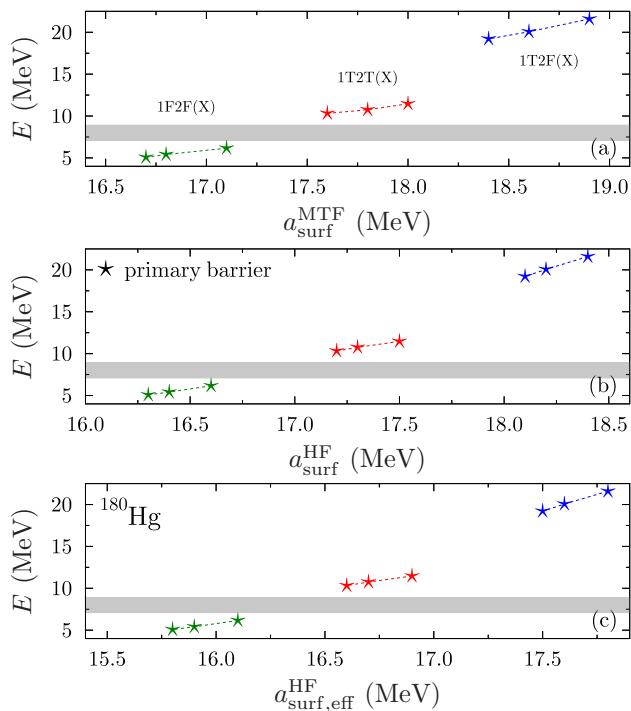


Figure 13. Height of the primary fission barrier of  $^{180}\text{Hg}$  as a function of  $a_{\text{surf}}^{\text{MTF}}$  (panel (a)),  $a_{\text{surf}}^{\text{HF}}$  (panel (b)), and  $a_{\text{surf,eff}}^{\text{HF}}(^{180}\text{Hg})$  (panel (c)) plotted in the same way as on Fig. 11.

related to the evolution of the bunching of single-particle levels with deformation in the Nilsson diagram, and which are more difficult to control in a parameter fit than the surface energy. Assuming that these shell effects are equal for all of the new fits, then the order of the minima obtained with the 1F2F(X), 1T2F(X), and 1T2T(X) parametrizations is actually what one would naively expect from the differences between their surface energy coefficients. At small deformation, the macroscopic deformation energy grows quadratically with quadrupole deformation, see Ref. [13] and references therein, such that a state with larger absolute value of  $\beta_{20}$  loses more macroscopic energy when increasing  $a_{\text{surf}}$  than a state with smaller  $\beta_{20}$ . That the SLy5sX parametrizations discussed in Ref. [160] do not follow this trend indicates that also the ground-state shell effects change significantly within this series, which has been illustrated for  $^{180}\text{Hg}$  in Ref. [13]. Many traditional Skyrme parametrizations predict a well-deformed prolate ground state for even-even Hg isotopes in this mass region, and this even in spite of their having large  $a_{\text{surf}}$  values that are comparable to those of the 1T2F(X). This altogether points to an unresolved fine-tuning problem of shell effects and indicates that finding the expected  $a_{\text{surf}}$ -dependence of the energy difference between the coexisting shapes in  $^{180}\text{Hg}$  for our new fits might be fortuitous.

We note that Fig. 12 indicates that the relative energy between the various normal-deformed minima of  $^{180}\text{Hg}$

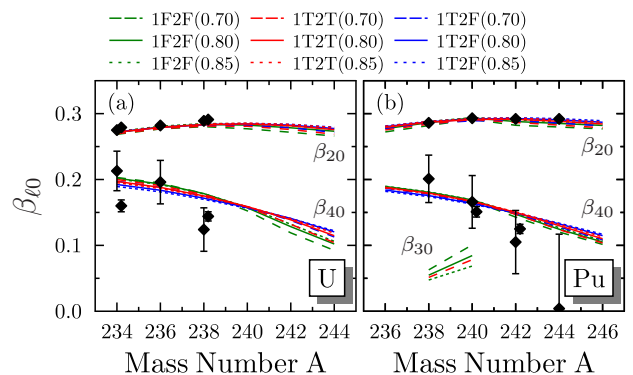


Figure 14. Dimensionless quadrupole and hexadecapole deformation of the charge density distribution of the ground states of even-even U ( $Z = 92$ ) and Pu ( $Z = 94$ ) isotopes compared with experimental data where available, plotted in the same colors and line styles as on Fig. 10. The error bars of the experimental  $\beta_{20}$  values are smaller than the markers used to plot them. For the two Pu isotopes for which we found reflection-asymmetric ground-state shapes, we also show the calculated octupole deformation.

does not show any significant dependence on  $m_0^*/m$  for the best fits. This is slightly surprising, as the size and variation of shell effects could have been affected by the effective mass.

Figure 13 plots the height of the primary fission barrier of  $^{180}\text{Hg}$  as a function of  $a_{\text{surf}}^{\text{MTF}}$ ,  $a_{\text{surf}}^{\text{HF}}$ , and  $a_{\text{surf,eff}}^{\text{HF}}(^{180}\text{Hg})$ . Like in the case of  $^{240}\text{Pu}$  displayed on Fig. 11, there is a near-linear correlation of the values obtained with the three parameter sets with different effective mass but same scheme for c.m. correction for all of the choices for  $a_{\text{surf}}$ , but again the barrier heights do not perfectly correlate with any of the choices for  $a_{\text{surf}}$  across families of parameter sets with different c.m. correction. While the deformation dependence of the c.m. correction energy mentioned before brings an offset of about 1 MeV to the comparison of the results obtained with the 1T2T(X) and 1T2F(X) sets, there have to be other contributions that are even larger.

## E. Deformation

### 1. Normal-deformed ground states of actinides

Figure 14 compares the calculated ground-state quadrupole and hexadecapole deformations of U ( $Z = 92$ ) and Pu ( $Z = 94$ ) isotopes with the available data<sup>6</sup> for electric transition moments extracted from  $B(E2)$  and

<sup>6</sup> Note that the  $\beta_2$  and  $\beta_4$  values given by these references are surface deformations that are not equivalent to the volume deformations of Eq. (29). The experimental  $\beta_{\ell 0}$  values used for Fig. 14 were obtained from converting the Cartesian quadrupole

$B(E4)$  moments determined either from Coulomb excitation [148] or the analysis of muonic X rays [149, 161]. We mention that SLy5s1 and SLy7 give results that on the plot are almost indistinguishable from those obtained with 1T2T(0.70) and therefore have been omitted from the figure.

It is striking to see almost no difference between the calculated values obtained from different parametrizations, indicating that for well-deformed nuclei with a unique deep normal-deformed minimum in the energy surface the ground state deformation is solely determined by the deformation dependence of shell effects, but independent on the macroscopic surface energy. In addition, the experimental  $\beta_{20}$  values are almost perfectly reproduced by all parametrizations. Note that  $\beta_{20}$  and  $\beta_{40}$  follow a different trend when moving across a major shell, with the hexadecapole moment changing sign at about midshell, which can be understood from the spatial distribution of the single-particle wave functions that are successively filled, see Refs. [162, 163]. The actinide nuclei for which data are available are located close to the region where this happens. Within their large error bars, the experimental  $\beta_{40}$  values are fairly reproduced, although the calculated values tend to decrease too slowly with mass number. Although there is a modest spread in the predictions of different self-consistent models for hexadecapole deformation in this region, this mismatch between the calculated and experimental trend with mass number seems to be a consistent feature of all models that have been used to study this observable, as first discussed in Ref. [164] and shown explicitly in the case of  $^{238}\text{U}$  for 21 different parametrizations of Skyrme's EDF in Ref. [165]. Given this indication from different models and the inherent difficulties of the experimental determination of hexadecapole deformation, it seems worthwhile to revisit this region with modern technology. For  $^{238}\text{U}$  in particular, such experimental information would be complementary to information that might be gleaned from ultra-relativistic heavy-ion collisions of this nucleus [166].

As mentioned when discussing the fission barrier of  $^{240}\text{Pu}$  in Sec. V C, for a few parametrizations we find an octupole-deformed ground state for this nucleus that is accompanied by a very small energy gain of at most 200 keV for 1F2F(0.70). That the deformation energy surface of  $^{240}\text{Pu}$  is soft against octupole deformation has been noticed before [167, 168], indicating the possibility of dynamical octupole correlations that would explain the experimentally observed low-lying negative-parity band whose levels decay to states in the ground-state band via strong  $E1$  transitions [169, 170]. For the same four parametrizations, 1F2F(0.70), 1F2F(0.80), 1T2F(0.85), and 1T2T(0.70), we also find a shallow octupole-deformed minimum for  $^{238}\text{Pu}$ , again with an energy gain that

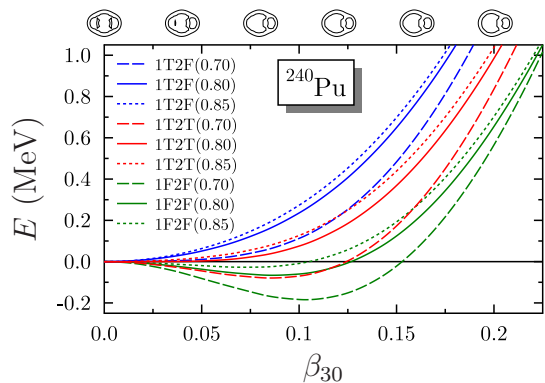


Figure 15. Energy of the normal-deformed configuration of  $^{240}\text{Pu}$  as a function of dimensionless octupole deformation  $\beta_{30}$ , plotted in the same colors and line styles as on Fig. 10. The inserts on top of the figure indicate the typical evolution of shapes along the energy curve.

does not exceed a few tens of keV. The  $\beta_{30}$  deformation of these isotopes are also displayed on Fig. 14. Compared with the lowest reflection-symmetric configuration of these isotopes, the quadrupole and hexadecapole deformations do not change by an amount that can be resolved on the figure. No octupole-deformed minima are found for the heavier plutonium isotopes or any of the uranium isotopes displayed on Fig. 14.

For the more neutron-deficient nuclei displayed on this figure, the presence or absence of an octupole-deformed minimum results from a small change in the softness of the deformation energy surface with respect to  $\beta_{30}$ , as is illustrated by Fig. 15 for  $^{240}\text{Pu}$ . The pattern of differences between the deformation energy curves is clearly correlated with the effective mass and the scheme for c.m. correction employed: the energy curve becomes stiffer when going from the 1F2F(X) to the 1T2T(X) and then to the 1T2F(X), reflecting the global dependence of  $a_{\text{surf}}$  on the scheme of c.m. correction. For parametrizations with the same scheme for c.m. correction, it is, however, the one with the *smallest* effective mass that is the softest against octupole deformation. Therefore, the sequence of energy curves is not directly determined by  $a_{\text{surf}}$ , as for a given c.m. scheme it is the parametrization with the *largest*  $m_0^*/m$  that has the smallest  $a_{\text{surf}}$  value (see Table IV). This points to an important role of the effective mass for the variation of shell effects with deformation that generate the octupole-deformed minima in this mass region. Comparing the parametrizations that generate an octupole-deformed minimum for this nucleus, the size of octupole deformation at the minimum and the energy gain are clearly correlated.

We mention that a similar pattern, but with much larger gain in deformation energy from octupole deformation, is also found for  $^{222}\text{Ra}$  [171], a nucleus for which empirical data point to static octupole deformation. Altogether, Fig. 15 confirms the finding of Ref. [13] that it is more likely to find static octupole deformation for pa-

---

and hexadecapole moments given in these references to spherical multipole moments  $Q_{\ell m}$  and then applying Eq. (29).



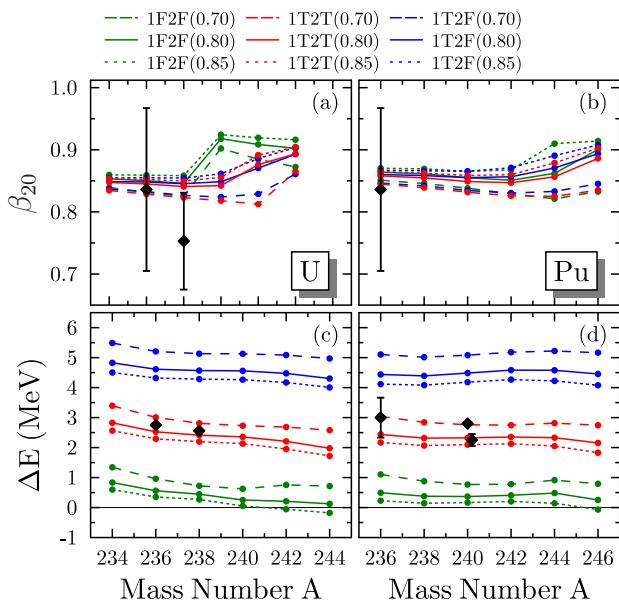


Figure 16. Charge quadrupole deformation (panels (a) and (b)) and excitation energy (panels (c) and (d)) of the  $0^+$  fission isomers of even-even U (panels (a) and (c)) and Pu (panels (b) and (d)) isotopes. Colors and line styles are the same as in the previous figures.

parametrizations of Skyrme’s EDF with low surface energy coefficient. The present study points to a second nuclear property of EDFs that amplifies such exotic deformation modes, which is a small effective mass as suspected in Ref. [33].

While our finding of octupole-deformed minima for a few plutonium isotopes indicates that lowering  $a_{\text{surf}}$  of a parametrization significantly increases the likelihood of shape transitions that involve exotic shape degrees of freedom in self-consistent mean-field calculations, the significance of the actual octupole-deformed minima for the interpretation of experimental data is less clear. The minima are too shallow to interpret the nuclei for which they are found as rigid octupole-deformed rotors, which also would be incompatible with experimental data for the observed states at low spin. Still, that fluctuations on octupole degrees of freedom might play a significant role for  $^{240}\text{Pu}$  is evident when comparing Fig. 15 with Fig. 10: around the ground state, the energy surface of  $^{240}\text{Pu}$  is much softer with respect to octupole deformation than with respect to quadrupole deformation for all nine of the “best fit” parametrizations, irrespective of their predicting an octupole-deformed minimum or not.

## 2. Superdeformed fission isomers of actinides

Figure 16 compares calculated values for the excitation energy and quadrupole deformation of superdeformed (SD) fission isomers of U ( $Z = 92$ ) and Pu ( $Z = 94$ ) isotopes with the available data. As done earlier in Ref. [8],

we limit the comparison to data for isomers that could be identified as  $0^+$  bandheads.

The excitation energies of the fission isomers of the uranium isotopes are taken from Ref. [172], the energy of the state with 37.4 ps lifetime of  $^{236}\text{Pu}$  from [154], and the energy of the isomer of  $^{240}\text{Pu}$  from Refs. [153, 154], see also Sec. VC.

The experimental  $\beta_2$  values were obtained converting the Cartesian charge quadrupole moments  $Q_0$  listed in Ref. [173] to spherical quadrupole moments  $Q_{20} = \sqrt{5/(16\pi)} Q_0$  first and then applying Eq. (29).

As could be expected from the discussion of the fission barrier of  $^{240}\text{Pu}$ , the 1T2F(X) parametrizations grossly overestimate the known excitation energies of fission isomers. This performance is similar to almost all other Skyrme parametrizations that use the 1T2F recipe and that are not fine-tuned to describe highly-deformed states. The 1F2F(X) on the other hand grossly underestimate this energy, so much so that SD minima become the global minima for some heavy actinide nuclei. The isomer excitation energies predicted by the 1T2T(X) are compatible with available data, further confirming that choosing the 1T2T(X) recipe for c.m. correction automatically leads to quite realistic, although not completely perfect, surface properties.

Taking into account the huge error bars on  $\beta_{20}$ , one can consider that all new parameter sets agree with data for the quadrupole deformation. Unlike the case of the normal-deformed minima, the calculated values do not fall on top of each other which indicates that there is some variation in the shell structure predicted in the second well.

We have checked that for all parametrizations the SD minimum is stable with respect to non-axial and reflection-asymmetric deformations.

## 3. Superdeformed states of Hg and Pb isotopes

Figure 17 compares predictions for the excitation energy and charge quadrupole moment of the  $0^+$  bandheads of SD rotational of even-even neutron-deficient Hg ( $Z = 80$ ) and Pb ( $Z = 82$ ) isotopes with available data.

Again, the experimental quadrupole deformations  $\beta_2$  have been deduced from Cartesian transition quadrupole moments<sup>7</sup>  $Q_t = \sqrt{16\pi/5} Q_{20}$  listed in Ref. [154]. These quadrupole moments are obtained from averaging transition moments between high-spin states built on top of the respective band head.

In general, the calculated  $\beta_2$  values of Pb isotopes are slightly larger than those of Hg isotopes with same

<sup>7</sup> Note that the  $\beta_2$  values given in the same Table of Ref. [154] are surface deformations that are not equivalent to the volume deformations defined through Eq. (29), see Ref. [13] and references therein.

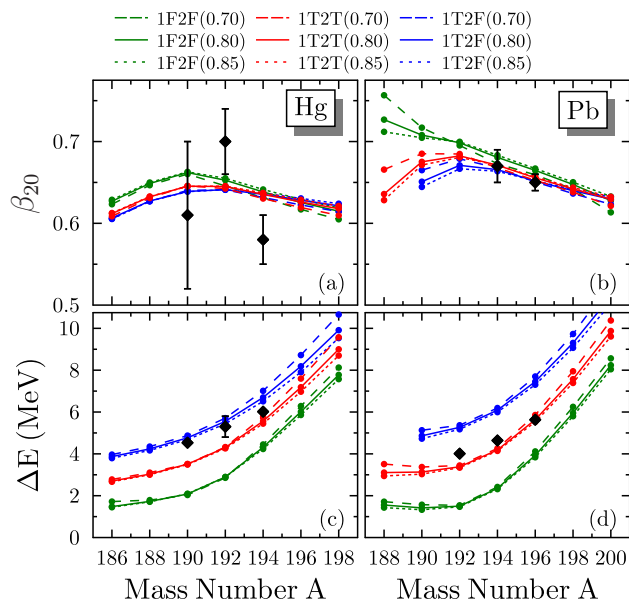


Figure 17. Charge quadrupole deformation (panels (a) and (b)) and excitation energy (panels (c) and (d)) of the hypothetical (see text)  $0^+$  bandheads of the superdeformed rotational bands of even-even Hg (panels (a) and (c)) and Pb (panels (b) and (d)) isotopes. Colors and line styles are the same as in the previous figures.

neutron number, pointing to a significant role of proton shell effects for the SD minimum. For both the Hg and Pb chains, the calculated  $\beta_2$  take their maximum value at about  $N \simeq 110$ . For Hg isotopes, the calculated  $\beta_2$  slightly fall off on both sides, whereas for Pb isotopes, only the values calculated with the 1T2F(X) and 1T2T(X) parametrizations follow this trend. For the heavier isotopes of both elements with  $N \gtrsim 110$ , all new fits predict similar  $\beta_2$  values that fairly reproduce the available data that have very large error bars. For the most neutron-deficient isotopes, however, the 1F2F(X) systematically yield slightly larger values than the fits from the two other series. This can possibly be attributed to 1F2F(X)'s  $a_{\text{surf}}$  values being smallest among all new fits and therefore yielding the softest deformation energy surfaces.

Not all Hg and Pb isotopes exhibit a SD minimum, and Fig. 17 is limited to the range of neutron numbers for which it is most likely to find one. Not all parametrizations predict an SD minimum for the same range of neutron numbers, as indicated by the 1T2F(X) for which none is found for  $^{188}\text{Pb}$ . That the likelihood of finding a SD minimum increases with decreasing  $a_{\text{surf}}$  has already been illustrated by Fig. 12 for  $^{180}\text{Hg}$ : the flatter the deformation energy surface, the more likely it is that local variations of shell effects generate local minima.

The experimental data for the excitation energies of the bandheads of the SD rotational bands in these nuclei are taken from Refs. [174–176]. The bandheads themselves have not been identified in experiment so far; in-

stead, their energy is estimated from the extrapolation of the excitation energies of high-spin levels in the rotational band built on top of them.

Going towards more neutron-deficient isotopes, the excitation energy  $\Delta E$  of the calculated SD bandheads first decreases rapidly and then levels out. As can be expected from their  $a_{\text{surf}}$  values, the curves obtained from the 1F2F(X), 1T2T(X) and 1T2F(X) are almost parallel, with an offset of about 1.5 MeV when going from one series to the next. The available experimental data, which are all in the region where the slope of the calculated  $\Delta E$  starts to level out, decrease slightly less quickly than the calculated ones. None of the new fits describes simultaneously the data for Hg and Pb isotopes: While the  $\Delta E$  of Pb isotopes are reasonably well described by the 1T2T(X) – which are also those that performed best for all other deformation energies discussed so far – the same parametrizations visibly underestimate the  $\Delta E$  of the Hg isotopes. By contrast, the 1T2F(X) with their larger  $a_{\text{surf}}$  fairly describe these data.

This discrepancy in performance for the  $\Delta E$  of adjacent Hg and Pb isotopes is likely to be a deficiency in the description of the relative size of shell effects in the various minima of Hg isotopes. The same flaw has been found for the SLy5sX series in Ref. [13]: SLy5s1 fairly describes the ground state and fission barrier of  $^{180}\text{Hg}$ , the fission barrier of  $^{240}\text{Pu}$  and the SD bandheads of Pb isotopes, but underestimates the SD band heads of Hg isotopes by a similar amount to what is found here for the 1T2T(X). That the  $\Delta E$  of Hg and Pb isotopes is not simultaneously described by widely-used parametrizations of the Skyrme EDF had already been pointed out earlier in Ref. [177].

#### 4. Shape coexistence of even-even Hg isotopes at normal deformation

As we mentioned already when discussing the fission barrier of  $^{180}\text{Hg}$  on Fig. 12, there is experimental evidence that the ground states of *even-even* Hg isotopes below  $N \simeq 120$  are the weakly oblate-deformed band heads of a collective rotational band, which at least for isotopes between  $100 \leq N \leq 110$  coexists with an excited prolate rotational band that has much larger a moment of inertia [178]. The excitation energy of the  $0^+$  state interpreted as the prolate band head roughly follows a parabolic trend with  $A$  [178], taking its minimal value of 328 keV for  $A = 182$ . For three of the intermediate *odd-mass* Hg isotopes with  $101 \leq N \leq 105$  around the minimum of this parabolic trend, however, a prolate state becomes the ground state, which leads to an anomalous odd-even staggering of charge radii [160, 178] in this mass region.

Nuclear EDF methods in general reproduce the coexistence of oblate and prolate states in this mass region. What most nuclear EDF methods fail to reproduce is the relative order and mass dependence of the energy differ-

ence between the prolate and oblate states [160].

Energy curves from calculations limited to axial symmetry often exhibit an additional third weakly-deformed prolate minimum that, however, might turn out to be a saddle point when considering more general non-axial shapes. When allowing for non-axial shapes, some of the calculated well-deformed prolate states become slightly triaxial for each of our best fit parametrizations. In most cases this concerns the two heaviest even-even isotopes for which such minimum is found, for the 1F2F(X) even the heaviest three, but for 1T2F(0.85) only the heaviest one. In any event, these are not the same isotopes for each parameter set. For  $^{180}\text{Hg}$  discussed earlier, and with energy curves shown on Fig. 12, only 1T2F(0.80) predicts slight triaxiality of its quite highly excited prolate state, which is accompanied by an energy gain of 50 keV. The triaxiality angle  $\gamma$  typically takes values between 7 and 15 degrees, and in most cases increases with  $A$ . Simultaneously, the energy gain from triaxiality also increases, taking values of up to about 350 keV for the last isotope for which such minimum is found. Altogether, this situation is quite different from the case of normal-deformed prolate states of Pu isotopes (shown on Fig. 14) for which the occurrence of octupole deformation is correlated to  $a_{\text{surf}}$  and  $m_0^*/m$ .

Panel (a) of Fig. 18 compares the total quadrupole deformation  $\beta_2 = \sqrt{\beta_{20}^2 + 2\beta_{22}^2}$  of the calculated minima found with the available data. We multiplied the  $\beta_2$  values of oblate states by a minus sign for better separation of the curves. Experimental data for the absolute  $\beta_2$  values of the oblate states as determined from  $B(E2, 2_1^+ \rightarrow 0_1^+)$  values through the rigid rotor model are taken from the NUDAT database [179]. There are indications that the low-lying coexisting states of some of these Hg isotopes are strongly mixed [180]; therefore, the rigid-rotor model cannot be expected to perfectly describe these transitions. Still, the calculated  $\beta_{20}$  of the oblate states agree well with these data. In particular, they reproduce well the slightly parabolic trend with  $A$ .

The experimental data for the absolute  $\beta_2$  values of the prolate states are deduced from the  $B(E2, 6_1^+ \rightarrow 4_1^+)$  values measured in the experiments reported in Ref. [181, 182], again through the rigid rotor model.<sup>8</sup> Because of their large moment of inertia, these states can be attributed to the rotational bands built on the prolate state of the respective nucleus. They are yrast for all nuclei for which there are data and expected to be less mixed with the oblate states than the lower-lying ones in this band, which makes the extraction of the transition quadrupole moment through the rigid-rotor model more reliable. The overall size and  $A$  dependence of the deformation of the prolate states is also well reproduced, although calculated values fall off less quickly with increasing  $A$ . This may simply point to the inadequacy of

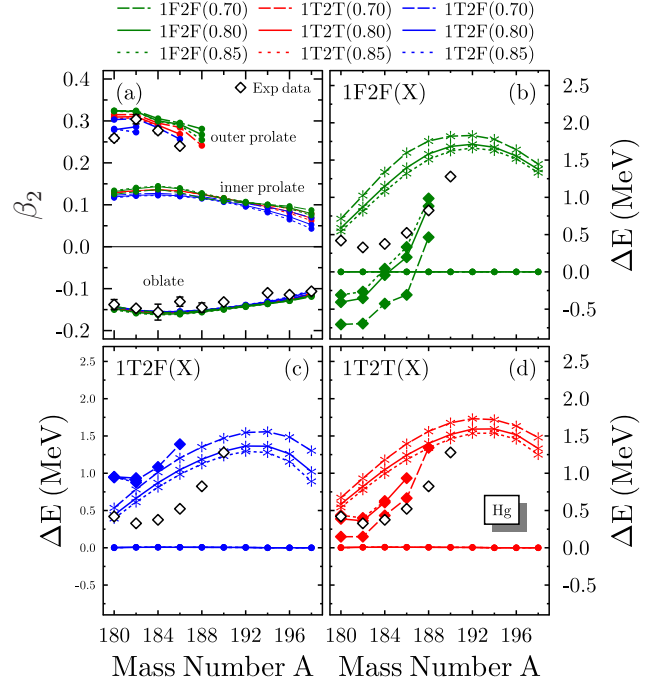


Figure 18. Shape coexistence at normal deformation in even-even neutron-deficient Hg isotopes. Panel (a): calculated dimensionless quadrupole charge deformation  $\beta_2$  of the three minima compared with experimental data where available (see text). Panels (b), (c), (d): energy of the weakly and strongly deformed prolate states relative to the oblate state shown separately for the 1F2F(X), 1T2F(X) and 1T2T(X) parametrizations. Colors and line styles are the same as in the previous figures.

the mean-field ansatz to model the complex structure of these states [180, 183].

The other three panels of Fig. 18 compare the energy of the coexisting normal-deformed minima to the energy of the oblate state with the available data. As we saw already in the discussion of the fission barrier of  $^{180}\text{Hg}$  represented on Fig. 12, depending on the choices made for the scheme of c.m. correction the new fits make very different predictions for shape coexistence at normal deformation of  $^{180}\text{Hg}$ , which is a direct consequence of the very different  $a_{\text{surf}}$  values of these fits.

For the 1T2F(X) [Fig. 18(c)] that have the largest  $a_{\text{surf}}$ , the ground state is oblate and the excitation energy of the well-deformed prolate states is grossly overestimated. Interestingly, the calculations do not find such prolate minimum for all isotopes for which a prolate rotational band is known. The second prolate minimum at smaller deformation remains well above the oblate state for all mass numbers.

For the 1T2T(X) [Fig. 18(d)] that have intermediate  $a_{\text{surf}}$  values, the ground state is also oblate, but now the well-deformed prolate states are at about the correct energy. Note that, without the additional energy gain from triaxial deformation, the excitation energy of the heav-

<sup>8</sup> Note that the  $\beta_2$  reported in Ref. [181] are again surface deformations, not volume deformations as plotted on Fig. 18.

ier isotopes would be further off the data. Unlike the case of the 1T2F(X), there is a visible effective-mass dependence of the excitation energy of the prolate state: reducing  $m_0^*/m$  also lowers the excitation energy.

For the 1F2F(X) that have the lowest  $a_{\text{surf}}$  values, the oblate and well-deformed prolate structures cross in energy, such that the lightest of the Hg isotopes shown in Fig. 18 have a prolate ground state. For the 1F2F(X), the effective-mass dependence of the excitation energy of the well-deformed prolate minimum is even more pronounced than for the 1T2T(X).

Comparing the three series, there is also a striking difference that concerns the isotopes for which a well-deformed prolate minimum is found: the range in  $A$  is smallest for the 1T2F(X) and largest for the 1F2F(X) parametrizations. More specifically, going from 1T2F(X) to 1T2T(X) and then to 1F2F(X) at a given effective mass, the heaviest isotope for which a well-deformed prolate minimum is found is in most cases pushed two mass units further up. There also is an effective-mass dependence: for 1T2T(0.70) and 1T2F(0.70), such minima are still found two mass units further up than for the parameter sets with larger effective mass from the same series.

In all cases, the excitation energy of the prolate band-head varies too quickly with mass number. Finding a well-deformed prolate minimum also seems to be correlated to its excitation energy: there are no such minima found at more than about 1.2 MeV above the oblate state.

As already noted when discussing Fig. 12, the differences in relative energy between the weakly-deformed oblate and well-deformed prolate minimum when comparing the 1F2F(X), 1T2T(X) and 1T2F(X) directly reflect the differences in their  $a_{\text{surf}}$  values: increasing  $a_{\text{surf}}$  leads to a larger loss in binding energy for the minimum at larger deformation.

The 1T2T(X) perform best for this phenomenon, confirming again that adjusting a parametrization of the Skyrme EDF at NLO with the full c.m. correction leads to quite realistic deformation properties, even when no information on deformed nuclei enters the adjustment protocol.

We mention in passing that for obvious reasons the 1T2T(X) are the only parametrizations out of the new fits that produce an anomalous odd-even staggering of the light Hg isotopes [171]; like in the case of SLy5s1 discussed in Ref. [160], however, the phenomenon is not predicted for exactly the same mass range at which it is observed experimentally.

## VI. SUMMARY, CONCLUSIONS AND OUTLOOK

We investigated the impact of choices made for the scheme of center-of-mass correction and the isoscalar effective mass  $m_0^*/m$  on the resulting surface properties of nuclear EDF through a series of dedicated fits of param-

eter sets of the widely-used standard NLO form of the Skyrme EDF.

To this aim we first constructed nine series of parametrizations that differ in their scheme for c.m. correction; i.e. none (1F2F), one-body term only (1T2F) and full one and two-body correction (1T2T), and in their isoscalar mass, i.e.  $m_0^*/m = 0.70, 0.80, \text{ and } 0.85$ . Adding a constraint on the surface energy coefficient  $a_{\text{surf}}^{\text{MTF}}$  calculated using the MTF approximation to a fit protocol that otherwise only constrains properties of doubly-magic spherical nuclei and properties of infinite matter, we constructed a set of parametrizations for each combination of c.m. correction strategy and  $m_0^*/m$  that covers the wide range of  $a_{\text{surf}}^{\text{MTF}}$ . The main observations and conclusions drawn from the analysis of these parametrizations are:

- The value of the penalty function of the adjustment protocol of the converged parameter fits varies strongly with  $a_{\text{surf}}^{\text{MTF}}$  within each of the nine series of fits.
- The optimal value for  $a_{\text{surf}}^{\text{MTF}}$  that gives the smallest value for the penalty function within a given series of fits depends strongly on the choice made for the scheme of c.m. correction in the EDF, as has been deduced earlier [14] in a much more limited study. In addition, there is a mild dependence of value for  $a_{\text{surf}}^{\text{MTF}}$  that minimizes the penalty function on the isoscalar effective mass  $m^*/m$ .
- We find strong correlations between almost all properties of infinite nuclear matter and the constrained value for  $a_{\text{surf}}^{\text{MTF}}$ . The origin of these correlations is probably threefold. First, there is a physics reason that can be qualitatively explained in the liquid-drop model: varying  $a_{\text{surf}}$  changes the contribution from the surface energy to the total binding energy of finite nuclei. To achieve a similar description of binding energies with different values of  $a_{\text{surf}}$ , other contributions to the LDM energy have to absorb the change in surface energy through a change of their coefficients. Second, there is a limitation of the standard Skyrme EDF: the number of its coupling constants is smaller than the number of relevant nuclear matter properties, which introduces an inevitable correlation between virtually all nuclear matter properties and the size of  $a_{\text{surf}}$ . As we cannot expect that the standard Skyrme EDF provides perfect modeling of nuclear systems and covers all physical degrees of freedom, this limitation of the Skyrme EDF introduces unphysical interdependencies between nuclear matter properties. Third, there is an accidental interconnection between the scheme chosen for the c.m. correction and the properties of nuclear matter properties. Although the c.m. correction itself does not contribute to the properties of infinite and semi-infinite matter, using different schemes during the parameter adjustment produces parametrizations with dif-



ferent nuclear matter properties as the other contributions to the total binding energy have to absorb the differences between the resulting c.m. correction energy.

- It is likely that similar correlations between the surface and surface symmetry energy will be found when constructing series of parametrizations with varied infinite matter properties.
- We confirm earlier studies [9] that, for NLO Skyrme EDFs, the values for  $a_{\text{surf}}$  obtained with different schemes to calculate semi-infinite matter, systematically differ by an offset. The MTF approach systematically gives values that are larger than the HF ones by a few hundreds of keV. The size of this offset depends on effective mass, which can be attributed to the *ansatz* for the kinetic density that is made in the MTF scheme. By contrast, values for  $a_{\text{surf}}$  obtained from the ETF approximation are systematically smaller than the HF ones, again by a few hundreds of keV. This time however, the difference between the  $a_{\text{surf}}$  slowly increases with their absolute size with a mild effective mass dependence. This confirms that the MTF value can serve as an efficient tool to constrain the isoscalar surface energy coefficient  $a_{\text{surf}}$  in a parameter fit. Unfortunately, extending the MTF scheme to asymmetric matter is not straightforward [102] and requires additional approximations when  $a_{\text{ssym}}$  is also to be constrained. In addition, the MTF *ansatz* is specifically tailored for the Skyrme NLO EDFs and cannot be applied to Skyrme EDFs of higher order in gradients that require the set-up of an alternative scheme [184].

In a second step, we constructed nine fits without constraint on  $a_{\text{surf}}^{\text{MTF}}$  that each represent the “best fit” for a given combination of choices for c.m. correction and isoscalar effective mass in the sense that they correspond to the minima of the penalty function of our adjustment protocol for each of the nine series constructed with a constraint on  $a_{\text{surf}}^{\text{MTF}}$ . Like the majority of parametrizations of the Skyrme EDF, the adjustment protocol of these nine “best fits” only considers properties of spherical nuclei and infinite nuclear matter, but no information on deformation properties of finite nuclei. With this, these parametrizations are representative of the consequences of the choices made for the scheme of c.m. correction and the effective mass on the surface energy of Skyrme EDFs at NLO. The main observations and conclusions from our analysis of their nuclear matter properties are:

- As a consequence of the correlations between  $a_{\text{surf}}$  and properties of infinite matter, the INM properties of the nine best fits systematically differ and this even in spite of some of them being constrained by the adjustment protocol.

- Most importantly, the nine “best fits” have systematically different values for the surface energy coefficient. First, there is a clear dependence on the scheme for c.m. correction: for the parameter sets using the 1T2F scheme,  $a_{\text{surf}}$  is almost 1 MeV larger than for parameter sets employing the full 1T2T scheme, whereas for parametrizations using the 1F2F scheme it is about 1 MeV smaller. This effect has already been identified for the difference between fits of 1T2F and 1T2T type before [14]. Our results demonstrate that something similar, but in the opposite direction, happens for fits of 1F2F type. On top of that, we also observe a mild dependence of  $a_{\text{surf}}$  on effective mass, at least in our fit protocol.

The main observations and conclusions from our analysis of the deformation energies of finite nuclei obtained with these nine parametrizations are:

- For all examples we studied, the calculated energy differences between two configurations in the same given nucleus scale roughly with the surface energy coefficient  $a_{\text{surf}}$  of the parametrization used. For some observables, but not all, there is an additional dependence on effective mass. The former of these two correlations can be expected from the deformation dependence of surface energy in the liquid-drop model, whereas the latter results from a deformation-dependence of shell effects.
- At small deformation, which means regions where the macroscopic liquid-drop energy is slowly varying with deformation, the actual deformation at which mean-field minima are found is rather insensitive to the value of  $a_{\text{surf}}$ . By contrast, the deformation of highly deformed excited states situated on the flank of a high fission barrier where the macroscopic energy varies quickly shows some dependence on  $a_{\text{surf}}$ . In addition, highly-deformed minima for some nuclei, are only found for parametrizations with low  $a_{\text{surf}}$ . From the point of view of Strutinski’s theorem, we attribute this behavior to the relative rate at which microscopic and macroscopic contributions contained in the EDF change with deformation. The former are determined by variations of the average density of single-particle levels around the Fermi energy, whereas the latter roughly increase quadratically with deformation, at least up to the point where the nucleus forms a neck. When the shell effects vary quicker than the macroscopic background, they determine the position of minima in the energy surface. By contrast, when the macroscopic background varies quicker than shell effects, then the barriers and minima obtained from the combined contributions move in deformation or might disappear completely.
- The 1T2T(X) fits provide the best overall agreement with experiment, particularly the parame-

trizations with elevated effective mass. Within the uncertainties of the experimental data, the 1T2T(X) parametrizations describe fairly well the fission barriers of  $^{240}\text{Pu}$  and  $^{180}\text{Hg}$ , ground-state deformation of actinides, shape coexistence in neutron-deficient Hg isotopes, and the superdeformed states of actinides and Pb isotopes. The only clear deficiency of the 1T2T(X) that we found is their underestimation of the excitation energy of the superdeformed bandhead of some Hg isotopes. By contrast, the 1F2F(X) systematically underestimate all deformation energy differences, whereas the 1T2F(X) almost always overestimate them.

- By no means, however, do the 1T2T(X) offer the best possible description of deformation energies that can be achieved for a Skyrme NLO EDF. This was not our purpose; instead these parametrizations demonstrate that a reasonable description of deformation energies can be achieved without explicitly considering information about deformation energies in the adjustment protocol by simply choosing the 1T2T scheme for c.m. correction. For parametrizations using the 1T2T scheme, the accurate description of deformation energies becomes a fine-tuning problem. For parametrizations using the 1T2F or 1F2F schemes on the other hand, the adjustment of deformation energies will require a major degradation of other properties. This is consistent with the recent BSkG1, BSkG2 [29], and BSkG3 [31] parametrizations, which all use the 1T2T recipe, achieving an excellent simultaneous description of masses, charge radii, fission barriers and nuclear matter properties relevant for nuclear astrophysics in case of BSkG3.
- The differences in deformation energy found between the 1F2F(X), 1T2T(X) and 1T2F(X) fits is almost independent on the contribution of the c.m. correction itself to the total energy. The slow variation of the c.m. correction with deformation only makes a visible difference for nuclei with a very wide fission barrier such as  $^{180}\text{Hg}$ .
- Our results confirm the finding of Ref. [13] that the likelihood of finding minima in the energy surface for configurations with exotic shapes increases with decreasing surface energy coefficient of the employed parametrizations. Our results point in addition to a significant role of the effective mass in this respect. This point deserves further study in the future.
- Our findings explain a number of observations made in the literature about the performance of Skyrme EDFs regarding nuclear deformation properties. Unfortunately the majority of Skyrme EDFs for nuclear structure and nuclear matter studies are still adjusted with the numerically less costly 1T2F scheme, which tends to make nuclei too rigid

against deformation. Constructing parametrizations for nuclear dynamics with the 1F2F scheme can also pose problems since such strategy tends to make nuclei too soft against deformation unless surface properties are explicitly tuned during the fit.

Our study raises the question to which extent not incorporating other quantal effects that cannot be easily described by mean-field modeling based on an EDF might also be spuriously imprinted on the properties of the EDF's parametrizations. The most immediate suspects are rotational and vibrational corrections for collective motion but the Wigner energy might be another [185].

There also is a noteworthy difference between the optimal values for  $a_{\text{surf}}$  when comparing different types of models. For the Skyrme EDFs used here, the best description of barriers is achieved for  $a_{\text{surf}}^{\text{HF}} \simeq 16.4 \text{ MeV}$  in combination with  $a_{\text{ssym}}^{\text{HF}} \simeq -46 \text{ MeV}$ . The surface and surface-symmetry energy coefficients of macroscopic-microscopic models, for which they usually are adjusted to fission barriers, are very different from these values. The FRLDM model of Ref. [130] gives  $a_{\text{surf}} = 21.269461 \text{ MeV}$  and  $a_{\text{ssym}} = -50.804 \text{ MeV}$ , and the three LDM models fitted in Ref. [131] have  $a_{\text{surf}}$  and  $a_{\text{ssym}}$  values of 19.3859 MeV and  $-38.4422 \text{ MeV}$  (LDM), 17.0603 MeV and  $-12.8737 \text{ MeV}$  (NLD), or 16.9707 MeV and  $-38.9274 \text{ MeV}$  (LSD), depending on the type of curvature term that is considered (i.e. none at all, a Gaussian one, or one of standard form). Among the aforementioned models, only the NLD describes fission barriers well, though. The comparison between the LDM models is complicated by their different definition of the surface (diffuse in the FRLDM and sharp in the models of Ref. [131]) and the use of different shape parametrizations in the study of fission barriers. With the exception of the LSD, none of these parametrizations comes close to the optimal value for a Skyrme EDF, although it has to be noted that it is not entirely clear how to calculate EDF values for  $a_{\text{surf}}$  and  $a_{\text{ssym}}$  that can be meaningfully compared with those of a macroscopic-microscopic model (i.e. with the HF scheme, or an ETF scheme, or even differently because of the different density profiles assumed in LDM models). In any event, all of the above points to the conclusion that one cannot expect that a parametrization of the nuclear EDF that reproduces the  $a_{\text{surf}}$  and  $a_{\text{ssym}}$  values of a macroscopic-microscopic model will perform well for deformation energies.

More relevant experimental data would be most useful to better constrain and benchmark nuclear surface properties; in particular data that probe the deformed density distribution of heavy nuclei, both for well-deformed ground states of heavy nuclei and especially for states at large deformation. The few existing measurements of higher-order shape deformations of nuclear ground states were all achieved in the 1970s mostly with stable nuclei. Similarly, there is very little information available on the excitation energies and quantum numbers of superdeformed states. In our view, the surface properties

of nuclear matter deserve more investment: such information is as important to fine-tune models as the much-more-often investigated bulk properties of nuclear matter.

For the reasons recalled above, among the parametrizations discussed in this paper, 1T2T(0.80) is the one that offers the best overall description of a wide range of observables. As they all use the full c.m. correction energy and keep the tensor terms from the two-body central interaction with coupling constants  $C_t^{sT}$  in Eqs. (5) and (6), the EDF of the 1T2T(X) has the same form as the one of SLy7 constructed in Ref. [17]. Because of the similarity of the adjustment protocol, we encourage the use of 1T2T(0.80) as a replacement of the parametrizations of Ref. [17] in future nuclear structure studies, and propose that it shall be used under the name of SLy7\*. Its parameters (which can also be found in the supplementary material [129]) are

$$\begin{aligned} t_0 &= -2676.132387, & x_0 &= 0.574713, \\ t_1 &= 381.547873, & x_1 &= 0.015424, \\ t_2 &= -438.549085, & x_2 &= -0.892996, \\ t_3 &= 15893.083082, & x_3 &= 0.764736, \\ W_0 &= 119.182854, & \alpha &= \frac{1}{6}. \end{aligned}$$

The parameter  $t_0$  is in  $\text{MeV fm}^3$ ,  $t_1$  and  $t_2$  in  $\text{MeV fm}^5$ ,  $t_3$  in  $\text{MeV fm}^{3+1/6}$ , and  $W_0$  in  $\text{MeV fm}^5$ . The  $x_j$  and  $\alpha$

are dimensionless.

Unlike SLy4 and SLy6, the form of SLy7\* includes all contributions to the EDF obtained from a two-body generator, removing some ambiguities about its use in nuclear matter studies. Compared with SLy7 and to the vast majority of other parametrizations of the Skyrme EDF at NLO, SLy7\* does not exhibit finite-size instabilities [45] in any of the  $(S, T)$  channels at densities encountered in finite nuclei, such that it can be used for time-reversal breaking calculations without the need for modifying coupling constants of the time-odd part of the EDF (6). We do not report on such calculations here, but we checked the stability of our parametrizations by means of cranked HFB calculations of rotational bands at high spin [171]. Results for rotational bands and one-quasiparticle states of odd-mass heavy nuclei obtained with time-reversal breaking calculations with SLy7\* will be reported elsewhere [186].

## ACKNOWLEDGMENTS

This project has been supported by the Agence Nationale de la Recherche, France, Grant No. 19-CE31-0015-01 (NEWFUN). W. Ryssens is a Research Associate of the Fonds de la Recherche Scientifique – FNRS (Belgium). The computations were performed using HPC resources from the CC-IN2P3 of the CNRS.

- 
- [1] M. Bender, P.-H. Heenen, and P.-G. Reinhard, Self-consistent mean-field models for nuclear structure, *Rev. Mod. Phys.* **75**, 121 (2003).
  - [2] N. Schunck, ed., *Energy density functional methods for atomic nuclei*, IOP Expanding Physics (IOP Publishing, Bristol, UK, 2019).
  - [3] A. N. Andreyev, K. Nishio, and K.-H. Schmidt, Nuclear fission: a review of experimental advances and phenomenology, *Rep. Prog. Phys.* **81**, 016301 (2018).
  - [4] K.-H. Schmidt and B. Jurado, Review on the progress in nuclear fission – experimental methods and theoretical descriptions, *Rep. Prog. Phys.* **81**, 106301 (2018).
  - [5] N. Schunck and L. M. Robledo, Microscopic theory of nuclear fission: a review, *Rep. Prog. Phys.* **79**, 116301 (2016).
  - [6] N. Schunck and D. Regnier, Theory of nuclear fission, *Prog. Part. Nucl. Phys.* **125**, 103963 (2022).
  - [7] M. Bender, R. Bernard, G. F. Bertsch, S. Chiba, J. Dobaczewski, N. Dubray, S. A. Giuliani, K. Hagino, D. Lacroix, Z. Li, P. Magierski, J. A. Maruhn, W. Nazarewicz, J. Pei, S. Péru, N. Pillet, J. Randrup, D. Regnier, P.-G. Reinhard, L. M. Robledo, W. Ryssens, J. Sadhukhan, G. Scamps, N. Schunck, C. Simenel, J. Skalski, I. Stetcu, P. Stevenson, S. Umar, M. Verrière, D. Vretenar, M. Warda, and S. Åberg, Future of nuclear fission theory, *J. Phys. G* **47**, 113002 (2020).
  - [8] N. Nikolov, N. Schunck, W. Nazarewicz, M. Bender, and J. Pei, Surface symmetry energy of nuclear energy density functionals, *Phys. Rev. C* **83**, 034305 (2011).
  - [9] R. Jodon, M. Bender, K. Bennaceur, and J. Meyer, Constraining the surface properties of effective Skyrme interactions, *Phys. Rev. C* **94**, 024335 (2016).
  - [10] J. Bartel, P. Quentin, M. Brack, C. Guet, and H.-B. Håkansson, Towards a better parametrisation of Skyrme-like effective forces: A critical study of the SkM force, *Nucl. Phys. A* **386**, 79 (1982).
  - [11] J. F. Berger, M. Girod, and D. Gogny, Time-dependent quantum collective dynamics applied to nuclear fission, *Comp. Phys. Comm.* **63**, 365 (1991).
  - [12] M. Kortelainen, J. McDonnell, W. Nazarewicz, P.-G. Reinhard, J. Sarich, N. Schunck, M. V. Stoitsov, and S. M. Wild, Nuclear energy density optimization: Large deformations, *Phys. Rev. C* **85**, 024304 (2012).
  - [13] W. Ryssens, M. Bender, K. Bennaceur, P.-H. Heenen, and J. Meyer, Impact of the surface energy coefficient on the deformation properties of atomic nuclei as predicted by Skyrme energy density functionals, *Phys. Rev. C* **99**, 044315 (2019).
  - [14] M. Bender, K. Rutz, P.-G. Reinhard, and J.A. Maruhn, Consequences of the center-of-mass correction in nuclear mean-field models, *Eur. Phys. J. A* **7**, 467 (2000).
  - [15] A. F. Stephenson, Correction due to motion of center of gravity in the Hartree approximation in nuclei, *Phys. Rev.* **51**, 590 (1937).
  - [16] S. Gartenhaus and C. Schwartz, Center-of-mass motion in many-particle systems, *Phys. Rev.* **108**, 482 (1957).
  - [17] E. Chabanat, P. Bonche, P. Haensel, J. Meyer, and R. Schaeffer, A Skyrme parametrization from subnu-

- clear to neutron star densities Part II. Nuclei far from stabilities, Nucl. Phys. A **635**, 231 (1998), Erratum Nucl. Phys. 643, 441 (1998).
- [18] K.-H. Kim, T. Otsuka, and P. Bonche, Three-dimensional TDHF calculations for reactions of unstable nuclei, J. Phys. G **23**, 1267 (1997).
- [19] M. Kortelainen, J. McDonnell, W. Nazarewicz, E. Olsen, P.-G. Reinhard, J. Sarich, N. Schunck, S. M. Wild, D. Davesne, J. Erler, and A. Pastore, Nuclear energy density optimization: Shell structure, Phys. Rev. C **89**, 054314 (2014).
- [20] K. Goeke, F. Grümmer, and P.-G. Reinhard, Three-dimensional nuclear dynamics in the quantized ATDHF approach, Annals of Physics **150**, 504 (1983).
- [21] J. Skalski, Relative kinetic energy correction to self-consistent fission barriers, Phys. Rev. C **74**, 051601 (2006).
- [22] P.-G. Reinhard and H. Flocard, Nuclear effective forces and isotope shifts, Nucl. Phys. A **584**, 467 (1995).
- [23] P. Klüpfel, P.-G. Reinhard, T. J. Bürvenich, and J. A. Maruhn, Variations on a theme by Skyrme: A systematic study of adjustments of model parameters, Phys. Rev. C **79**, 034310 (2009).
- [24] M. Samyn, S. Goriely, and J. M. Pearson, Nuclear mass predictions within the Skyrme HFB theory, Nucl. Phys. A **718**, 653 (2003).
- [25] M. Samyn, S. Goriely, M. Bender, and J. M. Pearson, Further explorations of Skyrme-Hartree-Fock-Bogoliubov mass formulas. III. Role of particle-number projection, Phys. Rev. C **70**, 044309 (2004).
- [26] S. Goriely, M. Samyn, and J. M. Pearson, Further explorations of Skyrme-Hartree-Fock-Bogoliubov mass formulas. VII. Simultaneous fits to masses and fission barriers, Phys. Rev. C **75**, 064312 (2007).
- [27] G. Scamps, S. Goriely, E. Olsen, M. Bender, and W. Ryssens, Skyrme-Hartree-Fock-Bogoliubov mass models on a 3D mesh: Effect of triaxial shape, Eur. Phys. J. A **57**, 333 (2021).
- [28] W. Ryssens, G. Scamps, S. Goriely, and M. Bender, Skyrme-Hartree-Fock-Bogoliubov mass models on a 3D mesh: II. Time-reversal symmetry breaking, Eur. Phys. J. A **58**, 246 (2022).
- [29] W. Ryssens, G. Scamps, S. Goriely, and M. Bender, Skyrme-Hartree-Fock-Bogoliubov mass models on a 3D mesh: IIb. Fission properties of BSkG2, Eur. Phys. J. A **59**, 96 (2023).
- [30] H. Krivine, J. Treiner, and O. Bohigas, Derivation of a fluid-dynamical Lagrangian and electric giant resonances, Nucl. Phys. A **336**, 155 (1980).
- [31] G. Grams, W. Ryssens, G. Scamps, S. Goriely, and N. Chamel, Skyrme-Hartree-Fock-Bogoliubov mass models on a 3D mesh: III. From atomic nuclei to neutron stars, Eur. Phys. J. A **59**, 270 (2023).
- [32] I. Ragnarsson and S. G. Nilsson, *Shapes and Shells in Nuclear Structure* (Cambridge University Press, 1995).
- [33] L. Guo, J. A. Maruhn, and P.-G. Reinhard, Triaxiality and shape coexistence in germanium isotopes, Phys. Rev. C **76**, 034317 (2007).
- [34] C. Mahaux, P. F. Bortignon, R. A. Broglia, and C. H. Dasso, Dynamics of the shell model, Physics Reports **120**, 1 (1985).
- [35] T. Lesinski, M. Bender, K. Bennaceur, T. Duguet, and J. Meyer, Tensor part of the Skyrme energy density functional: Spherical nuclei, Phys. Rev. C **76**, 014312 (2007).
- [36] M. Bender, K. Bennaceur, T. Duguet, P.-H. Heenen, T. Lesinski, and J. Meyer, Tensor part of the Skyrme energy density functional. II. Deformation properties of magic and semi-magic nuclei, Phys. Rev. C **80**, 064302 (2009).
- [37] L.-G. Cao, H. Sagawa, and G. Colò, Effects of tensor correlations on low-lying collective states in finite nuclei, Phys. Rev. C **83**, 034324 (2011).
- [38] F. Raimondi, B. G. Carlsson, and J. Dobaczewski, Effective pseudopotential for energy density functionals with higher-order derivatives, Phys. Rev. C **83**, 054311 (2011).
- [39] P. Becker, D. Davesne, J. Meyer, J. Navarro, and A. Pastore, Solution of Hartree-Fock-Bogoliubov equations and fitting procedure using the N2LO Skyrme pseudopotential in spherical symmetry, Phys. Rev. C **96**, 044330 (2017).
- [40] P. A. Zyla et al. (Particle Data Group), Review of Particle Physics, Prog. Theor. Exp. Phys. **2020**, 083C01 (2020).
- [41] E. Tiesinga, P. J. Mohr, D. B. Newell, and B. N. Taylor, CODATA recommended values of the fundamental physical constants: 2018, Rev. Mod. Phys. **93**, 025010 (2021).
- [42] J. Dobaczewski and J. Dudek, Time-odd components in the mean field of rotating superdeformed nuclei, Phys. Rev. C **52**, 1827 (1995), Erratum Phys. Rev. C **55**, 3177 (1997).
- [43] T. Lesinski, K. Bennaceur, T. Duguet, and J. Meyer, Isovector splitting of nucleon effective masses, ab initio benchmarks and extended stability criteria for Skyrme energy functionals, Phys. Rev. C **74**, 044315 (2006).
- [44] V. Hellemans, A. Pastore, T. Duguet, K. Bennaceur, D. Davesne, J. Meyer, M. Bender, and P.-H. Heenen, Spurious finite-size instabilities in nuclear energy density functionals, Phys. Rev. C **88**, 064323 (2013).
- [45] A. Pastore, D. Davesne, K. Bennaceur, J. Meyer, and V. Hellemans, Fitting Skyrme functionals using linear response theory, Physica Scripta **T154**, 014014 (2013).
- [46] J. Skalski, Self-consistent calculations of the exact Coulomb exchange effects in spherical nuclei, Phys. Rev. C **63**, 024312 (2001).
- [47] M. Anguiano, J. L. Egido, and L. M. Robledo, Coulomb exchange and pairing contributions in nuclear Hartree-Fock-Bogoliubov calculations with the Gogny force, Nucl. Phys. A **683**, 227 (2001).
- [48] J. Le Bloas, M.-H. Koh, P. Quentin, L. Bonneau, and J. I. A. Ithnin, Exact Coulomb exchange calculations in the Skyrme-Hartree-Fock-BCS framework and tests of the Slater approximation, Phys. Rev. C **84**, 014310 (2011).
- [49] S. Flügge, Zum Aufbau der leichten Atomkerne, Z. Phys. **96**, 459 (1935).
- [50] S. A. Fayans, Towards a universal nuclear density functional, JETP Letters **68**, 169 (1998).
- [51] S. A. Fayans, S. V. Tolokonnikov, E. L. Trykov, and D. Zawischa, Nuclear isotope shifts within the local energy-density functional approach, Nucl. Phys. A **676**, 49 (2000).
- [52] A. Bulgac, M. McNeil Forbes, S. Jin, R. N. Perez, and N. Schunck, Minimal nuclear energy density functional, Phys. Rev. C **97**, 044313 (2018).



- [53] M. Baldo, P. Schuck, and X. Viñas, Kohn–sham density functional inspired approach to nuclear binding, *Physics Letters B* **663**, 390 (2008).
- [54] M. Baldo, L. Robledo, P. Schuck, and X. Viñas, Energy density functional on a microscopic basis, *J. Phys. G* **37**, 064015 (2010).
- [55] M. N. Butler, D. W. L. Sprung, and J. Martorell, An improved approximate treatment of c.m. motion in DDHF calculations, *Nucl. Phys. A* **422**, 157 (1984).
- [56] L. Batail, *Étude des modes de respiration nucléaire dans le formalisme QRPA : un défi pour les interactions effectives modernes*, Ph.D. thesis, Université Claude Bernard Lyon 1 (2021).
- [57] H. Nakada, Modified parameter sets of M3Y-type semi-realistic nucleon-nucleon interactions for nuclear structure studies, *Phys. Rev. C* **81**, 027301 (2010).
- [58] J. Dobaczewski, K. Bennaceur, and F. Raimondi, Effective theory for low-energy nuclear energy density functionals, *J. Phys. G* **39**, 125103 (2012).
- [59] F. Raimondi, K. Bennaceur, and J. Dobaczewski, Non-local energy density functionals for low-energy nuclear structure, *J. Phys. G* **41**, 055112 (2014).
- [60] K. Bennaceur, A. Idini, J. Dobaczewski, P. Dobaczewski, M. Kortelainen, and F. Raimondi, Non-local energy density functionals for pairing and beyond-mean-field calculations, *J. Phys. G* **44**, 045106 (2017).
- [61] K. Bennaceur, J. Dobaczewski, T. Haverinen, and M. Kortelainen, Properties of spherical and deformed nuclei using regularized pseudopotentials in nuclear dft, *J. Phys. G* **47**, 105101 (2020).
- [62] J. Friedrich and P.-G. Reinhard, Skyrme-force parametrization: Least-squares fit to nuclear ground-state properties, *Phys. Rev. C* **33**, 335 (1986).
- [63] S. Goriely, M. Samyn, M. Bender, and J. M. Pearson, Further explorations of Skyrme-Hartree-Fock-Bogoliubov mass formulas. II. Role of the effective mass, *Phys. Rev. C* **68**, 054325 (2003).
- [64] R. E. Peierls and J. Yoccoz, The collective model of nuclear motion, *Proceedings of the Physical Society. Section A* **70**, 381 (1957).
- [65] R. E. Peierls and D. J. Thouless, Variational approach to collective motion, *Nucl. Phys.* **38**, 154 (1962).
- [66] S. Marcos, H. Flocard, and P.-H. Heenen, Calculation of the Peierls-Yoccoz translational mass for Hartree-Fock wave functions, *Phys. Lett. B* **134**, 287 (1984).
- [67] K. W. Schmid and F. Grümmer, On the treatment of the center of mass motion in nuclear mean field theories, *Z. Phys. A* **336**, 5–26 (1990).
- [68] R. R. Rodríguez-Guzmán and K. W. Schmid, Spherical Hartree-Fock calculations with linear momentum projection before the variation. Part I. Energies, form-factors, charge densities and mathematical sum rules, *Eur. Phys. J. A* **19**, 45 (2004).
- [69] R. R. Rodríguez-Guzmán and K. W. Schmid, Spherical Hartree-Fock calculations with linear momentum projection before the variation. Part II: Spectral functions and spectroscopic factors, *Eur. Phys. J. A* **19**, 61 (2004).
- [70] L. J. Tassie and F. C. Barker, Application to electron scattering of center-of-mass effects in the nuclear shell model, *Phys. Rev.* **111**, 940 (1958).
- [71] R. Dreizler, F. Krejs, and A. Klein, Application of the Hartree-Fock variational method to center-of-mass motion, *Nucl. Phys. A* **155**, 33 (1970).
- [72] K. W. Schmid and F. Grümmer, Translationally invariant treatment of the charge density in nuclei, *Z. Phys. A* **337**, 267–281 (1990).
- [73] K. W. Schmid and P.-G. Reinhard, Center-of-mass projection of Skyrme-Hartree-Fock densities, *Nucl. Phys. A* **530**, 283 (1991).
- [74] H. A. Bethe and M. E. Rose, Kinetic energy of nuclei in the Hartree model, *Phys. Rev.* **51**, 283 (1937).
- [75] J. P. Elliott, T. H. R. Skyrme, and J. D. Cockcroft, Centre-of-mass effects in the nuclear shell-model, *Proc. of the Royal Society of London A* **232**, 561 (1955).
- [76] H. J. Lipkin, Center-of-mass motion in the nuclear shell model, *Phys. Rev.* **110**, 1395 (1958).
- [77] M. O. Vassell, S. Borowitz, and J. K. Percus, Approximate solution of a finite many-particle system with translational invariance. I, *Phys. Rev.* **136**, B1266 (1964).
- [78] B. Giraud, Calcul des états parasites dus au mouvement du centre de masse, *Nucl. Phys.* **71**, 373 (1965).
- [79] J. B. Aviles, Separation of the center-of-mass in independent particle systems, *Annals of Physics* **50**, 393 (1968).
- [80] W. Scheid and W. Greiner, Theory of projection of spurious center of mass and rotational states from many-body nuclear wave functions, *Annals of Physics* **48**, 493 (1968).
- [81] K. T. R. Davies and R. L. Becker, Center-of-mass corrections in nuclear self-consistent field theories, *Nucl. Phys. A* **176**, 1 (1971).
- [82] K. Dietrich, On the introduction of collective variables in the non-relativistic theory of the nucleus, *Nucl. Phys. A* **606**, 63 (1996).
- [83] H. Krivine and J. Treiner, A simple approximation to the nuclear kinetic energy density, *Phys. Lett. B* **88**, 212 (1979).
- [84] M. Wang, W. Huang, F. Kondev, G. Audi, and S. Naimi, The AME 2020 atomic mass evaluation (II). tables, graphs and references, *Chinese Physics C* **45**, 030003 (2021).
- [85] J. M. Lattimer, Constraints on nuclear symmetry energy parameters, *Particles* **6**, 30 (2023).
- [86] R. B. Wiringa, V. Fiks, and A. Fabrocini, Equation of state for dense nucleon matter, *Phys. Rev. C* **38**, 1010 (1988).
- [87] G. H. Bordbar and M. Bigdeli, Spin polarized asymmetric nuclear matter and neutron star matter within the lowest order constrained variational method, *Phys. Rev. C* **77**, 015805 (2008).
- [88] E. Chabanat, P. Bonche, P. Haensel, J. Meyer, and R. Schaeffer, A Skyrme parametrization from subnuclear to neutron star densities, *Nucl. Phys. A* **627**, 710 (1997).
- [89] K. Bennaceur, P. da Costa, J. Dobaczewski, and M. Kortelainen, *Finres<sub>4</sub>*, finite-range self-consistent spherical space-coordinate solver (2023).
- [90] P.-G. Reinhard, M. Bender, W. Nazarewicz, and T. Vertse, From finite nuclei to the nuclear liquid drop: Leptodermous expansion based on self-consistent mean-field theory, *Phys. Rev. C* **73**, 014309 (2006).
- [91] J. Côté and J. M. Pearson, Hartree-Fock calculations of semi-infinite nuclear matter with complete forces (finite-range and spin-orbit term), *Nucl. Phys. A* **304**, 104 (1978).

- [92] J. Treiner and H. Krivine, Semi-classical nuclear properties from effective interactions, *Annals of Physics* **170**, 406 (1986).
- [93] M. Bender, K. Bennaceur, and W. Ryssens, Hartree-Fock code for calculations of semi-infinite nuclear matter (2023).
- [94] W. D. Myers, W. J. Swiatecki, and C. S. Wang, The surface energy of multi-component systems, *Nucl. Phys. A* **436**, 185 (1985).
- [95] M. Farine and J. M. Pearson, On the two definitions of nuclear surface energy and its calculation in two-component systems, *Phys. Lett. B* **167**, 259 (1986).
- [96] A. Dutta and M. Kohno, Microscopic calculation of the fission barrier of some actinide nuclei with the Skyrme-type interaction, *Nucl. Phys. A* **349**, 455 (1980).
- [97] M. Brack, C. Guet, and H.-B. Håkansson, Selfconsistent semiclassical description of average nuclear properties – a link between microscopic and macroscopic models, *Physics Reports* **123**, 275 (1985).
- [98] J. Dechargé and D. Gogny, Hartree-Fock-Bogolyubov calculations with the *D1* effective interaction on spherical nuclei, *Phys. Rev. C* **21**, 1568 (1980).
- [99] J. F. Berger, M. Girod, and D. Gogny, Constrained Hartree-Fock and beyond, *Nucl. Phys. A* **502**, 85 (1989).
- [100] M. Bender, P.-H. Heenen, and P. Bonche, Microscopic study of  $^{240}\text{Pu}$ : Mean field and beyond, *Phys. Rev. C* **70**, 054304 (2004).
- [101] P. Marević and N. Schunck, Fission of  $^{240}\text{Pu}$  with symmetry-restored density functional theory, *Phys. Rev. Lett.* **125**, 102504 (2020).
- [102] H. Krivine and J. Treiner, A simple determination of the nuclear surface symmetry energy, *Phys. Lett. B* **124**, 127 (1983).
- [103] A. W. Steiner, M. Prakash, J. M. Lattimer, and P. J. Ellis, Isospin asymmetry in nuclei and neutron stars, *Phys. Rep.* **411**, 325 (2005).
- [104] C. J. Horowitz, E. F. Brown, Y. Kim, W. G. Lynch, R. Michaels, A. Ono, J. Piekarewicz, M. B. Tsang, and H. H. Wolter, A way forward in the study of the symmetry energy: experiment, theory, and observation, *J. Phys. G* **41**, 093001 (2014).
- [105] M. Baldo and G. F. Burgio, The nuclear symmetry energy, *Prog. Part. Nucl. Phys.* **91**, 203 (2016).
- [106] X. Roca-Maza and N. Paar, Nuclear equation of state from ground and collective excited state properties of nuclei, *Prog. Part. Nucl. Phys.* **101**, 96 (2018).
- [107] M. Farine, J. M. Pearson, and B. Rouben, Higher-order volume-symmetry terms of the mass formula, *Nucl. Phys. A* **304**, 317 (1978).
- [108] W. Nazarewicz, P.-G. Reinhard, W. Satula, and D. Vretenar, Symmetry energy in nuclear density functional theory, *Eur. Phys. J. A* **50**, 20 (2014).
- [109] C. Mondal, B. K. Agrawal, J. N. De, S. K. Samaddar, M. Centelles, and X. Viñas, Interdependence of different symmetry energy elements, *Phys. Rev. C* **96**, 021302 (2017).
- [110] C. Mondal, B. K. Agrawal, J. N. De, and S. K. Samaddar, Correlations among symmetry energy elements in Skyrme models, *Int. J. Mod. Phys. E* **27**, 1850078 (2018).
- [111] J. M. Lattimer and Y. Lim, Constraining the symmetry parameters of the nuclear interaction, *The Astrophysical Journal* **771**, 51 (2013).
- [112] J. Dobaczewski, W. Nazarewicz, and P.-G. Reinhard, Error estimates of theoretical models: a guide, *J. Phys. G* **41**, 074001 (2014).
- [113] C. Ducoin, J. Margueron, C. Providência, and I. Vidaña, Core-crust transition in neutron stars: Predictivity of density developments, *Phys. Rev. C* **83**, 045810 (2011).
- [114] E. Khan, J. Margueron, and I. Vidaña, Constraining the nuclear equation of state at subsaturation densities, *Phys. Rev. Lett.* **109**, 092501 (2012).
- [115] Z. Zhang and L.-W. Chen, Constraining the symmetry energy at subsaturation densities using isotope binding energy difference and neutron skin thickness, *Phys. Lett. B* **726**, 234 (2013).
- [116] J. Piekarewicz and M. Centelles, Incompressibility of neutron-rich matter, *Phys. Rev. C* **79**, 054311 (2009).
- [117] J. Margueron, R. Hoffmann Casali, and F. Gulminelli, Equation of state for dense nucleonic matter from metamodeling. I. Foundational aspects, *Phys. Rev. C* **97**, 025805 (2018).
- [118] J. Margueron, R. Hoffmann Casali, and F. Gulminelli, Equation of state for dense nucleonic matter from metamodeling. II. Predictions for neutron star properties, *Phys. Rev. C* **97**, 025806 (2018).
- [119] B.-A. Li, B.-J. Cai, W.-J. Xie, and N.-B. Zhang, Progress in constraining nuclear symmetry energy using neutron star observables since GW170817, *Universe* **7**, 182 (2021).
- [120] G. Grams, R. Somasundaram, J. Margueron, and E. Khan, Nuclear incompressibility and speed of sound in uniform matter and finite nuclei, *Phys. Rev. C* **106**, 044305 (2022).
- [121] W. Zuo, I. Bombaci, and U. Lombardo, Asymmetric nuclear matter from an extended Brueckner-Hartree-Fock approach, *Phys. Rev. C* **60**, 024605 (1999).
- [122] M. Dutra, O. Lourenço, J. S. Sá Martins, A. Delfino, J. R. Stone, and P. D. Stevenson, Skyrme interaction and nuclear matter constraints, *Phys. Rev. C* **85**, 035201 (2012).
- [123] P. D. Stevenson, P. M. Goddard, J. R. Stone, and M. Dutra, Do Skyrme forces that fit nuclear matter work well in finite nuclei?, *AIP Conference Proceedings* **1529**, 262 (2013).
- [124] S. Goriely, N. Chamel, and J. M. Pearson, Further explorations of Skyrme-Hartree-Fock-Bogoliubov mass formulas. XII. Stiffness and stability of neutron-star matter, *Phys. Rev. C* **82**, 035804 (2010).
- [125] S. Goriely, N. Chamel, and J. M. Pearson, Further explorations of Skyrme-Hartree-Fock-Bogoliubov mass formulas. XIII. The 2012 atomic mass evaluation and the symmetry coefficient, *Phys. Rev. C* **88**, 024308 (2013).
- [126] B. Cochet, K. Bennaceur, P. Bonche, T. Duguet, and J. Meyer, Compressibility, effective mass and density dependence in Skyrme forces, *Nucl. Phys. A* **731**, 34 (2004).
- [127] S. Krewald, V. Klemt, J. Speth, and A. Faessler, On the use of Skyrme forces in self-consistent RPA calculations, *Nucl. Phys. A* **281**, 166 (1977).
- [128] Z. Zhang and L.-W. Chen, Extended Skyrme interactions for nuclear matter, finite nuclei, and neutron stars, *Phys. Rev. C* **94**, 064326 (2016).
- [129] See Supplemental Material at [URL will be inserted by publisher] for the coupling constants.
- [130] P. Möller, A. J. Sierk, T. Ichikawa,

- and H. Sagawa, Nuclear ground-state masses and deformations: FRDM (2012), *Atom. Data Nucl. Data Tables* **109-110**, 1 (2016).
- [131] K. Pomorski and J. Dudek, Nuclear liquid-drop model and surface-curvature effects, *Phys. Rev. C* **67**, 044316 (2003).
- [132] W. Ryssens, *Symmetry breaking in nuclear mean-field models*, Ph.D. thesis, Université Libre de Bruxelles, Brussels (2016).
- [133] D. Baye, The Lagrange-mesh method, *Physics Reports* **565**, 1 (2015).
- [134] W. Ryssens, P.-H. Heenen, and M. Bender, Numerical accuracy of mean-field calculations in coordinate space, *Phys. Rev. C* **92**, 064318 (2015).
- [135] W. Ryssens, V. Hellemans, M. Bender, and P.-H. Heenen, Solution of the Skyrme-HF+BCS equation on a 3D mesh, II: A new version of the Ev8 code, *Comp. Phys. Comm.* **187**, 175 (2015).
- [136] B. Gall, P. Bonche, J. Dobaczewski, H. Flocard, and P.-H. Heenen, Superdeformed rotational bands in the mercury region. A cranked Skyrme-Hartree-Fock-Bogoliubov study, *Z. Phys. A* **348**, 183 (1994).
- [137] W. Ryssens, M. Bender, and P.-H. Heenen, Iterative approaches to the self-consistent nuclear energy density functional problem. Heavy ball dynamics and potential preconditioning, *Eur. Phys. J. A* **55**, 93 (2019).
- [138] C. Rigollet, P. Bonche, H. Flocard, and P.-H. Heenen, Microscopic study of the properties of identical bands in the  $A = 150$  mass region, *Phys. Rev. C* **59**, 3120 (1999).
- [139] J. Erler, P. Klüpfel, and P.-G. Reinhard, A stabilized pairing functional, *Eur. Phys. J. A* **37**, 81–86 (2008).
- [140] T. Bürvenich, M. Bender, J. A. Maruhn, and P.-G. Reinhard, Systematics of fission barriers in superheavy elements, *Phys. Rev. C* **69**, 014307 (2004).
- [141] L. Bonneau, P. Quentin, and D. Samsøen, Fission barriers of heavy nuclei within a microscopic approach, *Eur. Phys. J. A* **21**, 391 (2004).
- [142] W. Younes and D. Gogny, Microscopic calculation of  $^{240}\text{Pu}$  scission with a finite-range effective force, *Phys. Rev. C* **80**, 054313 (2009).
- [143] Z. P. Li, T. Nikšić, D. Vretenar, P. Ring, and J. Meng, Relativistic energy density functionals: Low-energy collective states of  $^{240}\text{Pu}$  and  $^{166}\text{Er}$ , *Phys. Rev. C* **81**, 064321 (2010).
- [144] H. Abusara, A. V. Afanasjev, and P. Ring, Fission barriers in covariant density functional theory: Extrapolation to superheavy nuclei, *Phys. Rev. C* **85**, 024314 (2012).
- [145] N. Schunck, D. Duke, H. Carr, and A. Knoll, Description of induced nuclear fission with Skyrme energy functionals: Static potential energy surfaces and fission fragment properties, *Phys. Rev. C* **90**, 054305 (2014).
- [146] K. Rutz, J. Maruhn, P.-G. Reinhard, and W. Greiner, Fission barriers and asymmetric ground states in the relativistic mean-field theory, *Nuclear Physics A* **590**, 680 (1995).
- [147] M. Samyn, S. Goriely, and J. M. Pearson, Further explorations of Skyrme-Hartree-Fock-Bogoliubov mass formulas. V. Extension to fission barriers, *Phys. Rev. C* **72**, 044316 (2005).
- [148] C. E. Bemis, F. K. McGowan, J. L. C. Ford, W. T. Milner, P. H. Stelson, and R. L. Robinson,  $E2$  and  $E4$  transition moments and equilibrium deformations in the actinide nuclei, *Phys. Rev. C* **8**, 1466 (1973).
- [149] J. D. Zumbro, R. A. Naumann, M. V. Hoehn, W. Reuter, E. B. Shera, C. E. Bemis, and Y. Tanaka,  $E2$  and  $E4$  deformations in  $^{232}\text{Th}$  and  $^{239,240,242}\text{Pu}$ , *Phys. Lett. B* **167**, 383 (1986).
- [150] B. B. Back, O. Hansen, H. C. Britt, and J. D. Garrett, Fission of doubly even actinide nuclei induced by direct reactions, *Phys. Rev. C* **9**, 1924 (1974).
- [151] R. Capote, M. Herman, P. Obložinský, P. Young, S. Goriely, T. Belgva, A. V. Ignatyuk, A. J. Koning, S. Hilaire, V. A. Plujko, M. Avrigeanu, O. Bersillon, M. B. Chadwick, T. Fukahori, Z. Ge, Y. Han, S. Kailas, J. Kopecky, V. M. Maslov, G. Reffo, M. Sin, E. Soukhovitskii, and P. Talou, RIPL – Reference Input Parameter Library for calculation of nuclear reactions and nuclear data evaluations, *Nuclear Data Sheets* **110**, 3107 (2009), special Issue on Nuclear Reaction Data.
- [152] K. R. Kean, K. Nishio, K. Hirose, M. J. Vermeulen, H. Makii, R. Orlandi, K. Tsukada, A. N. Andreyev, I. Tsekhanovich, and S. Chiba, Validation of the multinucleon transfer method for the determination of the fission barrier height, *Phys. Rev. C* **100**, 014611 (2019).
- [153] M. Hunyadi, D. Gassmann, A. Krasznahorkay, D. Habs, P. G. Thirof, M. Csatlós, Y. Eisermann, T. Faestermann, G. Graw, J. Gulyás, R. Hertenberger, H. J. Maier, Z. Máté, A. Metz, and M. J. Chromik, Excited superdeformed  $K^\pi = 0^+$  rotational bands in  $\beta$ -vibrational fission resonances of  $^{240}\text{Pu}$ , *Phys. Lett. B* **505**, 27 (2001).
- [154] B. Singh, R. Zywna, and R. B. Firestone, Table of superdeformed nuclear bands and fission isomers: Third Edition (october 2002), *Nuclear Data Sheets* **97**, 241 (2002).
- [155] P. Möller, J. Randrup, and A. J. Sierk, Calculated fission yields of neutron-deficient mercury isotopes, *Phys. Rev. C* **85**, 024306 (2012).
- [156] M. Veselský, A. N. Andreyev, S. Antalic, M. Huyse, P. Möller, K. Nishio, A. J. Sierk, P. Van Duppen, and M. Venhart, Fission-barrier heights of neutron-deficient mercury nuclei, *Phys. Rev. C* **86**, 024308 (2012).
- [157] M. Warda, A. Staszczak, and W. Nazarewicz, Fission modes of mercury isotopes, *Phys. Rev. C* **86**, 024601 (2012).
- [158] Z. Li, S. Chen, Y. Chen, and Z. Li, Microscopic study on asymmetric fission dynamics of  $^{180}\text{Hg}$  within covariant density functional theory, *Phys. Rev. C* **106**, 024307 (2022).
- [159] A. N. Andreyev, J. Elseviers, M. Huyse, P. Van Duppen, S. Antalic, A. Barzakh, N. Bree, T. E. Cocolios, V. F. Comas, J. Diriken, D. Fedorov, V. Fedosseev, S. Franchoo, J. A. Heredia, O. Ivanov, U. Köster, B. A. Marsh, K. Nishio, R. D. Page, N. Patronis, M. Seliverstov, I. Tsekhanovich, P. Van den Bergh, J. Van De Walle, M. Venhart, S. Vermote, M. Veselsky, C. Wagemans, T. Ichikawa, A. Iwamoto, P. Möller, and A. J. Sierk, New type of asymmetric fission in proton-rich nuclei, *Phys. Rev. Lett.* **105**, 252502 (2010).
- [160] S. Sels, T. Day Goodacre, B. A. Marsh, A. Pastore, W. Ryssens, Y. Tsunoda, N. Althubiti, B. Andel, A. N. Andreyev, D. Atanasov, A. E. Barzakh, M. Bender, J. Billowes, K. Blaum, T. E. Cocolios, J. G. Cubiss, J. Dobaczewski, G. J. Farooq-Smith, D. V. Fedorov, V. N. Fedosseev, K. T. Flanagan, L. P. Gaffney,



- L. Ghys, P.-H. Heenen, M. Huyse, S. Kreim, D. Lunney, K. M. Lynch, V. Manea, Y. Martinez Palenzuela, T. M. Medonca, P. L. Molkanov, T. Otsuka, J. P. Ramos, R. E. Rossel, S. Rothe, L. Schweikhard, M. D. Seliverstov, P. Spagnoletti, C. Van Beveren, P. Van Duppen, M. Veinhard, E. Verstraelen, A. Welker, K. Wendt, F. Wienholtz, R. N. Wolf, and A. Zadvornaya, Shape staggering of midshell mercury isotopes from in-source laser spectroscopy compared with density-functional-theory and Monte Carlo shell-model calculations, *Phys. Rev. C* **99**, 044306 (2019).
- [161] J. D. Zumbro, E. B. Shera, Y. Tanaka, C. E. Bemis, R. A. Naumann, M. V. Hoehn, W. Reuter, and R. M. Steffen,  $E2$  and  $E4$  deformations in  $^{233,234,235,238}\text{U}$ , *Phys. Rev. Lett.* **53**, 1888 (1984).
- [162] G. F. Bertsch, Remark on  $Y_4$  moments, *Phys. Lett. B* **26**, 130 (1968).
- [163] J. Jänecke, Simple parameterization of nuclear deformation parameters, *Phys. Lett. B* **103**, 1 (1981).
- [164] J. Libert and P. Quentin, Self-consistent description of heavy nuclei. I. Static properties of some even nuclei, *Phys. Rev. C* **25**, 571 (1982).
- [165] W. Ryssens, G. Giacalone, B. Schenke, and C. Shen, Evidence of hexadecapole deformation in uranium-238 at the relativistic heavy ion collider, *Phys. Rev. Lett.* **130**, 212302 (2023).
- [166] N. Magdy, Impact of nuclear deformation on collective flow observables in relativistic U+U collisions, *Eur. Phys. J. A* **59**, 64 (2023).
- [167] L. M. Robledo and R. R. Rodríguez-Guzmán, Octupole deformation properties of actinide isotopes within a mean-field approach, *J. Phys. G* **39**, 105103 (2012).
- [168] S. E. Agbemava, A. V. Afanasjev, and P. Ring, Octupole deformation in the ground states of even-even nuclei: A global analysis within the covariant density functional theory, *Phys. Rev. C* **93**, 044304 (2016).
- [169] X. Wang, R. V. F. Janssens, M. P. Carpenter, S. Zhu, I. Wiedenhöver, U. Garg, S. Frauendorf, T. Nakatsukasa, I. Ahmad, A. Bernstein, E. Diffenderfer, S. J. Freeman, J. P. Greene, T. L. Khoo, F. G. Kondev, A. Larabee, T. Lauritsen, C. J. Lister, B. Meredith, D. Seweryniak, C. Teal, and P. Wilson, Structure of  $^{240}\text{Pu}$ : Evidence for octupole phonon condensation?, *Phys. Rev. Lett.* **102**, 122501 (2009).
- [170] M. Spieker, S. Pascu, D. Bucurescu, T. M. Shneidman, T. Faestermann, R. Hertenberg, H.-F. Wirth, N.-V. Zamfir, and A. Zilges, High-resolution ( $p, t$ ) study of low-spin states in  $^{240}\text{Pu}$ : Octupole excitations,  $\alpha$  clustering, and other structure features, *Phys. Rev. C* **97**, 064319 (2018).
- [171] P. Da Costa, *Interactions effectives de portée nulle et régularisées pour les calculs à l'approximation du champ moyen et au-delà*, Ph.D. thesis, Université Claude Bernard Lyon 1, Lyon (2022).
- [172] S. Garg, B. Maheshwari, B. Singh, Y. Sun, A. Goel, and A. K. Jain, Atlas of nuclear isomers – Second edition, *Atom. Data Nucl. Data Tables* **150**, 101546 (2023).
- [173] V. Metag, D. Habs, and H. Specht, Spectroscopic properties of fission isomers, *Physics Reports* **65**, 1 (1980).
- [174] A. N. Wilson, A. Korichi, S. Siem, A. Astier, D. Bazzacco, P. Bednarczyk, M. H. Bergström, S. Chmel, D. M. Cullen, P. M. Davidson, A. Görge, F. Hannachi, H. Hübel, N. Kintz, T. Lauritsen, A. Lopez-Martens, S. Lunardi, S. Naguleswaran, B. M. Nyakó, M. Rejmund, G. Schönwasser, C. Schück, J. F. Sharpey-Schafer, J. Timar, R. Wadsworth, and J. Libert, Two-particle separation energy trends in the superdeformed well, *Phys. Rev. Lett.* **104**, 162501 (2010).
- [175] T. L. Khoo, M. P. Carpenter, T. Lauritsen, D. Ackermann, I. Ahmad, D. J. Blumenthal, S. M. Fischer, R. V. F. Janssens, D. Nisius, E. F. Moore, A. Lopez-Martens, T. Døssing, R. Kruecken, S. J. Asztalos, J. A. Becker, L. Bernstein, R. M. Clark, M. A. Deleplanque, R. M. Diamond, P. Fallon, L. P. Farris, F. Hannachi, E. A. Henry, A. Korichi, I. Y. Lee, A. O. Macchiavelli, and F. S. Stephens, Excitation energies and spins of a superdeformed band in  $^{194}\text{Hg}$  from one-step discrete decays to the yrast line, *Phys. Rev. Lett.* **76**, 1583 (1996).
- [176] T. Lauritsen, T. L. Khoo, I. Ahmad, M. P. Carpenter, R. V. F. Janssens, A. Korichi, A. Lopez-Martens, H. Amro, S. Berger, L. Calderin, T. Døssing, S. M. Fischer, G. Hackman, F. Hannachi, C. J. Lister, E. F. Moore, D. T. Nisius, C. Schück, and S. Siem, Experimental determination of the excitation energy of superdeformed bands in  $^{192,194}\text{Hg}$  by analysis of the decay quasicontinuum  $\gamma$  rays, *Phys. Rev. C* **62**, 044316 (2000).
- [177] P.-H. Heenen, J. Dobaczewski, W. Nazarewicz, P. Bonche, and T. L. Khoo, Shell effects in superdeformed minima, *Phys. Rev. C* **57**, 1719 (1998).
- [178] K. Heyde and J. L. Wood, Shape coexistence in atomic nuclei, *Rev. Mod. Phys.* **83**, 1467 (2011).
- [179] National Nuclear Data Center, information extracted from the NuDat database, <https://www.nndc.bnl.gov/nudat/>.
- [180] K. Wrzosek-Lipska, K. Rezykina, N. Bree, M. Zielińska, L. P. Gaffney, A. Petts, A. Andreyev, B. Bastin, M. Bender, A. Blazhev, B. Bruyneel, P. A. Butler, M. P. Carpenter, J. Cederkäll, E. Clément, T. E. Cocolios, A. N. Deacon, J. Diriken, A. Ekström, C. Fitzpatrick, L. M. Fraile, C. Fransen, S. J. Freeman, J. E. García-Ramos, K. Geibel, R. Gernhäuser, T. Grahn, M. Guttorf, B. Hadinia, K. Hadyńska-Klęk, M. Hass, P. H. Heenen, R. D. Herzberg, H. Hess, K. Heyde, M. Huyse, O. Ivanov, D. G. Jenkins, R. Julin, N. Kesteloot, T. Kröll, R. Krücken, A. C. Larsen, R. Lutter, P. Marley, P. J. Napiorkowski, R. Orlandi, R. D. Page, J. Pakarinen, N. Patronis, P. J. Peura, E. Piselli, L. Próchniak, P. Rahkila, E. Rapisarda, P. Reiter, A. P. Robinson, M. Scheck, S. Siem, K. Singh Chakkal, J. F. Smith, J. Srebrny, I. Stefanescu, G. M. Tveten, P. Van Duppen, J. Van de Walle, D. Voulot, N. Warr, A. Wiens, and J. L. Wood, Electromagnetic properties of low-lying states in neutron-deficient Hg isotopes: Coulomb excitation of  $^{182}\text{Hg}$ ,  $^{184}\text{Hg}$ ,  $^{186}\text{Hg}$  and  $^{188}\text{Hg}$ , *Eur. Phys. J. A* **55**, 130 (2019).
- [181] T. Grahn, A. Petts, M. Scheck, P. A. Butler, A. Dewald, M. B. G. Hornillos, P. T. Greenlees, A. Görge, K. Helariutta, J. Jolie, P. Jones, R. Julin, S. Juutinen, S. Ketelhut, R. Krücken, T. Kröll, M. Leino, J. Ljungvall, P. Maierbeck, B. Melon, M. Nyman, R. D. Page, T. Pissulla, P. Rahkila, J. Sarén, C. Scholey, A. Semchenkov, J. Sorri, J. Uusitalo, R. Wadsworth, and M. Zielińska, Evolution of collectivity in  $^{180}\text{Hg}$  and  $^{182}\text{Hg}$ , *Phys. Rev. C* **80**, 014324 (2009).
- [182] L. P. Gaffney, M. Hackstein, R. D. Page, T. Grahn, M. Scheck, P. A. Butler, P. F. Bertone, N. Bree, R. J. Carroll, M. P. Carpenter, C. J. Chiara, A. Dewald,



- F. Filmer, C. Fransen, M. Huyse, R. V. F. Janssens, D. T. Joss, R. Julin, F. G. Kondev, P. Nieminen, J. Pakarinen, S. V. Rigby, W. Rother, P. Van Duppen, H. V. Watkins, K. Wrzosek-Lipska, and S. Zhu, Shape coexistence in neutron-deficient Hg isotopes studied via lifetime measurements in  $^{184,186}\text{Hg}$  and two-state mixing calculations, *Phys. Rev. C* **89**, 024307 (2014), Erratum *Phys. Rev. C* 89, 059905 (2014).
- [183] J. M. Yao, M. Bender, and P.-H. Heenen, Systematics of low-lying states of even-even nuclei in the neutron-deficient lead region from a beyond-mean-field calculation, *Phys. Rev. C* **87**, 034322 (2013).
- [184] P. Proust, Y. Lallouet, D. Davesne, and J. Meyer, Surface energy coefficient of an N2LO Skyrme energy functional: A semiclassical extended Thomas-Fermi approach, *Phys. Rev. C* **106**, 054321 (2022).
- [185] S. Goriely, M. Samyn, P.-H. Heenen, J. M. Pearson, and F. Tondeur, Hartree-Fock mass formulas and extrapolation to new mass data, *Phys. Rev. C* **66**, 024326 (2002).
- [186] J. Bonnard, W. Ryssens, and M. Bender, (2023), in preparation.